Dissertation
submitted to the
Combined Faculties of the Natural Sciences and Mathematics
of the Ruperto-Carola-University of Heidelberg, Germany
for the degree of
Doctor of Natural Sciences

Put forward by
Ioanna Arka
born in Athens, Greece
oral examination: 18.07.2011

Non-Linear Waves in the Laboratory and in Astrophysics: Pair Production in Counter-Propagating Laser Beams and Strong Waves in Pulsar Winds

Referees: Prof. Dr. John G. Kirk

PD Dr. Dr. Carsten Müller

Abstract

In this work we are investigating non-linear electromagnetic waves in two different physical environments: laboratories on earth and the astrophysical objects known as pulsars.

In the first part of our work the interaction of electrons and positrons with strong waves in the form of high intensity laser beams is analyzed. The possibility of emission of energetic radiation which can result in prolific pair production in the focus of two short, counter-propagating ultra-high intensity laser pulses is examined, taking into account several different possibilities for the relative polarizations and the waveform of the beams. The conclusion is reached that in the next generation laser facilities currently under construction mainly in Europe, like ELI and the 10PW Vulcan laser, pair production and electromagnetic pair cascades should be observed for intensities as low as $10^{24}\mathrm{Wcm}^{-2}$.

In the second part of this work we focus on large amplitude, low frequency waves that are emitted by pulsars. After a brief review of the current understanding of pulsar winds and the problems inherent to it, we show that the interaction of a relativistic striped pulsar wind with the the termination shock should result in reflection of electromagnetic energy in the upstream, which can affect the outflow, creating a precursor. We then investigate the possible conversion of the pulsar wind to a superluminal linearly polarized wave propagating upstream of the termination shock and show that this will result in the transfer of energy from the fields to the outflow particles in the precursor, lowering the magnetization of the outflow and opening the way for further particle acceleration at the shock front.

Zusammenfassung

In dieser Arbeit untersuchen wir nicht-lineare elektromagnetische Wellen in zwei unterschiedlichen physikalischen Umgebungen: im Labor auf der Erde und in Pulsaren im Weltraum.

Im ersten Teil dieser Arbeit analysieren wir die Wechselwirkung von Elektronen und Positronen mit hochintensiven Laserstrahlen. Wir untersuchen die Möglichkeit der Emission hochenergetischer Strahlung, welche im Fokus von zwei sich entgegengesetzt-propagierenden Laserstrahlen zur Paarproduktion in der Lage ist. Dazu betrachten wir verschiedene Möglichkeiten der relativen Polarisierungen und Wellenformen der Laserstrahlen. Wir zeigen, dass die nächste Generation von Lasern die gerade konstruiert werden, wie z.B. ELI und der 10PW Vulcan Laser, Elektonen-Positronen Paare und elektromagnetische Schauer bereits bei Intensitäten von $10^{24}\mathrm{Wcm}^{-2}$ erzeugen kann.

Im zweiten Teil dieser Arbeit konzentrieren wir uns auf Wellen mit grosser Amplitude und niedrigen Frequenz, die von Pulsaren ausgesandt werden. Nach einem kurzen Überblick über den momentanen Erkenntnisstand von Pulsarwinden und den damit verbundenen Problemen zeigen wir, dass die Wechselwirkung von relativistischen ("striped") Pulsarwinden mit dem Schock, der sich bildet wenn der Wind auf das interstellare Medium trifft, eine Reflektion von elektromagnetischer Energie erzeugt. Anschliessend betrachten wir die mögliche Umwandlung des Pulsarwindes zu einer linear-polarisierten Welle mit Phasengeschwindigkeit grösser als die des Lichtes, bevor der Wind den Schock erreicht. Durch diese Umwandlung wird Energie von den Feldern auf die Teilchen übertragen, was zu einer Verringerung der Magnetisierung des Ausflusses führt und somit den Weg frei macht für weitere Beschleunigung wenn der Schock erreicht ist.

Contents

List of Figures

to my beloved uncle, Dimitrios Eleutherianos
who would have been very proud to see me graduate

Chapter 1

Introduction - Contents of this thesis

In this thesis we will investigate the properties of the motion of particles in strong waves and the processes that take place during the interaction of particles with strong fields. In this opening chapter we introduce the concepts of strong waves and fields, and we discuss the environments in the laboratory and in astrophysics where they are relevant. At the end of the chapter we will give an overview of this thesis.

We will treat exclusively electrons and positrons, and it is to be understood that these two species of particles are meant whenever we refer to "particles" or "electrons". The symbol e is used for the magnitude of the electron charge, and the symbols m and c will be used throughout to denote the electron mass and the speed of light, respectively.

1.1 Strong waves and the strength parameter

Strong waves are electromagnetic waves, propagating either in vacuum or in plasmas, which can potentially accelerate particles to relativistic velocities within one wave period. This property can be quantified by introducing the strength parameter

$$a = \frac{eE_{\text{rms}}}{mc\omega} \tag{1.1}$$

with E_{rms} being the root mean square electric field of the wave, and ω its angular frequency. For a vacuum wave, the frequency is connected to the wavelength λ of the wave through the relationship

$$\lambda = \frac{2\pi c}{\omega}$$

so the strength parameter can be expressed as

$$a = \frac{eE_{\text{rms}}}{2\pi mc^2}\lambda \tag{1.2}$$

From 1.2 we see that the strength parameter expresses the work done by the field of the wave when the particle moves one wavelength in the root mean square electric field of the wave, in units of the electron rest mass energy mc^2. When $a \gg 1$ we will refer to the wave as a "strong wave", a wave which is capable of imparting to the particle energy much larger than its rest mass energy.

The equations of motion of a particle in the field of a strong vacuum wave are non linear in the particle momentum. This is why the process of particle interaction with a strong wave is often called "Nonlinear Thomson/Compton Scattering". Unlike classical Thomson scattering, which is elastic, and Compton scattering, where a relativistic electron gains or loses energy while downscattering or upscattering a photon, non-linear Compton scattering has as a result the recoil of the particle in the direction of the wave and the gain of energy of the order of magnitude $\sim amc^2$. Particles in a strong wave also gain a relativistic transverse momentum component, as we will see in detail in a subsequent chapter. The radiation resulting from the acceleration in a strong wave tends in the limit $a \gg 1$ to a continuous spectrum containing high harmonics of the wave's frequency ω.

The $a \ll 1$ limit will be referred to as the "weak wave" regime.

1.2 Strong fields and the critical Schwinger field

In 1929 physicist Oscar Klein applied the Dirac equation to the problem of the scattering of an electron by a potential barrier, a problem often encountered in non-relativistic quantum mechanics (see, for example [47]). The surprising result was that when the barrier became strong enough then the probability of transmission of the particle was increasing, contrary to what is expected classically. When the potential barrier approaches infinity then the transmission probability approaches unity and the reflection probability approaches zero. This counter-intuitive result is known as the *Klein paradox*.

The characteristic field value for which this phenomenon becomes important is calculated as the electric field which performs work equal to mc^2 over a Compton wavelength $\hbar/mc$. Thus this field is given by

$$F = \frac{m^2 c^3}{\hbar e} \tag{1.3}$$

and corresponds to an electric field of $E_{\rm cr} = 1.3 \times 10^{16} {\rm Vcm}^{-1}$. The corresponding magnetic field is $B_{\rm cr} = 4.414 \times 10^{13} {\rm Gauss}$. We will refer to this value as the *critical field*.

Fields close to or above this value are referred to as "strong fields". Electric fields of magnitude close to $E_{\rm cr}$ are able to impart to an electron energy equal or greater to its rest mass in one Compton wavelength. This implies the possibility of production of electron-positron pairs when strong fields are probed by an electron, in the process referred to as trident pair production. Pairs can also be produced in the interaction of photons of sufficient energy with static fields, in a process called single-photon pair production.

When we discuss pair production by relativistic electrons, the relevant field is that in the electron rest frame. This means that the critical Schwinger field can be approached if relativistic particles are moving in a field the value of which is, in the laboratory frame, much lower than the critical field. In the rest frame of the particle then, the field will be Lorentz boosted, so that $E_{\rm cr}$ can be approached and strong-field phenomena like pair production can be observed. This can be expressed by an invariant parameter, η, which for a particle moving with Lorentz factor γ transversely to a constant electric field of magnitude E in the absence of a magnetic field is

$$\eta = \gamma \frac{E}{E_{\rm cr}} \tag{1.4}$$

When η approaches or exceeds unity, the probability of strong-field processes like those mentioned above rises.

Another aspect of the Klein paradox is that a sufficiently strong static field can impart enough energy to virtual particles to make them real, causing pair creation out of the vacuum.

1.3 Probing strong waves and strong fields

1.3.1 Lasers

For the investigation of strong field phenomena, one would have to achieve an electric field of magnitude close to $E_{\rm cr}$. However, the critical field is too high to be achieved with today's means in the laboratory. This is why the use of relativistic particles in combination with moderately strong fields is a more realistic approach to the problem. This corresponds to maximizing not the field, but the parameter η introduced in the previous paragraph. To this end one would need a particle accelerator and a source of an intense field: the ideal candidate for accelerating particles and providing the electromagnetic field at the same time is a high-intensity laser.

The strength parameter of a linearly polarized laser pulse is expressed through its intensity and its wavelength as

$$a = 605 I_{24}^{1/2} \lambda_{\mu\rm m} \tag{1.5}$$

where I_{24} is the intensity of the beam at focus in units of $10^{24}\mathrm{Wcm}^{-2}$ and $\lambda_{\mu\rm m}$ the laser wavelength in micrometers.We see that for intensities close to $10^{24}\mathrm{Wcm}^{-2}$ and wavelengths of the order of 1μm the strength parameter is much larger than unity, and particles interacting with laser beams of such intensities would be accelerated to longitudinal Lorentz factors of the order of several hundreds.

On the other hand, an intensity of $10^{24}\mathrm{Wcm}^{-2}$ corresponds to a field of $E = 1.9 \times 10^{13}\mathrm{V/cm}$. This means that to a particle of Lorentz factor of a few hundred, this field can appear boosted to a value close to $E_{\rm cr}$ depending on the particle's direction of motion. The parameter η, then, can approach the value $\eta = 1$, where pair production by the processes mentioned above is possible. In this way lasers can act in a dual sense: as accelerators of electrons, and as targets which provide the field in which strong-field QED processes can occur.

The process of pair production, however, cannot proceed by injecting a non-relativistic electron in a single strong plane wave. The electron gets accelerated in the direction of the wave, with the result that in its rest frame the wave appears red-shifted. This lowers the η parameter and disfavours pair production. If a laser beam collides with a relativistic electron, however, the conditions for pair production can be fulfilled, since the laser fields are boosted in the particle frame. Strong waves can also be used to accelerate particles, with the strong field provided by a different source. Laser beams of intensity $\sim 10^{20}\mathrm{Wcm}^{-2}$ have already been used for the production of pairs, acting either as the accelerator of particles to high energy, or providing the intense field in the laser focus for beams of ultrarelativistic particles produced by a linear accelerator. The configuration of counter-propagating beams, however, achieves the advantages of both approaches, as we will explain in a subsequent chapter. The calculation of pair creation in counter-propagating laser beams is the subject of the first half of this thesis.

1.3.2 Pulsars

Pulsars are rapidly rotating, strongly magnetized neutron stars, which have periods in the order of magnitude of $10^{-3} - 1$sec. If pulsars were large magnetic dipoles rotating in vacuum, then they would emit strong electromagnetic waves. The strength parameter was first introduced in connection to these objects by Gunn and Ostriker [29], who were investigating the acceleration of particles by those waves. For the well-known Crab Pulsar, which has a surface magnetic field of the order of 10^{12}G and a rotation frequency $\omega = 190\text{sec}^{-1}$, the strength parameter close to the stellar surface is of the order of magnitude $a \sim 10^{10}$. With these field magnitudes and strength parameters, pulsars are the ideal astrophysical laboratory for the study of both strong-field processes and strong electromagnetic waves.

Indeed, the very same processes for pair production that are mentioned above in association with strong laser fields, are also in play in the vicinity of pulsars. The surface electric fields of pulsars are so strong, that they are capable of extracting particles (electrons) from the star. These particles can then produce secondary pairs through the energetic radiation emitted by electrons as they are accelerated in the pulsar's strong fields. The high energy photons interact with the field lines to produce electron-positron pairs via the process of single-photon pair production. Pulsar outflows consist mainly of these pairs.

The pair load of the pulsar magnetosphere dictates the type of outflow which the pulsar is going to launch. If the pair load is high, a magneto-hydrodynamic description of the pulsar wind is possible. In the opposite case the displacement current has to compensate for the dearth of charged particles, and the strong wave emitted by the pulsar could be converted to a superluminal mode, i.e. one which propagates with phase velocity $\beta_\phi > 1$. Such a mode resembles more a vacuum wave, with the displacement current term dominating the convection current, albeit one with superluminal phase speed. They have the advantage that they can propagate in plasmas of lower density, and are the subject of the second half of this thesis.

1.4 Structure of this thesis

This thesis consists of two parts: in the first, including chapters 2-5, the possibility of pair production using counter- propagating laser beams is discussed. The second part of the thesis includes chapters 6-8, where the properties of superluminal waves in pulsar outflows are investigated. We conclude with a summary of our results and a few words on possible future extension of our work in chapter 9.

Part I: Pair-production in the laboratory: counter-propagating laser beams

In Chapter 2 we give an overview of the physics and applications of ultra-short pulse, high intensity lasers. We present the evolution of laser intensities in the past decades and discuss the expectations for the new laser facilities that are going to be available for experiments in the next few years.

In Chapter 3 we introduce the physical processes which are relevant to particle radiation and pair production in the laboratory using laser beams. The motion of a particle in a strong wave

is analyzed, the use of classical physics for the calculation of particle trajectories is justified and the formulae for the evaluation of pair production are presented.

In Chapter 4 we review the techniques that have successfully been used for pair production in the laboratory. We argue that the proposed configuration of counter-propagating beams would be much more efficient for pair production, leading to the initiation of electromagnetic cascades in the laser focus. We review some previous results for circularly polarized beams, and present an analogy with astrophysical sources.

In Chapter 5, we use realistic models of pulses to estimate the probability of pair production by an electron accelerated in the focus of two counter-propagating beams. The results of these calculations have been published in [44]. We argue that only a few particles are enough to initiate cascades that could deplete the beams of their energy. We give an estimate of the threshold intensity where these cascades would occur, and argue that linear polarization is superior to circular as a means for pair production.

Part II: Non-linear waves in pulsar winds

In Chapter 6, we give a brief overview of pulsars and their outflows. We mention some of the open issues in the field, and the solutions that have been proposed in the past years to address them. We also introduce the conserved quantities in the pulsar winds and the approximations we make in order to simplify the problem.

In Chapter 7 we describe the striped wind, the magneto-hydrodynamic outflow that is predicted to be launched by a pulsar, and its termination shock, which signifies the transition from the relativistic wind to the pulsar wind nebula. Based on new estimates of the energy radiated by a shock front in the vacuum-wave approximation, we argue that the interaction of the striped wind with the termination shock will result in the reflection of Poynting flux in the upstream, in the form of a transverse, linearly polarized wave with the pulsar's frequency. We examine the impact of these estimates on the interpretation of recent pic simulations of magnetic field annihilation at shocks.

In Chapter 8 we investigate the conversion of the striped wind to a large amplitude, linearly polarized wave in a background magnetic field. We present detailed results of modes which propagate inwards from the termination shock, for different latitudes in the wind. We discuss how the problems of current pulsar wind models can be addressed using these modes and how this work can be extended in the future.

Conclusions

In Chapter 9 we give our conclusions in both the matters of electromagnetic cascade initiation in the focus of two counter- propagating laser beams using next generation lasers, and the conversion of a striped wind to a superluminal large-amplitude electromagnetic wave. We comment briefly on the significance of our results and on possible continuation of and improvement of the present calculations in the future.

Part I

Pair production in the laboratory: counter-propagating laser beams

Chapter 2

Laser intensities: past, present and future

2.1 Lasers: an introduction

Lasers are sources of radiation of high coherence. Their function is based on population inversion, the phenomenon that occurs when a system exists in a state with more of its members in an excited state than in the ground state. The members of the system can be for example atoms, molecules or ions in a crystal lattice. Such a medium emits photons either by spontaneous emission or by stimulated emission, which occurs when a photon of energy equal to the difference in energy levels between the excited and the ground states perturbs an excited atom (or molecule, or ion etc) and causes it to emit a photon of the same frequency and phase with the perturbing one. The two photons are then said to be coherent. This is the mechanism of amplification of radiation, which refers to the fact that the medium in population inversion emits more photons that it absorbs.

The basic components of a laser system are the *pump source*, the *gain medium* and the *resonant cavity*.

The pump source is a light source that provides energy to the laser system. This can be for example a flashlamp, an arc lamp or even another laser of suitable type.

The gain medium absorbs the energy provided by the pump source and is excited, so that a population inversion is induced. It is in this medium that stimulated emission takes place to produce the phenomenon of light amplification. The gain medium can be a solid, a liquid, a gas or a plasma and determines the wavelength of the laser radiation. It is placed in the resonant cavity, which is a device responsible for the trapping of the radiation in order to provide feedback to the mechanism of light amplification.

The simplest resonant cavity consists of two mirrors, one highly and one partially reflective, which allow for the photons to be reflected several times in order to stimulate emission in the gain medium, before they exit through the partially reflective mirror to produce the laser beam. If radiation is viewed as electromagnetic waves, then an equivalent description is that a resonant cavity allows for standing wave modes to exist for a long time, providing feedback on the light amplification mechanism.

The first demonstration of radiation amplification though population inversion was achieved

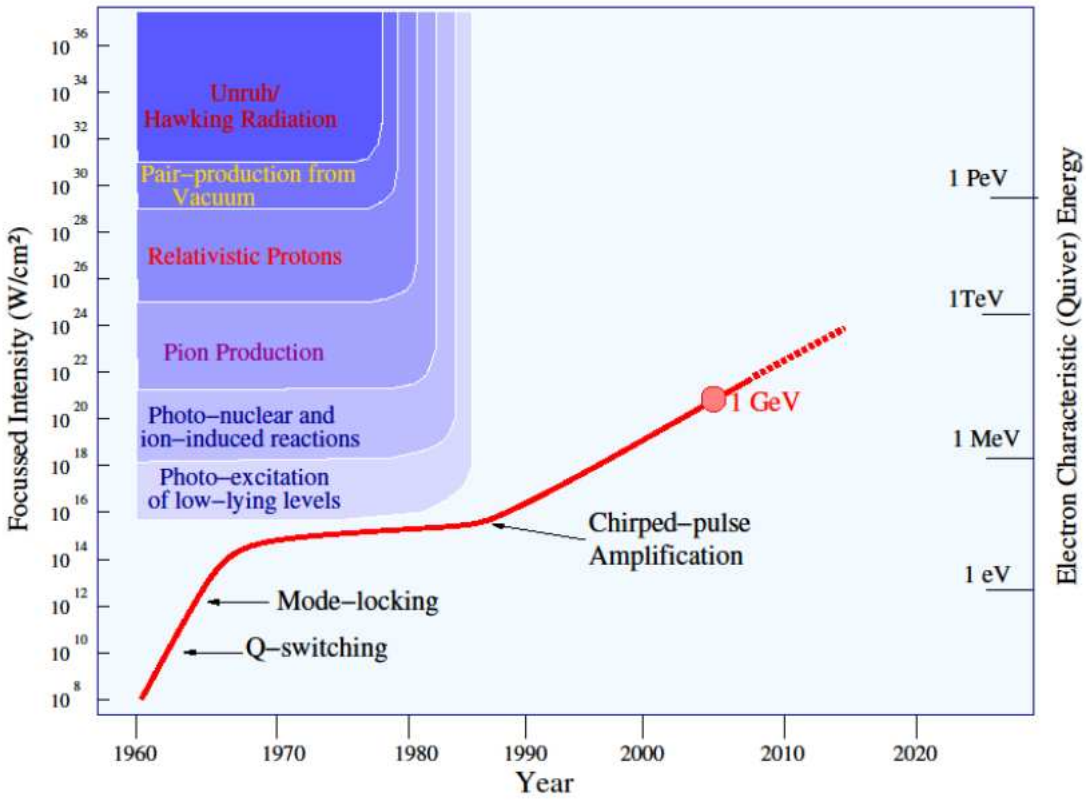

Figure 2.1: **Evolution of laser intensities in the past decades.**
This diagram shows the evolution of focused laser intensities in the decades from the 1960's to today. The plateau before the introduction of the Chirped Pulse Amplification (CPA) technique is notable. The figure is taken from [51].

in 1954 by Townes, Gordon and Zeiger [28], who inserted a population of excited ammonia molecules in a resonant cavity, the dimensions of which were constructed to be a multiple of the radiation's half wavelength. This device was called a *maser*, as an acronym of the phrase *Microwave Emission through Stimulated Emission of Radiation*. Six years later the function of the first "optical maser" was demonstrated by T. Maiman using a synthetic ruby crystal, which produces a very narrow emission line of wavelength 694.3nm [57]. This was named "laser", replacing "light" for "microwave" in the above acronym. This name has prevailed ever since to describe any device which emits highly coherent radiation, even if it operates in wavelengths different than those of optical light.

2.2 Evolution of laser intensities

The first optical laser, which was operated in 1960, had a focused intensity of $10^8 \mathrm{Wcm}^{-2}$. Since then laser intensities have been rising at a fast rate, as is readily seen in figure 2.1. This has been achieved mainly through the decrease of the pulse duration, which has as a consequence the rising of the laser power emitted in a single pulse.

At first pulses were compressed from the microsecond to the nanosecond regime, using a technique called Q-switching [34]. The principle behind *Q-switching* is to keep the losses in the

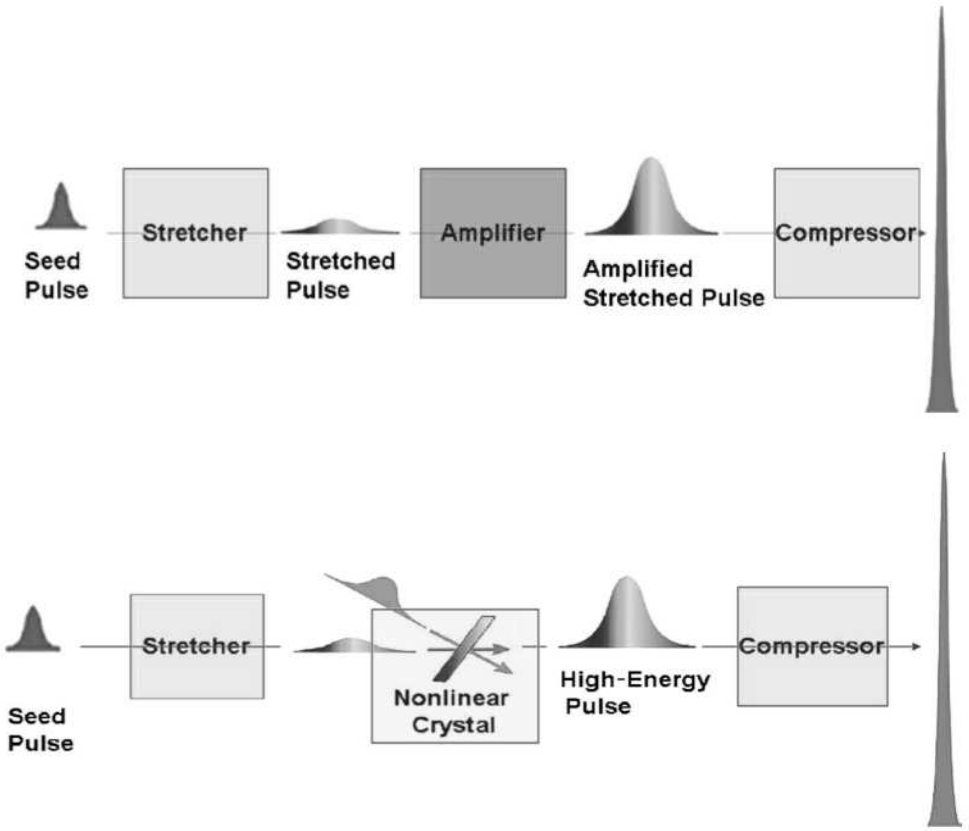

Figure 2.2: **Schematic representation of the CPA and OPCPA concepts.** *Stretching, amplifying and compression of pulses with the CPA and OPCPA techniques. The figures are taken from [68].*

resonator cavity high while pumping energy to the gain medium, so that stimulated emission cannot occur. The losses are governed almost exclusively by spontaneous emission, and the pumped energy is stored in the gain medium. Then when the stored energy reaches saturation levels, the losses are reduced to a small value, allowing the fast build up of energy power in the resonator cavity. The transition from the nanosecond to the picosecond (1ps = 10^{-12}sec) and even femtosecond (1fs = 10^{-15}sec) regime was achieved with *mode locking* [64], a technique in which the constructive interference between the modes in the resonating cavity is used to produce periodic pulses of intense laser light.

However, with mode locking the point was reached where further increase of peak intensity was not possible, due to non-linear effects in the gain medium [67]. This corresponds to the plateau seen in figure 2.1. Thus the peak intensity remained at the $10^{14} - 10^{15}$Wcm^{-2} region for two decades before a new technique called Chirped Pulse Amplification (CPA) revolutionized the field [85].

The Chirped Pulse Amplification technique consists of three stages: first a seed laser pulse is stretched in time by a factor of $10^3 - 10^5$. The stretching does not change the pulse energy, but it lowers the intensity so that non-linear effects in the gain medium are minimized. Then the pulse is amplified by $10^6 - 10^{12}$ and subsequently compressed back to a duration close to its original value [68].

A variation of the CPA technique is Optical Parametric Chirped Pulse Amplification (OPCPA) [18], which uses optical parametric amplification instead of regular optical amplification. In this technique the stretched signal beam propagates through a non-linear crystal along with a pump beam of higher energy photons. The photons of the pump beam then are converted into lower energy signal photons and the same number of idler photons, the energy of which is the difference between pump beam and signal photon energy. As the energy of the pump beam is converted to signal and idler photons, the signal beam is amplified. An advantage of optical parametric amplification is the larger bandwidth gain which allows for shorter pulse duration, something which contributes to the enhancement of intensity [68]. A schematic representation of the principles of CPA and OPCPA is given in figure 2.2.

Today, by using CPA and tight focusing techniques [5] laser intensities of the order of magnitude of 10^{22}Wcm^{-2} have been achieved. However, upgrades of current lasers and new facilities are planned which will push laser intensities higher by several orders of magnitude. We review some of them in a following section.

2.3 The future facilities

In the following we give some examples of facilities that are in the stage of planning or construction, which are going to achieve focused intensities of the order 10^{23}Wcm^{-2} and beyond in the next decade.

The Vulcan 10PW OPCPA project

One of the highest power lasers in operation today is the Vulcan Petawatt of the Central Laser Facility in the Rutherford Appleton Laboratory in Oxford. Currently it consists of 8 beams, two of which can operate in short-pulse mode giving pulses of energy up to 1PW and duration $\sim$ 500fs at the infrared wavelength of 1054nm.

At the moment the Vulcan Petawatt laser is able to provide pulses of ultra-high focused intensity greater than 10^{21}Wcm^{-2}. An upgrade is planned, however, which will achieve a power of 10PW. The project has two phases, with Phase 1 already completed: a front end has already been developed that can deliver a broadband pulse of energy $\sim$ 1J using Optical Parametric Chirped Pulse Amplification. In Phase 2 the pulse will be further amplified to energies of $\sim 300J$ and compressed to a maximum duration of 30fs. The Vulcan 10PW will then be able to produce pulses of intensity upwards of 10^{23}Wcm^{-2} [35]. This project has a timeframe of a few years.

Extreme Light Infrastructure

The Extreme Light Infrastructure (ELI) is a project involving institutions from 13 European countries, focused on science using ultra-high intensity lasers. ELI is focused on four areas of physics using hexawatt (10^{16}W) lasers, to each of which a facility is dedicated:

- *The production of ultra-short energetic particle (10 GeV) and radiation (up to few MeV) beams using compact laser plasma accelerators.* The corresponding facility (ELI-Beamlines facility) is under construction in Prague, Czech Republic.

- *Probing of extremely fast dynamic with attosecond (*10^{-18}sec*) pulses and general research with ultra-high intensity lasers.* The facility (ELI-Attosecond facility) is under construction in Szeged, Hungary.

- *Research in the field of laser-based nuclear physics, through coupling of the laser with a particle accelerator.* The facility (ELI-Nuclear Physics facility) is under construction in Magurele, Romania.

- *Physics with the highest intensity* ($> 10^{23}$Wcm^{-2})*laser beams.* The location of this facility (ELI-Ultra High Field facility) is going to be decided in the year 2012.

The first three sites are expected to be operational in the year 2015.

HiPER and other inertial confinement fusion facilities

An important area of study in the field of ultra-high intensity lasers is inertial confinement fusion, a process where a target of Deuterium-Tritium is compressed and heated until nuclear reactions begin. Several facilities are under construction or already in operation which are dedicated to investigating the feasibility of nuclear fusion as a future energy source.

HiPER (High Power laser Energy Research facility) is a proposed facility involving the co-operation of ten European countries and the United States of America. HiPER is dedicated to the research on laser fusion but is also going to conduct science in other areas, like those of materials science, astrophysics in the laboratory and laser-plasma interactions. The HiPER facility is expected to provide 60 beams and achieve intensities of 5×10^{24}Wcm^{-2} using Optical Parametric Chirped Pulse Amplification. The PETAL (Petawatt Aquitaine Laser) in the region of Aquitaine, France, is acting as a forerunner to HiPER.

The National Ignition Facility in (NIF) in Lawrence Livermore National Laboratory, is a 192-beam facility already conducting experiments in inertial confinement fusion. Its purpose is to be the first facility to achieve the extraction of more energy by fusion reactions in hydrogen targets than is spent for the target's heating, providing the conditions under which nuclear fusion can become a viable future energy source. The NIF operates since 2009, with the first ignition experiments having started in late 2010 [24]. It is capable of irradiating a fuel target with 1MJ of energy.

Another facility dedicated to the research of nuclear fusion is the Megajoule Laser (LMJ) in France, which is going to operate with 240 beams. It is currently under construction near Bordeaux, France. It is expected that the LMJ is going to be able to deliver 1.8MJ of energy to its targets, making it the largest laser fusion facility in the world. Its construction is expected to be finished by the year 2012.

Chapter 3

Physical Processes

3.1 Thomson scattering: from linear to non-linear

The simplest case of a particle-wave interaction to consider analytically in classical electrodynamics is the motion of an electron or positron in a plane, linearly polarized harmonic vacuum wave (see, for example [50]). The equation of motion of an electron in an electromagnetic field is [48]:

$$m\frac{du^i}{d\tau} = -\frac{e}{c}F^{ik}u_k \tag{3.1}$$

where radiation reaction forces have been ignored. In 3.1, u^i is the electron's $i-$th component of the four-velocity,

$$u^i = (\gamma, \gamma\mathbf{v}/c)$$

with $\mathbf{v}$ the three-velocity vector. m,e and c symbolize the electron's mass, magnitude of charge and the speed of light, τ is the proper time and F^{ik} are the components of the electromagnetic tensor. In the non-relativistic limit the Lorentz factor becomes $\gamma \simeq 1$ and the spatial four-velocity components are almost equal to the classical three-velocity components. Under these approximations the above equations of motion become

$$\frac{d\mathbf{p}}{dt} = \frac{e}{c}\left(\mathbf{E} + \frac{\mathbf{v}}{c} \times \mathbf{B}\right) \tag{3.2}$$

where $\mathbf{p} = m\mathbf{v}$ and the proper time has been replaced by laboratory time t. For a linearly polarized plane vacuum wave $E = B$ and thus in the non-relativistic limit the second term of the right-hand side is much smaller than the first since $v \ll c$ so we can safely ignore it. This way we arrive at the equation

$$\frac{d\mathbf{v}}{dt} = \frac{e}{mc}\mathbf{E} \tag{3.3}$$

where the velocity $\mathbf{v}$ has been normalized to the speed of light c.

In the case of a harmonic vacuum wave we have $\mathbf{E} = E\hat{\mathbf{e}}\cos\omega(t - x/c)$ where $\hat{\mathbf{e}}$ is a unit vector in the direction of the field and E the electric field magnitude. The wave propagates in the positive $x-$direction and $\hat{\mathbf{e}}$ is perpendicular to the propagation direction. Normalizing time to the inverse of the wave's frequency, $t' = \omega t$ and space to the inverse of the wavelength,

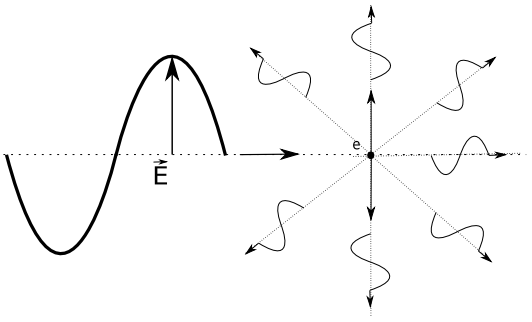

Figure 3.1: **Particle in a weak wave.** *Depiction of the oscillation and radiation of a particle in the field of a weak harmonic vacuum wave: the particle undergoes oscillations in the direction of the electric field, and radiates according to the classical Thomson formula. The oscillation is non-relativistic and the radiation is not beamed.*

$x' = \omega x/c$ we arrive to the equation

$$\frac{d\mathbf{v}}{dt'} = a\hat{\mathbf{e}}\cos(t' - x') \tag{3.4}$$

where we have introduced the parameter

$$a = \frac{eE}{mc\omega} \tag{3.5}$$

This is a different definition of the strength parameter of the electromagnetic wave, using the amplitude instead of the root mean square value of the field, and it differs from the definition we gave in Chapter 1 by a multiplicative constant of order of magnitude unity, which depends on the polarization of the beam. The strength parameter defined in this way is also known as the wiggler or undulator parameter (in which case it is symbolized K). Introducing the invariant phase of the wave $\phi = t' - x'$ we have

$$\frac{d\phi}{dt'} = 1 - v_x$$

and imposing the initial condition of the electron being at rest at zero phase, $v_x = 0$ at all times and

$$\frac{d\mathbf{v}}{d\phi} = a\hat{\mathbf{e}}\cos\phi \tag{3.6}$$

The strength parameter then governs the magnitude of the particle's velocity:

$$\mathbf{v} = a\hat{\mathbf{e}}\sin\phi$$

The velocity amplitude is a, which means that for the approximations used above to hold, the condition $a \ll 1$ has to hold. In other words, if $a \ll 1$ then the electric field is small enough and the frequency of the wave is high enough so that in the time interval between field reversals the particle cannot get accelerated to relativistic velocities. Such waves are referred to as weak waves.

However for a sufficiently low frequency wave with a sufficiently large amplitude the strength parameter can approach or exceed unity. This means that the particle can get accelerated to relativistic velocities within a half-period of the wave. In this case the rest of the terms of the equation of motion cannot be ignored any more, and the non-linear terms cannot be approximated by their linear counterparts. The term $\mathbf{v} \times \mathbf{B}$ is going to start being significant and will act to bend the particle's trajectory away from its harmonic oscillation form.

The equations of motion then become (see, for example [50]):

$$\frac{d\gamma}{d\tau} = \frac{e}{mc}\mathbf{u}\cdot\mathbf{E} \tag{3.7}$$

$$\frac{d\mathbf{u}}{d\tau} = \frac{e}{mc}\left(\gamma\mathbf{E} + \mathbf{u}\times\mathbf{B}\right) \tag{3.8}$$

We consider the same harmonic wave, where $E = B$, and we take the electric field to be in the $y-$direction and the magnetic field to be in the $z-$direction. Then $d\tau = dt/\gamma$ and we normalize time again to the inverse of the wave frequency, keeping the symbols t and x for the new dimensionless variables instead of t' and x'. This way we arrive at the equations

$$\frac{d\gamma}{d\tau} = \frac{du_x}{d\tau} = a u_y \cos(t-z) \tag{3.9}$$

$$\frac{du_y}{d\tau} = a(\gamma - u_x)\cos(t-z) \tag{3.10}$$

$$\frac{du_z}{d\tau} = 0 \tag{3.11}$$

We immediately see from the first of these equations that there is a conserved quantity of the motion:

$$Z = \gamma - u_x$$

Using this property and changing the variable to the dimensionless phase $\phi = t - z$ we have

$$\frac{d\phi}{d\tau} = \gamma - u_x = Z \tag{3.12}$$

and the equations of motion become:

$$\frac{du_y}{d\phi} = a\cos\phi \tag{3.13}$$

$$\frac{d\gamma}{d\phi} = \frac{du_x}{d\phi} = \frac{a^2}{Z}\cos\phi\sin\phi \tag{3.14}$$

$$\frac{du_z}{d\phi} = 0 \tag{3.15}$$

The solution to the above equations, for the initial condition $(\gamma_0, u_{x0}, u_{y0}, u_{z0}) = (1,0,0,0)$, $\phi_0 = 0$, i.e. a particle at rest at the origin of space and time, is

$$\gamma = 1 + \frac{a^2\sin^2\phi}{2} \tag{3.16}$$

$$u_x = \frac{a^2\sin^2\phi}{2} \tag{3.17}$$

$$u_y = a\sin\phi \tag{3.18}$$

$$u_z = 0 \tag{3.19}$$

which imply that the constant Z is in this case equal to 1. This solution is periodic in ϕ with period 2π. It consists of a center-of-momentum motion with a constant velocity and the well known "figure-of-8" motion in the center-of-momentum frame as seen in figure 3.1. The temporal

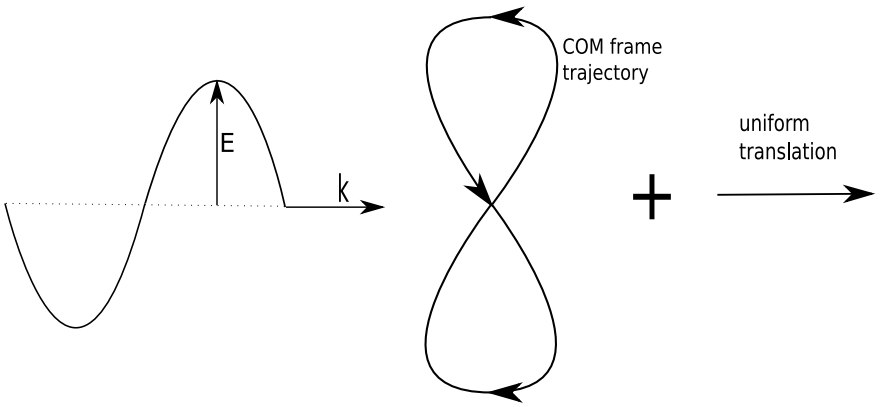

Figure 3.2: **Particle in a strong wave.**
The trajectory of a particle in a strong, linearly polarized vacuum wave, consists of a center of momentum motion, shown left, which is a figure-of-eight motion, plus a uniform translation of the center-of-momentum frame. The uniform translation will generally also include a drift which is perpendicular to the propagation direction of the wave (not shown here).

period can be shown to be [50]:

$$T = 2\pi \left(1 + \frac{a^2}{4}\right) \tag{3.20}$$

while the corresponding change in x in this amount of time is

$$x_T = 2\pi \frac{a^2}{4} \tag{3.21}$$

Thus the mean recoil velocity in the wave direction is the ratio of these two quantities:

$$\langle v_x \rangle = \frac{a^2}{a^2 + 4} c \tag{3.22}$$

and for $a \gg 1$ it is very close to the speed of light. We can define a center-of-momentum Lorentz factor which corresponds to this velocity as

$$\gamma_{com} = \frac{1}{\sqrt{1 - v_x^2/c^2}} \sim a \tag{3.23}$$

For $a \gg 1$ the center-of-momentum frame is moving with a Lorentz factor comparable to the strength parameter of the wave in the propagation direction of the wave. Qualitatively this can be understood as following: since initially $\mathbf{v} \parallel \mathbf{E}$ and the fields of a vacuum wave are perpendicular to the direction of motion, the initial $\mathbf{v} \times \mathbf{B}$ acceleration is in the direction of motion. The particle trajectory is continuously bent by the interplay of the $\mathbf{E}$ and $\mathbf{v} \times \mathbf{B}$ forces during a half-period of the wave in such a way as to induce the mentioned center-of-momentum drift.

It is straightforward to show that, for a particle with initial Lorentz factor $\gamma_0 \gg a$ which propagates against the harmonic vacuum wave, the center-of-momentum Lorentz factor is reduced to the value $\gamma \sim \gamma_0/a$ [52]. Thus particles picked up by the wave will be accelerated to $\gamma_{com} \sim a$, while the center-of-momentum drift of high energy particles propagating against the wave will decelerate, although the particles themselves still gain energy.

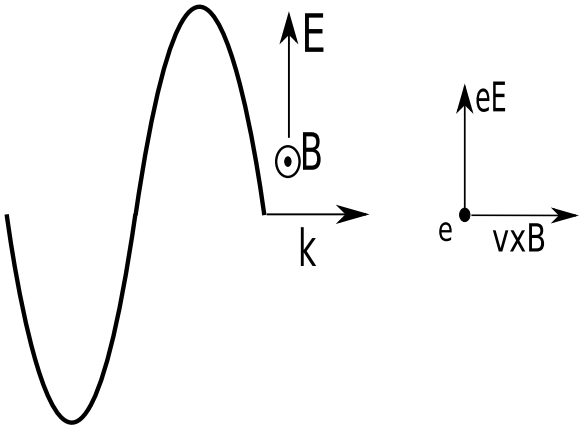

Figure 3.3: **Forces acting on a particle in a strong linearly polarized vacuum wave.** *The forces acting initially on a particle in the field of a strong vacuum wave: the combination of the* **E** *and* $\mathbf{v} \times \mathbf{B}$ *forces is responsible for the drift in the wave direction.*

This is why particles interacting with strong electromagnetic waves recoil in the propagation direction of the wave. There is generally also a perpendicular drift which depends on the initial conditions.

The strength parameter from a quantum mechanical point of view, represents the work done by the field on the particle in one Compton wavelength $eE\hbar/mc$ divided by the energy quantum of the wave $\hbar\omega$. The obvious implication of this is that with the strength parameter rises the probability of the absorption of more than one beam photons by an electron interacting with the wave. The transition from the linear to the non-linear regime happens, as in the classical case, around the value $a \sim 1$. In the limit $a \gg 1$ the number of photons absorbed by an electron during a scattering is large enough to justify a classical description of the wave-particle interaction.

3.2 Radiation reaction: the Landau-Lifshitz approximation

In order to get to the formulae describing the classical motion of electrons in a strong wave, the equations of motion were solved in the previous section ignoring the force of radiation reaction. This force is denoted as g^i and if it is taken into account, 3.1 becomes

$$m\frac{du^i}{d\tau} = \frac{e}{c}F^{ik}u_k + g^i. \tag{3.24}$$

Then g^i is given by [48]:

$$g^i = \frac{2e^2}{3c^3}\left(\frac{d^2u^i}{d\tau^2} - u^i u^k \frac{d^2u_k}{d\tau^2}\right) \tag{3.25}$$

Using the approximation that the radiation reaction force is small compared to the acceleration force, which is the first term on the right hand side in 3.25 we can use equation 3.24 without the radiation reaction term in order to substitute for $d^2u^i/d\tau^2$ in 3.25. The result is

$$g^i = \frac{2e^3}{3mc^3}\frac{\partial F^{ik}}{\partial x^l}u_k u^l + \frac{2e^4}{3m^2c^5}F^{il}F_{kl}u^k + \frac{2e^4}{3m^2c^5}(F_{kl}u^l)(F^{km}u_m)u^i \tag{3.26}$$

This is the Landau-Lifshitz approximation for the radiation reaction force [48].

For ultrarelativistic particles $u^i \gg 1$, so the third term in 3.26 dominates all others. In this

case we can write g^i as:

$$g^i = \frac{2e^4}{3m^2c^5}(F_{kl}u^l)(F^{km}u_m)u^i = -\frac{2e^4}{3m^2c^5}\gamma^2\left(\mathbf{E}+\boldsymbol{\beta}\times\mathbf{B}\right)^2 u^i \tag{3.27}$$

We see that in the ultrarelativistic limit the radiation reaction force is opposite to the velocity of the particle. The equations of motion can be then written as:

$$\frac{du^i}{d\tau'} = aF^{ik}u_k + \frac{2}{3}\alpha_f a\frac{B_0}{B_{cr}}(F^{kl}u_l)(F_{kj}u^j)u^i \tag{3.28}$$

where $\tau' = \tau\omega$ is the proper time normalized to the inverse of the wave's frequency.

We now define the invariant parameter η which we have already met in the introduction in the special case of an electron moving in a transverse electric field. In the general case it is given by the expression:

$$\eta = \frac{e\hbar}{m^2c^3}\sqrt{(F^{\mu\nu}u_\nu)(F_{\mu\lambda}u^\lambda)} \tag{3.29}$$

η determines the importance of strong-field quantum effects. It expresses the work, in units of mc^2, performed by the external field over the Compton wavelength, in the particle's rest system. In other words, η is the ratio of the external field to the critical field in the particle's rest frame. If $\eta \ll 1$ then strong-field quantum effects are negligible. As η approaches the value 1 for some parts of the electron's trajectory, then the probability of pair production either by the trident process or by the emission of energetic photons and the process of single-photon pair production becomes significant. With the help of η, g^i can be expressed as

$$g^i = \frac{2}{3}\alpha_f\frac{m^2c^4}{\hbar}\eta^2 u^i \tag{3.30}$$

The Landau-Lifshitz prescription for the radiation reaction in a plane wave field is valid if the first term dominates the second term in equation 3.24. Taking into account equation 3.30, this condition becomes $\alpha_f\eta \ll 1$ (see also [48],[7]). Already at $\eta \sim 1$, however, quantum phenomena are apparent in the particle's motion: the classical description of the trajectory is not valid anymore. In this sense, the Landau-Lifshitz formula can be used whenever the classical equations of motion are applicable to the interaction of a particle with a vacuum wave. This is the regime we will be probing in the investigation of the motion of an electron in counter-propagating laser beams: $a \gg 1$ and $\eta \lesssim 1$.

The energy lost by an accelerated particle is determined by the term g^0, which corresponds to the equation showing the variation of the Lorentz factor. The emitted power is an invariant and is given as

$$\frac{dE}{dt} = \frac{c^2 g^0}{\gamma} = -\frac{2e^2}{3c}\frac{du_k}{d\tau}\frac{du^k}{d\tau} \tag{3.31}$$

If $du^k/d\tau$ is given by the Landau-Lifshitz approximation, then the radiation calculated by 3.31 corresponds to the radiation power given by the well known Larmor formula [48].

3.3 Processes in strong static fields

The transition probabilities for various processes that an electron might undergo in the field of a plane wave are functions of the two invariant parameters already mentioned in the previous paragraphs, a and η. For arbitrary fields, the situation becomes more complicated. However, there are two simplifications one can make:

The first simplification comes from the assumption of *quasi-stationarity*: if the coherence time for an interaction is much shorter than the variation timescale of the field, then transition probabilities for the processes in an arbitrary constant field can be used. The variation timescale of the fields in laser beams is the inverse of the frequency $1/\omega$, and the coherence time is given in the quantum regime by [76]:

$$t_{\rm coh} \simeq \frac{E_{\rm cr}}{E_0}\frac{\hbar}{mc^2}$$

It can be readily shown using this expression that the condition $t_{\rm coh} \ll 1/\omega$ is equivalent to $a \gg 1$, so that for the case of strong waves the quasi-stationarity condition holds and we can use transition probabilities that are calculated for uniform, static fields [76]. It is interesting to note that this coherence time coincides with the one calculated in the classical theory of radiation, as the timescale of acceleration in a field of magnitude E_0:

$$t_{\rm coh} \simeq \frac{mc}{eE_0}$$

(see equation 3.3).

The second simplification is that of *weak fields*: if the two invariants of the field

$$f = \frac{|E^2 - B^2|}{E_{cr}^2} \tag{3.32}$$

$$g = \frac{|\mathbf{E}\cdot\mathbf{B}|}{E_{cr}^2} \tag{3.33}$$

satisfy the condition $f, g \ll 1$, and if, moreover, $\mathrm{Max(f, g)} \ll \eta^2$ then transition probabilities can be calculated as if the process was taking place in a uniform, static field [76]. Since the fields we will be discussing are in every case no greater than $10^{-3}E_{\rm cr}$, we will consider that the weak field approximation holds in our calculations. In a plane vacuum wave $f = 0$ and $g = 0$ so the weak field approximation always holds.

In the following we give the expressions for synchrotron radiation and pair production, as calculated for static fields. These are the expressions we will be using in our following calculations, where the quasi-stationarity and weak-field conditions hold.

3.3.1 Synchrotron radiation

The rate of emission of synchrotron (or magnetic bremsstrahlung) photons by electrons of energy γmc^2 which are moving perpendicularly to a magnetic field B is given, under the conditions mentioned above, by the following expression, reviewed in [20]:

$$\frac{d^2N}{d\chi dt} = \sqrt{3}\alpha_f \frac{mc^2}{h}\frac{\eta}{\gamma}\frac{F(\chi,\eta)}{\chi} \tag{3.34}$$

where the synchrotron emissivity is given by the expression:

$$F(\chi,\eta) = \frac{2\sqrt{3}}{\pi}\left(\frac{2\chi}{3\eta^2}\right)^2 \mathcal{M}(\chi,\eta) \tag{3.35}$$

$$\mathcal{M}(\chi,\eta) = M_i(\chi,\eta)J_i(\chi,\eta) \tag{3.36}$$

and summation is over $i = 1, 3$. The functions M_i, J_i are given in Appendix A. In this expression the parameter χ appears, which is analogous to η, but refers to an emitted photon instead of the accelerated electron:

$$\chi = \frac{e\hbar}{2m^3c^4}|F^{ij}k_j| \tag{3.37}$$

where k^j is the four-momentum vector of the emitted photon. There is a difference in convention for χ with respect to η, which consists in the factor 2 that appears in the denominator.

If the photon emitted has energy much lower than the electron energy, $h\nu \ll \gamma mc^2$, then the above expression can be approximated by

$$F(\chi,\eta) = \left(1 - \frac{2\chi}{\eta}\right)\kappa(2\zeta) \tag{3.38}$$

where

$$\kappa(z) = z\int_z^\infty dx K_{5/3}(x) \tag{3.39}$$

where $K_{5/3}(x)$ is a modified Bessel function, and $\kappa(z)$ is familiar from the classical synchrotron emissivity:

$$F_{\rm cl}(\chi,\eta) = \kappa(2\zeta) \tag{3.40}$$

The argument 2ζ in the above expressions becomes, in the classical limit

$$2\zeta \simeq \frac{4\chi}{3\eta^2} = \frac{\nu}{\nu_{\rm cr}}$$

where

$$\nu_{\rm cr} = \frac{3}{2}\gamma mc^2\frac{B}{B_{\rm cr}}$$

is the classical critical emission frequency which appears in $F_{\rm cl}$. We see, therefore, that the classical and quantum mechanical expressions in the limit $2\chi/\eta \to 0$ are identical.

However, when $h\nu$ is comparable to γmc^2, which means that the photon energy can be comparable to the electron's energy, the two emissivities are not similar anymore. This comes from the fact that the electron cannot emit radiation of energy higher than its own, thus giving rise to a cutoff at $\chi = \eta/2$, i.e. when $h\nu = \gamma mc^2$. This difference becomes apparent for $\eta \gtrsim 0.1$ and we show it in figure 3.3.1 for two values of η.

The cutoff in the quantum synchrotron emissivity has as a consequence that the Lorentz invariant power emitted by the particle is reduced with respect to the classical case. This can be seen in figure 3.3.1 as a reduction of the area below the emissivity curve for the quantum synchrotron case. The power emitted then, is

$$\frac{dE}{dt} = \frac{2}{3}\alpha_f\eta^2\frac{m^2c^4}{\hbar}g(\eta) \tag{3.41}$$

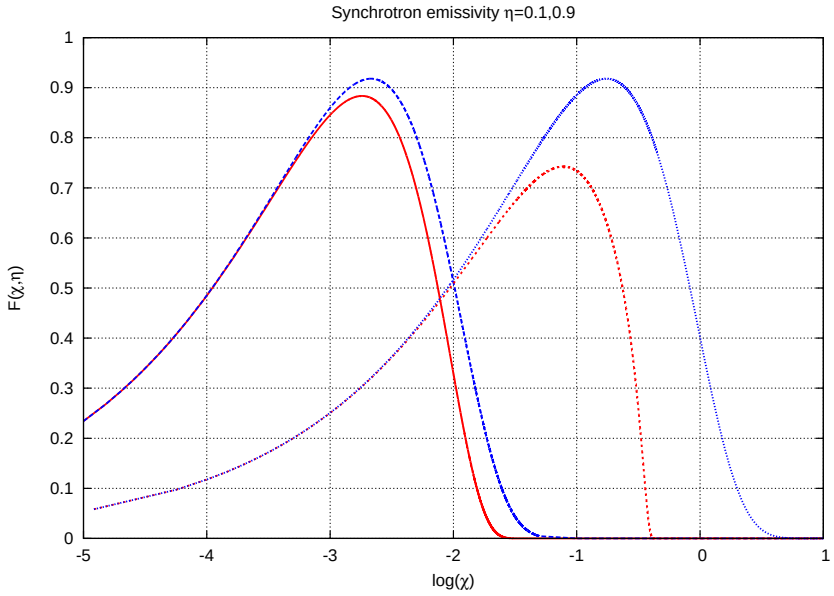

Figure 3.4: **Synchrotron emissivity in the classical and quantum mechanical case.** *The classical synchrotron emissivity is plotted in blue and the quantum mechanical formula is plotted in red for the two cases* $\eta = 0.1$ *and* $\eta = 0.9$*. The lines on the left correspond to the value* $\eta = 0.1$ *while the ones on the right to* $\eta = 0.9$*. For the curves on the right the difference between the two formulae is larger and corresponds to the fact that the energy of the emitted photon cannot exceed the energy of the emitting electron. This is why the quantum mechanical emissivity (red line) falls to the value of zero above* $\chi = 0.5$*.*

where

$$g(\eta) = \frac{3\sqrt{3}}{2\pi\eta^2}\int_0^\infty F(\eta,\chi)d\chi \tag{3.42}$$

In the classical case the power is given by 3.41 with $g(\eta) = 1$. For small η the function $g(\eta)$ can be approximated by

$$g(\eta) \simeq 1 - \frac{55\sqrt{3}}{16}\eta \tag{3.43}$$

3.3.2 Pair production in strong static fields

There are two processes which are relevant for pair production in the context of the interaction of particles with vacuum waves. The first is trident pair production, which involves intermediate virtual photons, and the second is pair production by the real synchrotron photons that are emitted by the electron in the field of the laser beams, according to the formulae described above. We give the pair production rates for these processes immediately below.

Trident pair production

The trident pair production rate for an electron of energy γmc^2 is given by Erber [20]:

$$\frac{dN_{tr}}{d\tau} = 0.64\frac{mc^2}{h}\alpha_f^2\eta\hat{\Omega}(\eta) \tag{3.44}$$

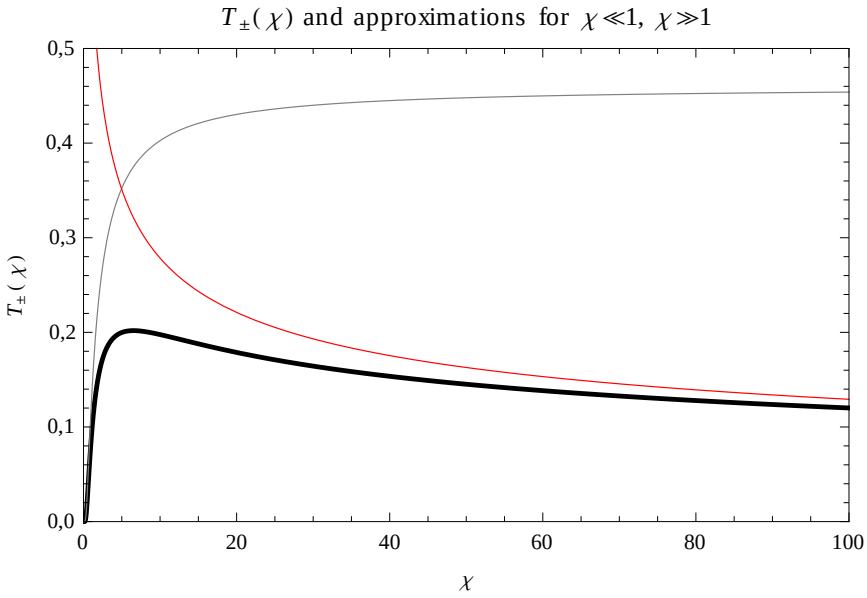

Figure 3.5: **The function $T_\pm(\chi)$ and its approximations for $\chi \ll 1$ (gray), $\chi \gg 1$(red).**

where N_{tr} denotes the number of pairs produced. Here we give the invariant rate per proper time. The function $\hat{\Omega}$ is given in Appendix A, and for small η can be approximated as

$$\hat{\Omega}(\eta) = \frac{\pi^{5/2}}{16}(3\eta)^{1/4} \exp\left(-\frac{8}{\sqrt{3\eta}}\right) \tag{3.45}$$

Single photon pair production

Energetic photons emitted by the accelerated particles in the field of a laser can lead to pair production. The attenuation coefficient is a function of the dimensionless photon energy χ and the photon energy $h\nu$ and is given by Erber [20] as

$$\frac{d\tau_\nu}{dt} = \frac{\alpha_f}{\lambda_c}\frac{mc^2}{h\nu}\chi T_\pm(\chi) \tag{3.46}$$

where τ_ν is the optical depth of photons of energy $h\nu$. The function $T_\pm(\chi)$ is given approximately as

$$T_\pm(\chi) \simeq 0.16\frac{1}{\chi}K_{1/3}^2\left(\frac{2}{3\chi}\right) \tag{3.47}$$

where $K_{1/3}(x)$ is the modified Bessel function of the second kind.

In the limits $\chi \ll 1$ and $\chi \gg 1$ we have

$$T_\pm(\chi \ll 1) \simeq 0.46 \exp\left(-\frac{4}{3\chi}\right) \tag{3.48}$$

$$T_\pm(\chi \gg 1) \simeq 0.6\chi^{-1/3} \tag{3.49}$$

The maximum of the attenuation coefficient 3.46 with respect to the photon energy is at the value $\chi \sim 6$.

Chapter 4

Pair production in laser experiments

4.1 Pair production techniques

In the past few years, there have been reports of pair production in several experiments using laser beams. The idea behind these experiments is to use laser beams either as targets for relativistic electrons, or as the means to accelerate electrons.

The most well-known example of the first case is an experiment performed in the Stanford Linear Accelerator Center, where 46.6GeV and 49.9GeV electron beams from the linear accelerator were fired against an infrared and a green laser beam, of respective wavelengths 1053 and 527 nm [11]. In this experiment two strong-field processes were observed: non-linear Compton scattering, and multi-photon Breit-Wheeler pair production.

These two processes have been introduced in the previous chapter, where we were concerned with their mathematical formulation in the limit of large strength parameter, where the trajectory of a particle in an external wave field can be treated classically, if $\eta \lesssim 1$. However, in the SLAC experiment, the intensity of the beam was not high enough to achieve $a \gg 1$. The strength parameter, using the definition involving the root mean square field

$$a = \frac{eE_{\text{rms}}}{mc\omega} \tag{4.1}$$

was only just comparable to unity, in the transition regime between weak and strong waves. For $a \sim 1$ only a few beam photons are participating in each process. Non-linear Thomson scattering, in this case, refers to the scattering of a small number n of laser photons (symbolized as ω, which is the laser frequency) by a relativistic electron to produce a high energy photon (denoted as γ):

$$e + n\omega \Rightarrow e' + \gamma \tag{4.2}$$

Multi-photon Breit-Wheeler pair production is the process, in which the high-energy photon previously emitted by the process of non-linear Compton scattering, interacts with more than one low-energy beam photons to produce an electron-positron pair:

$$\gamma + n'\omega \Rightarrow e^+e^- \tag{4.3}$$

The strength parameter achieved in the SLAC experiment was $a \simeq 0.4$ corresponding to

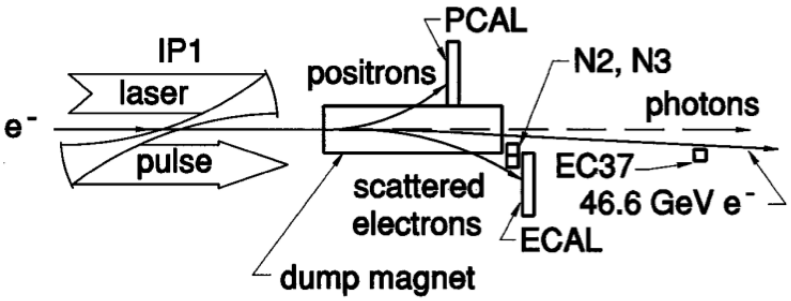

Figure 4.1: **Schematic representation of the SLAC experiment.**
A high intensity laser beam is fired into an electron beam from a linear accelerator. High energy photons scattered by the non-linear Thomson mechanism are observed downstream of the particle beam, while positrons created by the non-linear Breit-Wheeler process are deflected by magnets and measured in the calorimeter PCAL. The figure is taken from [11].

peak laser intensities in the vicinity of $10^{18}\mathrm{Wcm}^{-2}$. It was calculated that on average $n = 1.5$ laser photons were scattered in process 4.2 and $n' = 4.7$ were absorbed in process 4.3 to produce $e^+ - e^-$ pairs. In this experiment non-linear QED phenomena in vacuum were observed for the first time.

Another way to produce pairs is to use the laser not as a target but as an accelerator. This is based on the fact that a particle interacting with a strong intensity laser beam recoils in the direction of the beam, as explained in Chapter 3. When the laser is focused on a solid target of large atomic weight electrons from the surface of the target are accelerated and radiate bremsstrahlung photons in the field of the heavy nuclei. These photons in their turn can produce pairs in the electrostatic field of the nuclei (Bethe-Heitler process), while the electrons themselves produce pairs via the trident process. This way pair cascades are initiated which result in the production of a substantial number of positrons.

In one such experiment a short-pulse laser beam of intensity $\sim 10^{20}\mathrm{Wcm}^{-2}$ was used to initiate cascades in an Au (gold) target [12]. The positron density achieved was estimated to be of the order of magnitude $10^{16}\mathrm{cm}^{-3}$ inside the target, and the positrons achieved kinetic energies up to 50MeV. A strong anisotropy in the angular distribution of the emerging positrons was observed, with the largest numbers observed at the rear of the target. This was considered to be an indication of jet-like expulsion of positrons from the target. A schematic representation of the setup of the experiment is shown in figure 4.2.

A third mechanism which, however, cannot be tested in the laboratory yet, is pair production out of the vacuum, as predicted by Schwinger [78]. While this process cannot operate in a single beam because of the violation of momentum conservation, it can operate in counter-propagating beams of intensity $\sim 10^{29}\mathrm{Wcm}^{-2}$ which corresponds to the critical Schwinger field, $E_{\mathrm{cr}} = 1.3\times10^{18}\mathrm{Vm}^{-1}$. Such intensities are unattainable with today's means or in the foreseeable future. For this reason we will focus on the mechanisms of pair production mediated by relativistic electrons, as described above.

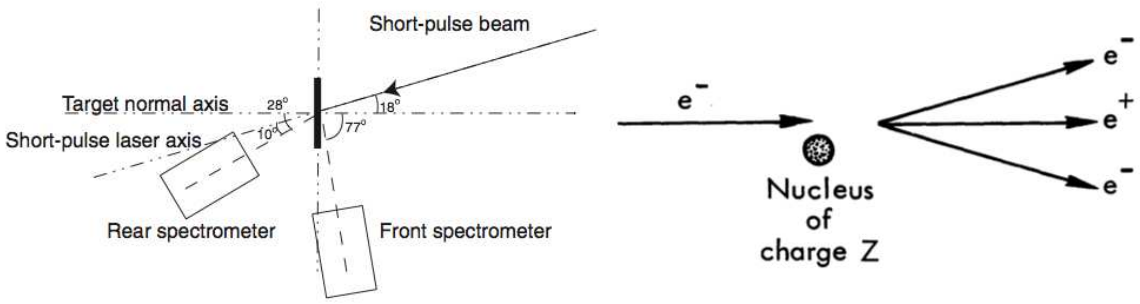

Figure 4.2: **Positron production by interaction of a high intensity laser with a heavy target.**
The figure on the left is taken from [12]. It shows the configuration of the experiment in which pair production was achieved by firing a laser to a gold target. On the right a sketch of the mechanism of trident pair production in the field of a nucleus is shown, taken from [80].

4.2 Counterpropagating beams

An electron which is picked up by a laser beam is accelerated in the direction of propagation of the beam to a center-of-momentum Lorentz factor that is of the order of magnitude of the strength parameter: $\gamma_{\rm com} \sim a$. These electrons acquire large energies. Nevertheless, because of this recoil the fields of the beam are weakened in the electron center of momentum frame, and the wave itself appears redshifted. The field in the electron center of momentum (COM) frame is of the order of magnitude $E' \sim E/a$.

Because of this, the parameter η which is crucial for pair-production becomes $\eta \sim aa^{-1}E/E_{\rm cr} = E/E_{\rm cr}$ for a particle in a single laser beam. This is unfavourable for pair production: the momentum gain from the particle recoil in the laser beam is counteracted by the reduction of the field in the COM frame. A configuration is needed, for which the product of the Lorentz factor and the perpendicular field in the COM frame becomes comparable to the critical field.

In the experiment where a laser beam was fired at a solid target, the laser was used as an accelerator of electrons, while the heavy nuclei of the target provided the strong electrostatic field in which pair production could occur. In the SLAC experiment, the electrons were accelerated by a linear accelerator and fired against a laser beam. The laser in this case was used as a target, and its field appeared boosted in the electron COM frame, creating conditions favourable for pair production.

However, a potentially more efficiently and easily achievable configuration is to use laser beams of the same intensity, and thus of the same strength parameter, both as accelerators and targets as proposed in [7]. In this configuration because of the equal strength of the counter-propagating waves, the COM frame coincides with the laboratory, and the perpendicular field in the electron rest f frame becomes of the order of magnitude of the laboratory field times the center-of-momentum Lorentz factor of the particle: $\eta \sim \gamma b$, where $b = B_0/B_{\rm cr}$ and B_0 is the field amplitude in the laser beam. This way, for beams of $a \gg 1$, even with fields of amplitude much lower than the critical value $E_{\rm cr}$, it is possible for η to approach unity, giving rise to observable strong field phenomena.

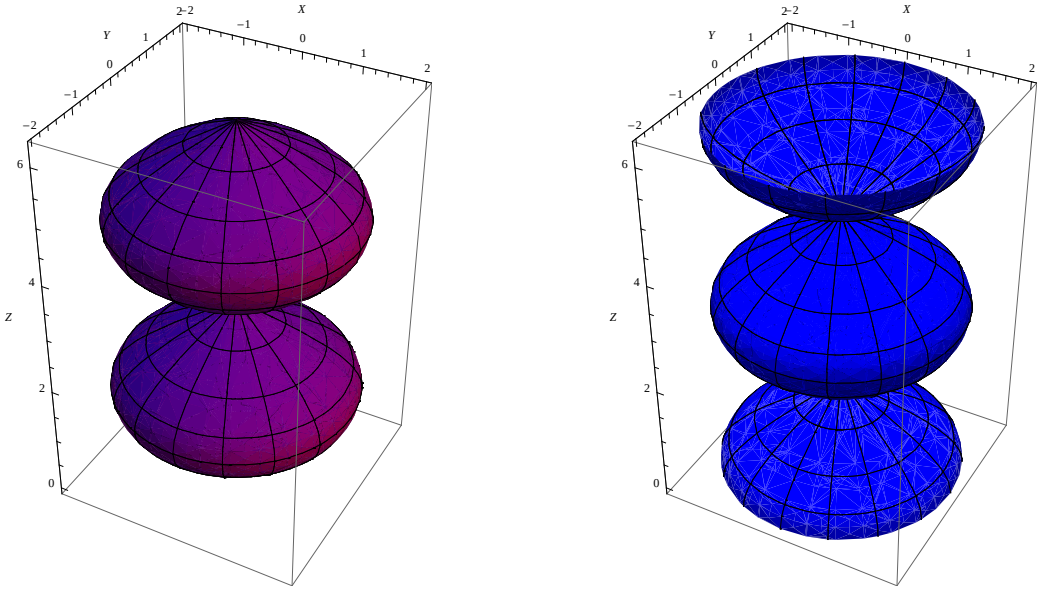

Figure 4.3: **Contours traced by the tips of the electric and magnetic field vectors in one 2π rotation.**
In the case of circularly polarized beams, with one being left-handed and the other right-handed, the result is a sinusoidal wave that rotates around the axis of the beams. The field amplitude is constant in every point along the beam and rotates in one laser period. The amplitude at each point ranges from 0 to $2E_0$, with E_0 the single beam amplitude.

4.2.1 The paradigm of circular polarization

Bell and Kirk [7] estimated pair production initiated by electrons in counter-propagating beams using as an example the trajectories of particles in the $B-$nodes of two counter-propagating circularly polarized beams of equal frequency and intensity. The beams were assumed to be monochromatic, infinitely long plane waves and to have polarizations of opposite handedness, so that in the magnetic field node the electric field has constant magnitude equal to $2E_0$, where E_0 is the amplitude of each beam, and rotates by 2π in one laser period. The contours of the standing wave are seen in figure 4.3.

The trajectories of electrons in the magnetic nodes are simple: the electric force is providing the centripetal acceleration, and the particles perform circular motion around the node, with a period of $2\pi/\omega$, where ω is the laser angular frequency. The radiation reaction force for relativistic particles is, as has been discussed in the previous chapter, very nearly opposite to the direction of motion, so the electric field is not perpendicular to the particle's velocity: there is a parallel component which exactly compensates the radiation reaction force, and it is the perpendicular field that provides the centripetal acceleration. The particle's Lorentz factor is $\gamma = a \sin\theta$, where θ is the angle between the electric field and the particle's velocity. In this case

$$a = \frac{2E_0 e}{mc\omega}$$

where E_0 is the field amplitude in each beam.

In [7] the criterion was set that the motion is radiation reaction dominated if $\theta < \pi/4$. From equation 3.28 it is seen that according to this criterion radiation reaction becomes important for

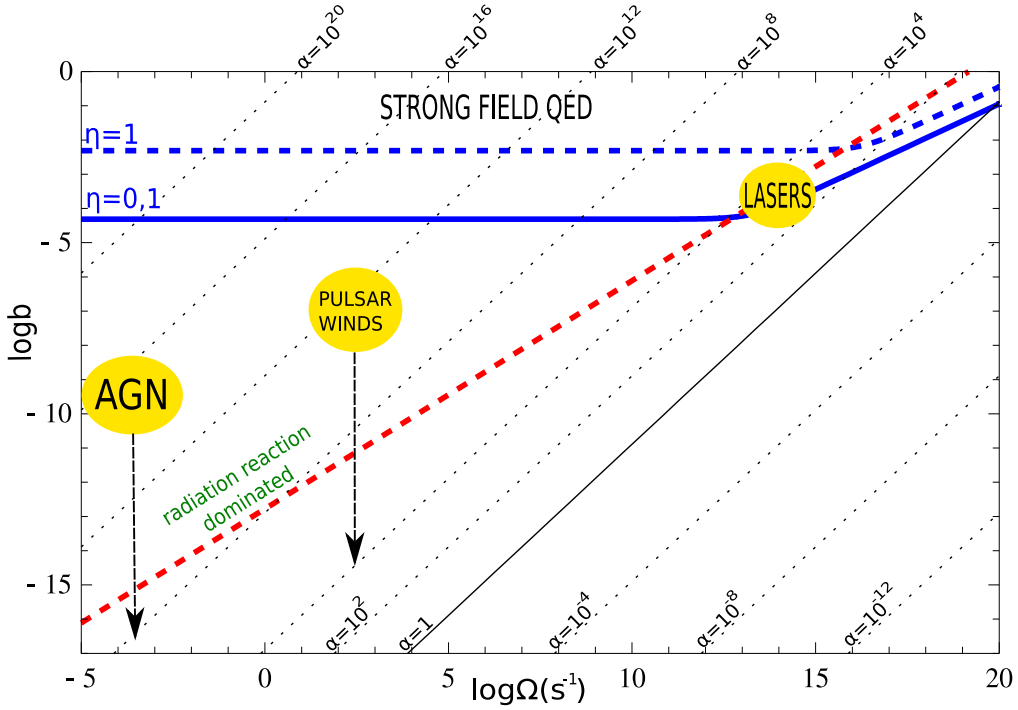

Figure 4.4: **Strength parameter lines on a wave amplitude-frequency plot.** *The field is given in units of the critical field, $b = B_0/B_{\rm cr}$. The dashed red line $\theta = \pi/4$ separates the regions of dominant and non-dominant radiation reaction. Roughly above the line of constant η, $\eta = 0.1$ lies the region where strong field QED phenomena are expected. Next generation lasers of wavelengths of the order $\sim 1\mu$m and intensity $10^{23} - 10^{24}$Wcm^{-2} fall into the region of strength parameter $10^2 - 10^4$, and at the edge of the dominant radiation reaction and strong field QED regions. The regions marked as AGN and PULSAR WINDS are drawn taking into account the rotation frequency of the compact object (supermassive black hole and pulsar, respectively) and a typical field value at the light cylinder of each object. The arrows then show the direction of decrease in the strength parameter as one moves away from the compact object towards regions of reduced field. The paradigm of circularly polarized counter-propagating beams does not necessarily apply to the astrophysical objects: their presence on their diagram serves the purpose of showing the strength parameters of waves associated with them.*

$\alpha_f \gamma^2 E/E_{\rm cr} \sim 1$ or $\alpha_f \gamma^2 b \sim 1$. This corresponds to

$$\eta \sim \frac{1}{\alpha_f \gamma}$$

Since the particle trajectories are identical to those when gyrating around magnetic field lines, it is straightforward to calculate the peak frequency emitted according to the classical synchrotron formula. The energy of the emitted photons corresponding to this frequency is [7]:

$$h\nu_s = 0.29\frac{3}{2}\gamma^2 b \sin\theta mc^2 = 0.435\eta\gamma mc^2$$

For the intensities that interest us, $10^{23} - 10^{24}$Wcm^{-2}, η is less than unity and the emitted photon energies are about one order of magnitude lower than the electron energy, justifying the classical approach for the trajectory calculation. Bell and Kirk predicted that at the intensity

$10^{24}\mathrm{Wcm}^{-2}$ about one electron-positron pair would be created during one gyration of a particle in the node of two counter-propagating lasers of wavelength $1\mu m$. A cascade would then develop which would feed on the lasers energy. The dominant process at these high intensities is pair production via real synchrotron photons: the trident effect is more important at intensities close to $10^{23}\mathrm{Wcm}^{-2}$, while pair production via real photon starts dominating already at $3 \times 10^{23}\mathrm{Wcm}^{-2}$ [7].

In figures 4.4 and 4.5 contours of constant γ, a and $h\nu_s$ are plotted, for a range of field strengths b and angular frequencies Ω. The plots are made using the simple results from the above calculations of particle motion and radiation in the $B = 0$ nodes of two counter-propagating beams of opposite circular polarization. The position of next generation lasers of intensity $10^{23} - 10^{24}\mathrm{Wcm}^{-2}$ is shown in the diagrams, along with the position of two astrophysical sources which might be able to emit strong circularly polarized waves in vacuum: AGN stands for Active Galactic Nuclei, in which case the source of the waves would be a rotating supermassive black hole. In the case of pulsar winds, the source is a magnetized rotating neutron star. For the astrophysical sources, Ω is the rotation frequency of the compact object, which imposes the frequency of the emitted wave.

4.2.2 In search of more realistic beam configurations

The analysis of Bell and Kirk showed that electrons accelerated in the field of counter-propagating laser beams of intensity $10^{23} - 10^{24}\mathrm{Wcm}^{-2}$ can initiate pair cascades which might be capable of depleting the beams of their energy.

However the phenomena described in the previous paragraph are sensitive to the beam geometry, and can only be significant at the rather limited area in the focus of the two counter-propagating beams. Also, particles in vacuum waves generally drift in the perpendicular direction to the wave propagation and might leave the region of strong field in the matter of a few laser periods, or even a fraction of a period. The pulse trains are neither infinite, nor monochromatic, but contain a certain spectrum of frequencies and have a finite duration. All these characteristics of laser pulses should be taken into account in a more detailed calculation.

The most serious drawback of the two counter-propagating, circularly polarized beams configuration, however, comes from the choice of polarization: trajectories directly at the nodes are unstable, and particles beginning their motion anywhere but exactly on a magnetic field node drift away from it and settle on the electric field node after some oscillations around it. The number of pairs produced by these particles is quickly saturated, because the particles radiate less and less until they come to rest at the electric node. This is one of the reasons that circular polarization is not the most favourable for pair production.

In figures 4.6 and 4.7 this effect of saturation is shown.

In figure 4.6 the number of pairs as a function of intensity is shown, after 5 laser periods from the beginning of motion. The particle is started from rest at three different points along the beams: a magnetic node, at $\lambda/5$ and at $\lambda/10$ from the magnetic node, where λ is the wavelength of the laser beams. The results have been calculated assuming that the beams are very long, monochromatic plane waves of transverse radius $R = \lambda$. We can see that the farther the particle is initially from the node, the fewer pairs are created through real photons at a given intensity.

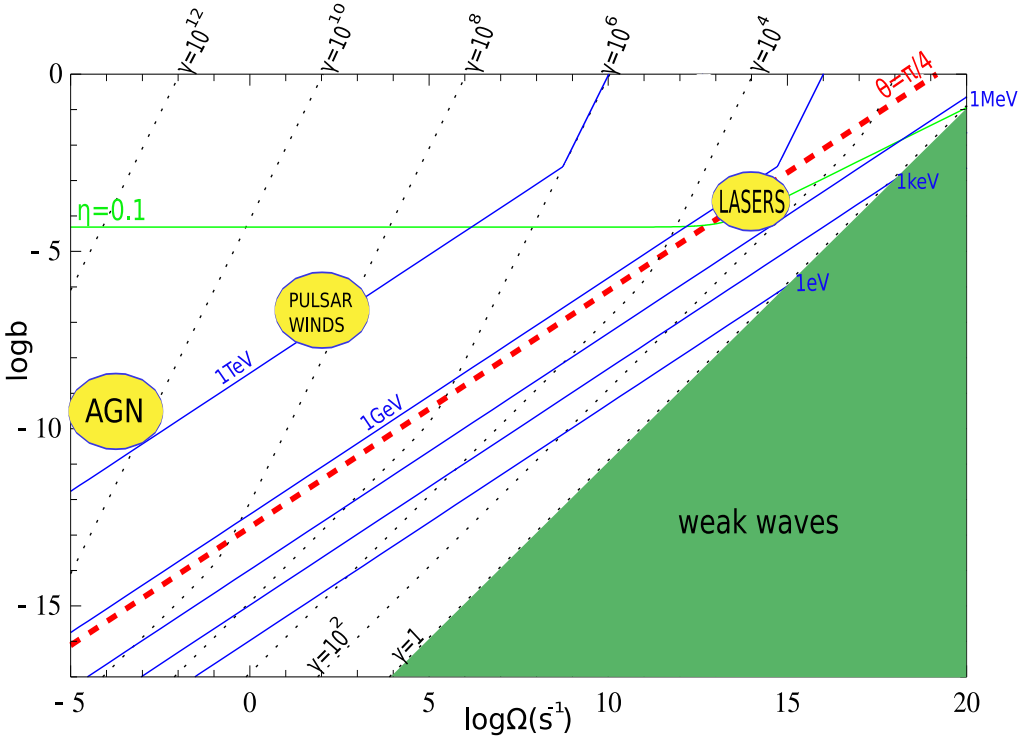

Figure 4.5: **Emitted photon energy contours on a field amplitude-wave frequency plot.**
The blue lines indicate the peak photon energies emitted according to the classical synchrotron formula. The region below $a = 1$ is shaded and corresponds to the weak waves. The dashed lines are contours of the constant Lorentz factor of particles gyrating in the nodes of counter-propagating circularly polarized vacuum waves. The regions denoted as AGN and PULSAR WINDS have the same meaning as in figure 4.4. For the next generation lasers, the Lorentz factors of electrons gyrating in the B-nodes is going to be of the order of magnitude $10^2 - 10^3$. The synchrotron photons emitted have energies in the range of MeV to GeV, and are energetic enough to start pair cascades.

The number of pairs created through a real synchrotron photon versus time in units of periods is shown in figure 4.7 for intensity $10^{24}\mathrm{Wcm}^{-2}$ for the same initial positions as those used for figure 4.6. It is readily seen that away from the node the pair number is smaller and saturates within a fraction of a period, close to the node it saturates somewhat later, but at the node it keeps rising linearly with time. All trajectories initiated away from the $B = 0$ node are going to drift away from it and towards the $E = 0$ node (see also [44]).

The problems of beam geometry and perpendicular drift are similar for all beam polarizations, but the beam polarizations can be changed. Linear polarization is easier to create in the laboratory, and the setup of counter- propagating beams can be achieved, for example, by reflecting a laser pulse off a solid target. In this case the reflected beam is going to have the same polarization as the incoming one. Therefore, in the following chapter we will investigate electron trajectories and pair production in several configurations of counter-propagating beams of linear polarization. The results will then be used to predict the possibility of development of pair cascades using future laser facilities in the intensity range $10^{23} - 10^{24}\mathrm{Wcm}^{-2}$.

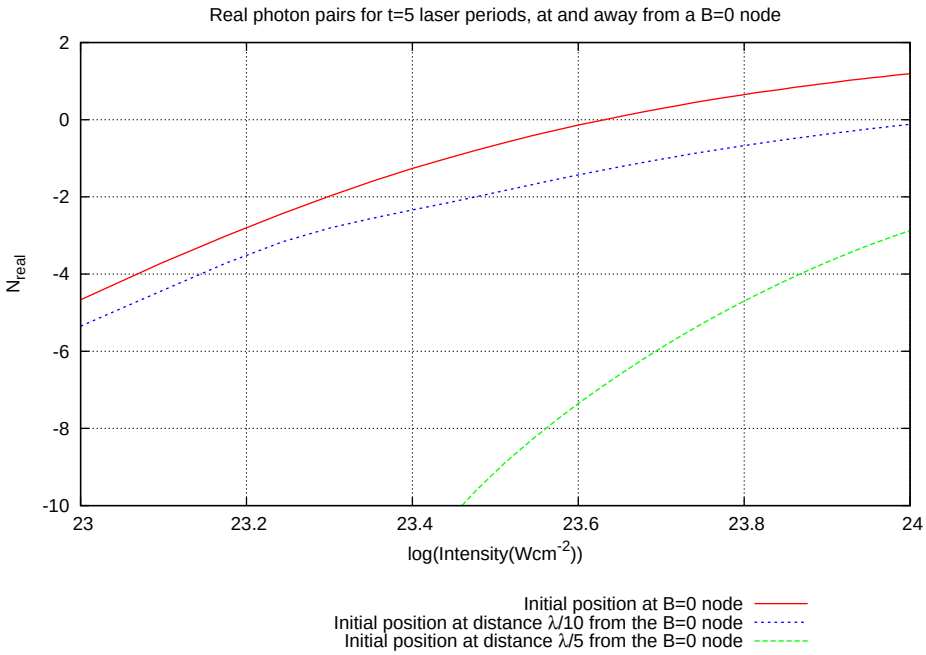

Figure 4.6: **Pair production at and away from an $B = 0$ node as a function of beam intensity.**

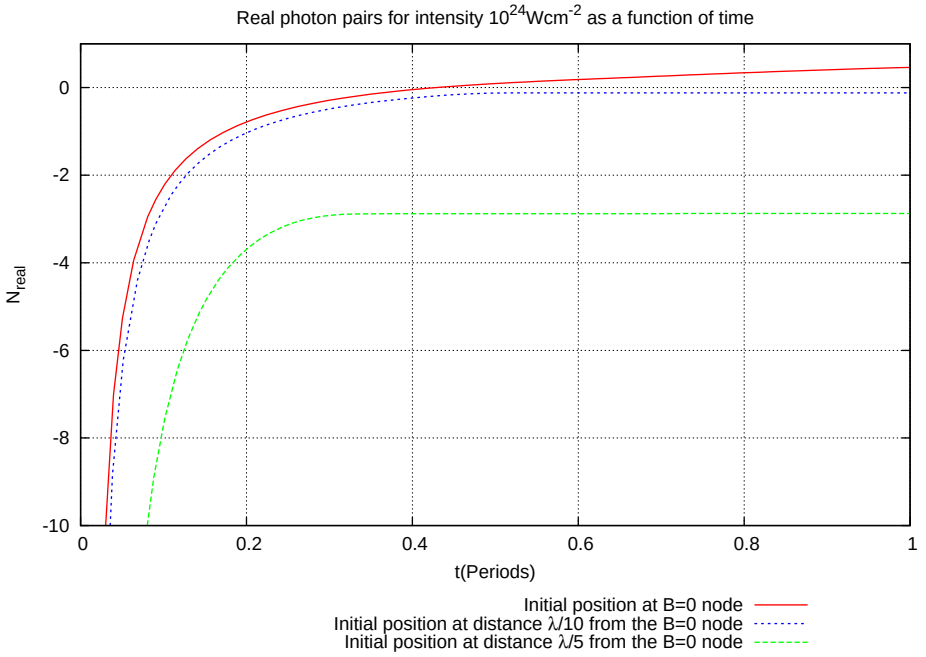

Figure 4.7: **Pair production at and away from an $B = 0$ node as a function of time for intensity $10^{24}\mathrm{Wcm}^{-2}$.**

Chapter 5

Calculation of pair production

The strength parameter of a laser pulse, expressed as a function of its intensity and its wavelength, was given in equation 1.5. For beams of wavelength $\sim 1\mu$m and intensity $0.1 < I_{24} < 1$ with I_{24} the intensity in units $10^{24}\mathrm{Wcm}^{-2}$ the quasi-stationarity condition $a \gg 1$ which we introduced in Chapter 3 is well satisfied. This means that one can use the transition probabilities calculated for a particle in a static field, as described in the same chapter. Also the largest value that the invariants f, g can assume in counter-propagating beams of such intensities is of the order of magnitude $\sim 10^{-5} I_{24}$. This means that the weak field approximation also holds, so that we can use the formulae of Chapter 2 for the calculation of radiation and pair production. The motion of an electron in the field of the lasers is described classically, something that is a reasonably good approximation as long as the parameter η that determines strong-field quantum effects is not too large, $\eta \lesssim 1$.

It is true that in our calculation there exist points in space and time where the electric and magnetic fields are simultaneously zero. At those points, the coherence time, defined in Chapter 3, is not small anymore, however processes relevant to the phenomena we are investigating (radiation of high energy photons and pair production) are suppressed because of the weakness of the fields. This is why the quasi-stationarity approximation is still generally valid for counter-propagating vacuum waves of large strength parameter. A similar argument applies to the largeness of η^2 as compared to the invariants f and g: in the points where η is small, pair production is suppressed anyway: strong-field QED effects start appearing at $\eta \sim 0.1$. For these values the weak-field condition always holds.

In the following sections, we will describe the numerical calculation of electron trajectories and the possibility of pair production caused by the radiated synchrotron photons in the field of two counter-propagating laser beams. The results of this work were published in Kirk et al. 2009 [44].

5.1 Set-up of the model

In order to achieve meaningful results, realistic models of laser beams have to be used in the numerical calculations. We improve on the calculations of Bell and Kirk 2008, [7], by examining three different possible experimental configurations.

The first two involve counter-propagating laser beams of frequency ω, in the first case with

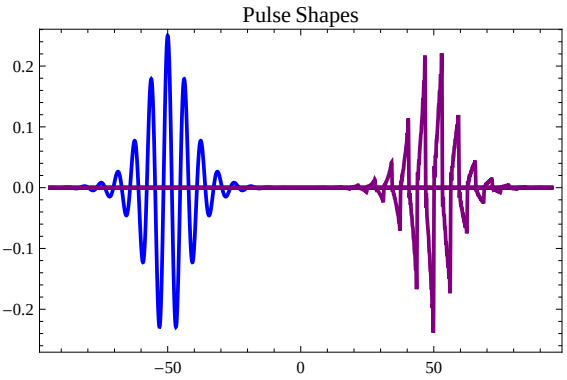

Figure 5.1: **Examples of pulses.**
On the left an example is shown of a harmonic wave folded with an envelope function, equation 5.2. On the right a pulse is shown which is simulating a laser beam being reflected off a solid target, equation 5.1, also folded with the same envelope function. The two pulses are not plotted to scale.

parallel linear polarizations and in the second with crossed polarizations, i.e. the polarization vectors are in right angles to each other. In the third case the polarizations are again aligned, but one of the pulses contains higher harmonics, in order to simulate a pulse that has been reflected off a solid target. The Fourier series representing this wave is [4]:

$$\mathbf{E} = \hat{\mathbf{e}}\frac{2}{\pi}\sqrt{\frac{\sqrt{3}}{2}}f(\phi)\left(\sum_{n=0}^{n_{max}}\frac{\sin[(2n+1)\phi]}{2n+1} - \frac{2\cos[(2n+1)\phi]}{\pi(2n+1)^2}\right) \tag{5.1}$$

where ϕ is the phase of the wave and $\hat{\mathbf{e}}$ is a unit vector in the direction of polarization of the wave. We continue to normalize space to c/ω and time to $1/\omega$, with ω the frequency of the monochromatic wave that represents the beam, so that phase becomes $\phi_+ = t - z$ for a wave propagating in the positive $z-$direction and $\phi_- = z + t$ for the counter-propagating pulse.

To take into account the finite duration of the pulses, we fold the monochromatic wave or, in the reflected wave case, the Fourier series, with an envelope function:

$$f(\phi) = \frac{1}{4}\left[1 \mp \tanh\left(\frac{\phi}{\Delta}\right)\right]\left[1 \pm \tanh\left(\frac{\phi \pm L}{\Delta}\right)\right] \tag{5.2}$$

where ϕ is the phase of a pulse, L is the length of the pulse in phase units, and Δ is the thickness of the pulse edges, which shows how sharp the decrease is. In 5.2 the upper signs refer to the pulse propagating in the positive direction, while the lower signs refer to the one propagating in the negative direction. The reflected wave is, of course, also folded with the envelope function.

The pulses have also a finite transverse dimension. It is important to take this into account, since electrons accelerated by vacuum waves drift perpendicularly to the propagation direction of the beam, with the result that they might leave the pulse before they reach the interaction region of the two pulses where radiation and pair production should take place. We do not take into account the transverse decrease in intensity, however we assume a finite radius of the beam within which the intensity is constant: this radius is set to be equal to one wavelength, and trajectories of particles that drift out of a cylinder of this radius are terminated.

The electron trajectories are started from rest and are numerically calculated using equation 3.24 with radiation reaction given by the Landau-Lifshitz prescription 3.26. The parameter η is calculated in every step, and the radiation reaction terms are multiplied by the function $g(\eta)$ given by 3.42 in order to take into account the reduction in emitted power in the strong field regime.

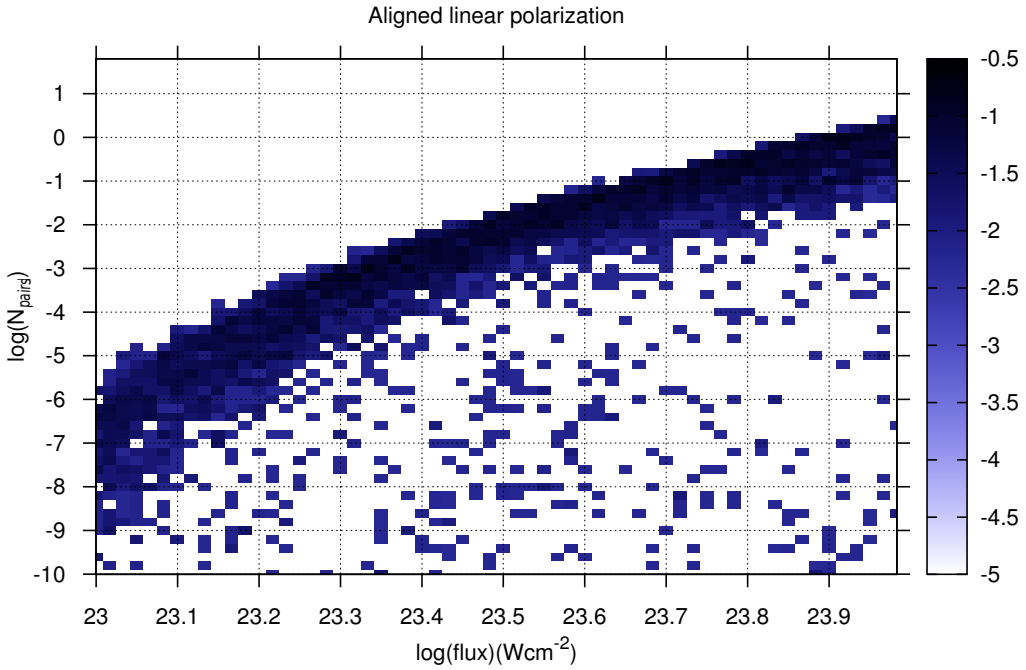

Figure 5.2: **Probability of pair production for aligned polarizations.**
The two pulses have aligned polarizations and the same shape. Plotted is the logarithm of the probability that a certain number of pairs per electron is going to be produced for the initial conditions described in the text.

When η is close to 1, the energy spread of the electrons becomes wider, leading to the possibility of emission of photons of higher energies. This is an effect of the quantum mechanical nature of radiation: the emission is no more continuous but episodic, and stragglers could emit a photon of large energy, leading to a higher possibility of pair production, as investigated by Shen and White [81]. However in this calculation we don't take such effects of discreteness into account.

5.1.1 Calculation of pair production

We have calculated the amount of pairs created by both the process of trident pair production, and the process of pair production via real photons, as described in Chapter 2. Trident pair production is directly calculated by equation 3.44. For the pair production by real photons, we have to make use of the optical depth which is given by equation 3.46:

$$\tau(\nu) = \frac{\alpha_f}{\lambda_c}\frac{mc^2}{h\nu}\int_{t_0}^{t_{\rm esc}} dt\chi(t)T_{\pm}(\chi(t)) \tag{5.3}$$

where the integration has to take place over the straight trajectory of the photon from the point of its emission t_0 at the point (x_0, y_0, z_0) to its leaving the beam at time $t_{\rm esc}$. Along this trajectory χ changes, because although the frequency of the photon ν remains constant, the perpendicular field that goes into the calculation of χ is a function of space and time:

$$\chi(t) = \frac{h\nu}{2mc^2}\frac{\mid \mathbf{E}_{\perp} + \mathbf{k}\times\mathbf{B} \mid}{E_{\rm cr}} \tag{5.4}$$

where **k** is the unit vector along the photon's momentum. This is found assuming that in every point in space and time, photons are emitted parallel to the instantaneous direction of motion of the emitting electron. The number of pairs which are produced by synchrotron photons can then be calculated by integrating the synchrotron photon spectrum over the range of photon energies from $\chi = 0$ to the maximum value of $\chi = \eta/2$, weighted by the probability of the photon being absorbed and creating a pair, which is $1 - e^{-\tau}$:

$$\frac{dN_r}{dt} = \int_0^{\eta/2} d\chi \frac{dN}{d\chi dt} \left(1 - e^{-\tau}\right) \tag{5.5}$$

Pair production stops when the photons leave the cylindrical region of radius λ since we assume that the fields vanish there.

In the above calculation the quantum synchrotron spectrum was used, and the radiation reaction was folded with the function $g(\eta)$, in order to normalize the energy losses to the quantum formula.

5.2 Computation and results

The equations of motion of the electrons, 3.24, along with the equations governing pair production by the trident process and by real photons, were integrated numerically using the Bulirsch-Stoer algorithm [74]. The interaction point of the pulses, defined as the point in space where the two pulses completely overlap, if they have the same shape and polarization was set to be $z = 0$. The length of the pulses was set to be $L = 10\pi$ and the thickness of the edge of the pulses was $\Delta = 10\pi/3$, with L and Δ in phase units.

The pulses were started far away from the interaction region, and the electrons were started from rest, in a region between the pulses. Because of their perpendicular drift, only electrons that start off near the interaction region, where strong field effects are important, have a chance of reaching it. This is why we started the electrons within an interval of a few wavelengths around the interaction region.

In order to get results referring to the probability of pair production in counter-propagating beams, we started 10^5 particles in the region between the pulses, with random initial positions. The coordinates x and y were randomly chosen within a circle of radius one wavelength, $x^2+y^2 = \lambda^2$, while the coordinate along the propagation direction of the laser was chosen randomly in the interval $-8\lambda < z < 0$. Also, the single beam intensity was chosen randomly in the interval $10^{23} - 10^{24}\mathrm{Wcm}^{-2}$. The variation in intensity will give information about the critical intensity, where a cascade is likely to be initiated by particles in the beams.

In the figures 5.2, 5.3, 5.4 the results of our calculation can be seen. In these figures we show in colour-coded plots the logarithm of the probability that a certain amount of pairs will be created for a given logarithmic intensity interval, for the three beam configurations that we have chosen. This probability is calculated by dividing the number of trajectories at a certain interval of beam intensity that have given a certain number of pairs by the total number of trajectories in the given intensity interval.

In the case of aligned polarizations and of the reflected beam, roughly 83% of all particles leave the laser volume without having triggered pair production. In the case of the crossed

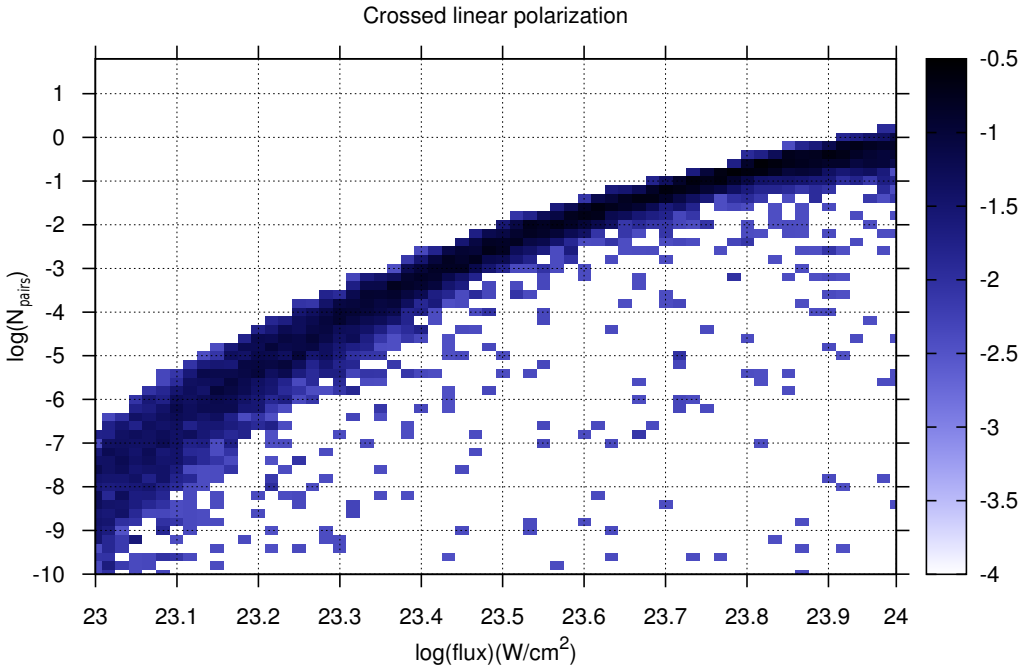

Figure 5.3: **Probability of pair production for crossed polarizations.**

polarization this percentage is close to 75%. It can be seen from figures 5.2,5.4 and 5.3 that the probability for the creation of one pair becomes substantial only for the highest intensities.

At $I_{24} \sim 0.86$ for the case of aligned linear polarization, a threshold is reached: the probability for the creation of one pair per electron is ~ 0.3. This means that for every 10 electrons initiated in a small region of the beam around the interaction point, three are going to produce electron-positron pairs, i.e a number of pairs is expected to be produced of the order of magnitude of the initial number of pairs in the beam. Moreover, some of these secondary particles, which are produced in a strong field region, might produce pairs themselves. This is why it is reasonable to assume that for intensities larger than this value, the phenomenon is going to have as a result the production of more pairs than the ones injected in the laser beams and lead to a pair avalanche at the focus of the beams, fed by the beams' energy. For the case of the interaction of a laser with a beam reflected by a solid target, the probability of the production of one pair by one electron becomes unity at intensity $10^{24}\mathrm{Wcm}^{-2}$.

Why we expect cascading

Although we haven't conducted a calculation of cascading in the laser beams, it is quite likely that the phenomenon of pair production is going to be multiplied, possibly until the beams' energy is depleted. Pair production happens in the interaction region of the beams. The pairs that are produced are already in a region of high field intensity, and they are going to be accelerated within a fraction of the laser's period. Since the interaction of the beams lasts for several periods, there is enough time for the process to be repeated several times: the secondary particles will be accelerated themselves, and lead to pair creation of their own. The process will continue until the pulses have separated.

For the higher intensities, close to $10^{24}\mathrm{Wcm}^{-2}$, the probability of pair production by an

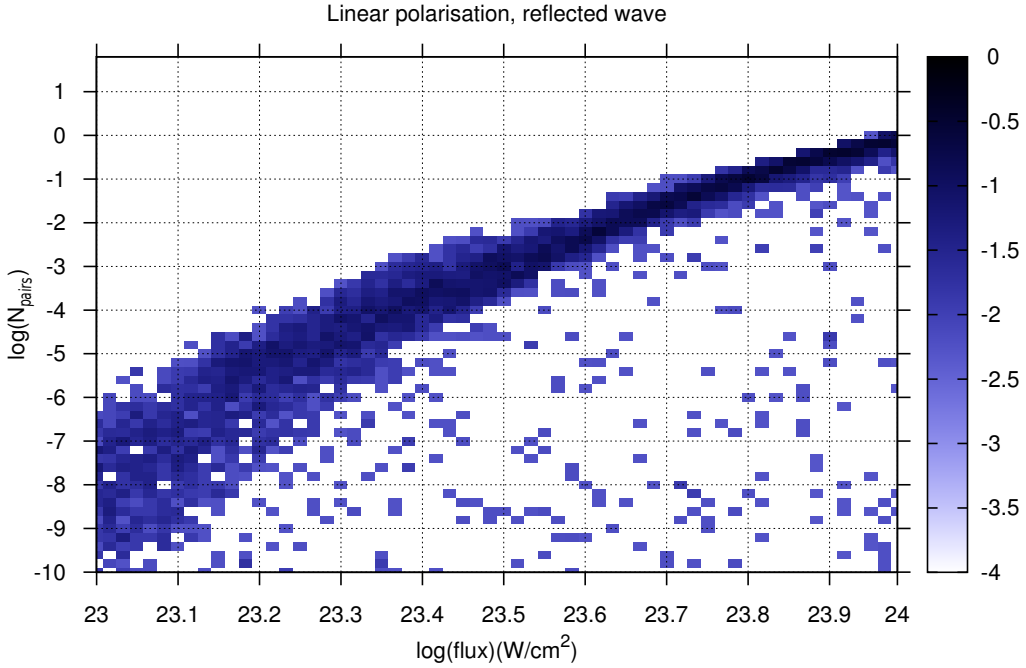

Figure 5.4: **Probability of pair production for aligned polarizations, with one beam reflected off a solid target.**

electron approaches unity. This can lead to exponentiation of the process, since every particle now produced is going to pair-produce itself. The cascading process feeds on the beams' energy and might deplete it, if intensities are high enough for rapid pair production to occur. A calculation of the critical intensity for the development of a QED cascade was undertaken in [21], which, however, gave a threshold of $10^{25}\mathrm{Wcm}^{-2}$, because the first pair was assumed to be created by the counter-propagating laser beams *in vacuum*, and not in a tenuous plasma, as in our calculation.

In figure 5.2 we have plotted the points where the values $\eta = 0.1$ and $\eta = 1$ are first achieved during an electron's trajectory in a space-time (z-t) diagram of the interaction of the laser pulses. The plot was made for 1000 electrons with random initial conditions and intensities as described above. From this we can reach the conclusion that, since pair production happens where η approaches unity, then it is likely that pair production happens at the interaction region of the pulses, thus leading to cascades as described above.

5.2.1 Linear vs circular polarization

In order to further justify the choice of linear polarization, we have conducted the same calculation for two different configurations of circularly polarized beams.

The first corresponds to the configuration of Bell and Kirk [7], where the polarizations of the beams are of the opposite sense, so that nodes of the electric and magnetic field would occur in an infinitely long standing wave. The expressions for the circularly polarized beams were folded with the same envelope functions, of the same duration and cutoff as in the linearly polarized case, and again it was assumed that the transverse radius of the beam is equal to one wavelength. The result of this calculation can be seen in figure 5.7. It is obvious that pair

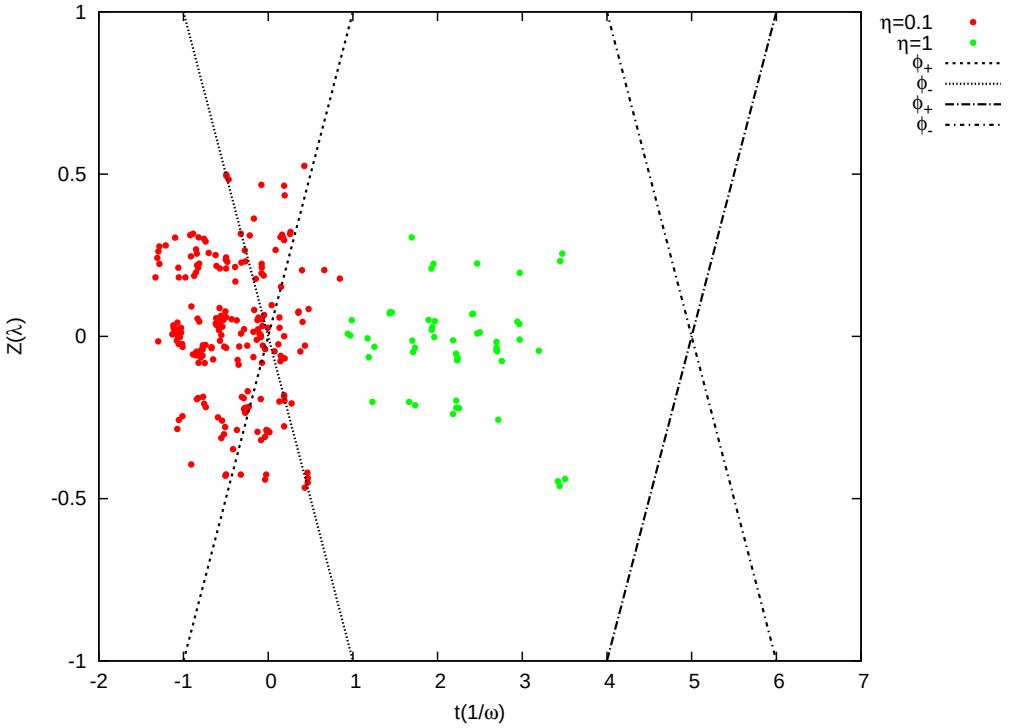

Figure 5.5: **Spacetime plot showing the points where $\eta = 0.1$ and $\eta = 1$ are achieved.** *The lines forming the "X"-shape at the left are the positions of the front edges of the pulses, while the corresponding lines to the right are the rear edges of the pulses. Trajectories have been calculated for 1000 particles, with random initial conditions and intensities as described in the text. Red dots signify the points where η exceeds 0.1 for the first time in a trajectory. This happens in most cases around the intersection of the front ends of the pulses. Green dots signify the points where $\eta = 1$ for the first time. It can be seen that the red points are more numerous, while the green ones are in the middle of the pulse intersection area. Thus pairs are likely to be produced at the beginning or during the interaction of the pulses, in a region of strong field, leading in the rapid acceleration of the secondary particles, and the development of a pair cascade.*

creation is suppressed. The overwhelming majority of trajectories give no pairs at all.

The second configuration we tried is the one of two counter-propagating, circularly polarized beams, with the same sense of polarization, so that there are no nodes in the wave resulting from their superposition. This wave can be seen in figure 5.2. Again the same envelope function was used and the same transverse dimension was assumed. The results of the computation for this case can be seen in figure 5.8. It is obvious that the absence of nodes is of advantage, however pair production is still suppressed by two orders of magnitudes in the high intensity edge, and by much more at lower intensities.

The reason for the higher pair production in the linearly polarized beams is the fundamental difference between particle trajectories in strong linearly polarized waves and in strong circularly polarized waves: in the center of momentum frame in the first instance the particles undergo an oscillation both in the transverse direction and in the direction of wave propagation. However in a strong circularly polarized wave the center of momentum motion is circular, transverse to the direction of propagation of the wave. In the linear polarized beams, then, the particle is

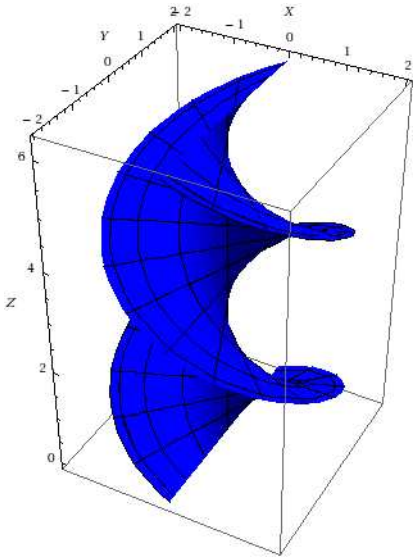

Figure 5.6: **Circular polarizations, no nodes.** *In the case where the two beams have the same sense of polarization, at every point in space the vector of the electric (magnetic) field has a fixed direction and oscillates between the values* $-2E_0$ *and* $2E_0$*, where* E_0 *is the field amplitude in the single beam. On the left the contour is shown which is created by the field vectors at* t_0*. The whole spiral structure is oscillating in a harmonic way, i.e. the field has always the same magnitude everywhere at a given point in time. This plot corresponds to infinitely long pulses. In our calculation the same envelope function was used as in the case of linear polarization.*

capable of excursions along the beams, which contribute substantially to its probing regions of intense field.

This can be readily seen in the figure 5.3, where we compare two trajectories that were calculated for identical beam intensities and initial conditions, in the case of linear aligned polarizations and in the case of circular polarizations of opposite handedness. The trajectory of the particle in the linearly polarized beam is more "angular", with more abrupt longitudinal excursions, and these correspond to increases in η. The trajectory of the particle in the circularly polarized beams, on the contrary, is much smoother, and the value of η remains one order of magnitude lower throughout the calculation.

5.3 Limitations according to our model - work for the future

We have conducted the above calculations using the assumption of continuous energy emission by the electrons, which is given by the formula of quantum synchrotron radiation. This way we have taken into account one of the effects that appear in the quantum mechanical regime, which is the reduction in total power of the emitted radiation, because of the cutoff at energy approaching the electron's own energy.

However, there is a second effect that we haven't included in this treatment: this is the episodic emission of photons. The stochastic nature of the photon emission leads to leaps in the electron energy, which have as a result the broadening of the electron spectrum, as predicted by Shen and White [81]. It has been recently shown using a Monte Carlo approach (Duclous et al. 2010, [19]) that this spread in energy, which is known as *straggling*, leads to increased pair production for given initial conditions and laser intensity in the case of circular polarizations with $B = 0$ nodes. This happens because straggling causes occasional excursions of the η parameter, which leads to increased energy of the emitted photons and as a result boosts pair production. Straggling also slows the convergence of the electrons towards the $E = 0$ nodes, making them stay for longer times in regions of stronger field where pair production can occur.

A full numerical treatment of the problem would involve larger scale simulations following the initiation of a cascade in the focus of the beams, possibly combining a Monte Carlo algorithm

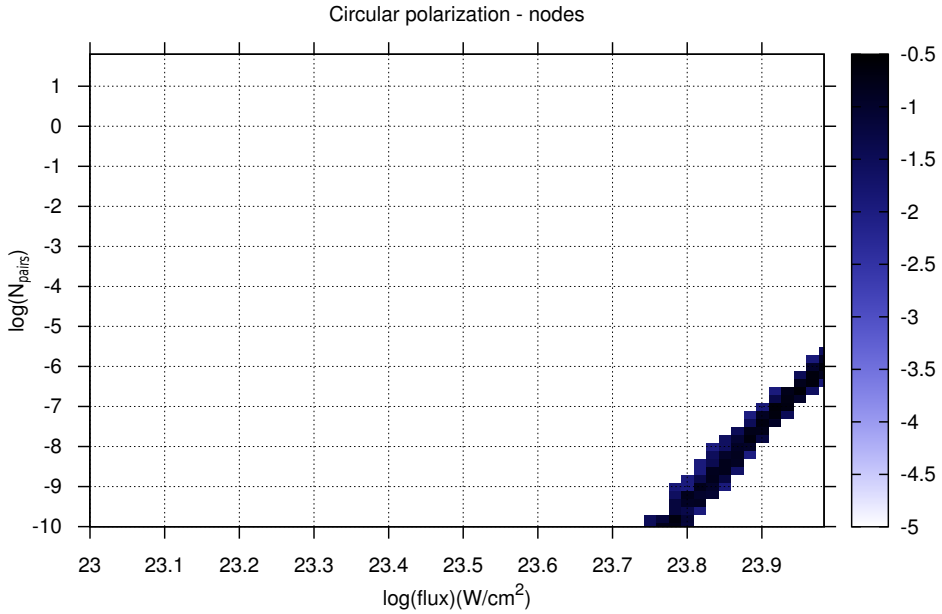

Figure 5.7: **Probability of pair production for circular polarization, for beams of opposite handedness.**

with a Particle In Cell (PIC) simulation. It remains to be seen if such a simulation will confirm our predictions, and if pair cascades are going to be observed in the next few years at the new ultra-high intensity laser facilities currently under construction.

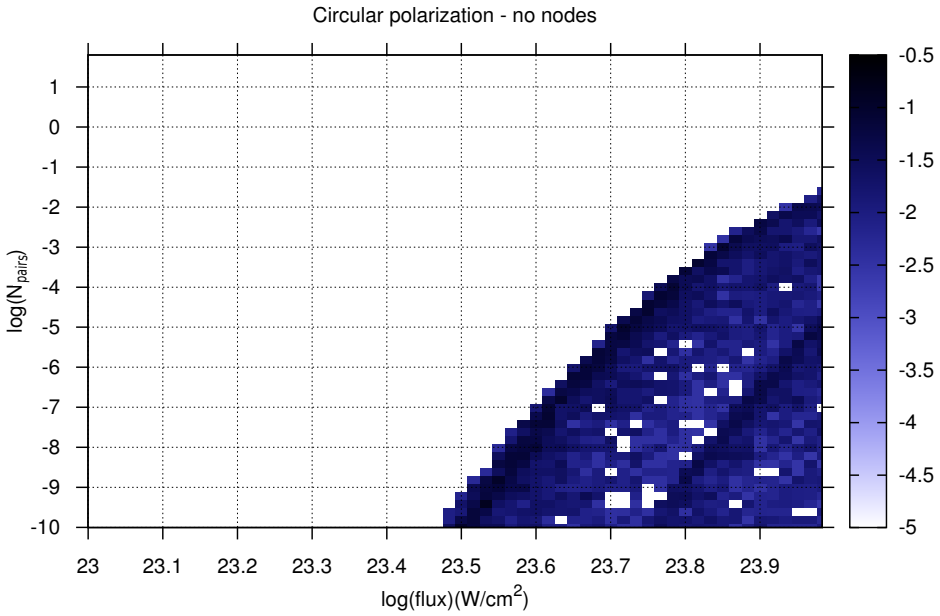

Figure 5.8: **Probability of pair production for circular polarization, for beams of the same handedness.**

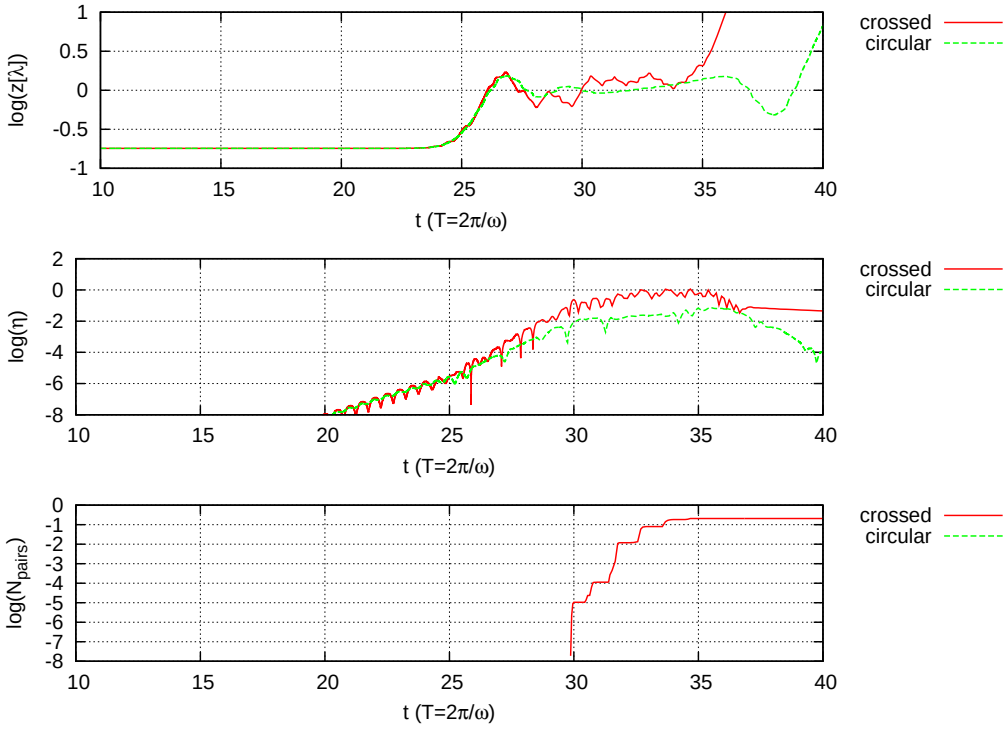

Figure 5.9: **Comparison of trajectories for linear and circular polarizations.** *Two trajectories with identical initial conditions, and identical single beam intensities are shown. For the linearly polarized case, the parameter η reaches the value $\eta = 1$ for parts of the trajectory, thereby giving a finite probability of pair creation. For the circular polarization case, η stays at least one order of magnitude lower. In the first panel the coordinate z along the beam direction is shown for the two trajectories. It can be seen that in the linear polarization case, the excursions in z are more prominent, and they are connected with increases in η.*

Part II

Non-linear waves in pulsar winds

Chapter 6

Pulsars and their winds

The most natural environment to study large-amplitude waves in astrophysics are pulsars, rapidly rotating neutron stars which have their rotational axis misaligned to the magnetic axis. From their serendipitous discovery more than forty years ago until today they have been the object of observation in all bands of the electromagnetic spectrum and the cause of many discoveries in astrophysics. The most famous of these objects, the Crab Pulsar, along with the nebula surrounding it, has been exhaustively studied, however has yet to reveal all its secrets, as we will discuss below.

6.1 Introduction

In 1967, a new kind of radio source was observed using a new large radio telescope at the Mullard Radio Astronomy Observatory. The discovery was announced in a 1968 Nature paper [37], where it was proposed that the extreme regularity of the pulses of the new source might be attributed to the radial pulsations of a white dwarf or a neutron star. Because of this regularity, the sources were named pulsars. In the same year it was argued that a rotational origin of the pulses is much more likely ([69],[25]). Very soon observations of pulsars in association with the Vela and Crab supernova remnants, as well as theoretical arguments, lead to an increasing acceptance of the idea that pulsars were to be identified with rotating magnetized neutron stars ([89],[49],[84]).

Ostriker and Gunn [72] subsequently showed that if the magnetic field of the pulsar is approximated as a dipole and the magnetic and rotational axes are misaligned, then the observed pulsar slowdown as expressed by the time derivative of the pulsar period $\dot{P}$, is consistent with the losses by magnetic dipole radiation. Furthermore, this luminosity was found to be of the same order of magnitude of the synchrotron luminosity in the nebula in the case of the Crab pulsar. Therefore the energy lost by the pulsar as measured by its rotational slowdown is transferred to the nebula by some kind of outflow. The model of the pulsar as a rotating neutron star with its magnetic moment at an angle to its rotational axes has since then prevailed.

The first ones to realize that pulsars would be the source of large amplitude electromagnetic waves were Gunn and Ostriker, who in a seminal paper [29] argued that rotating magnetized neutron stars in vacuum would emit electromagnetic waves of strength parameter $a \gg 1$ close to the star, and that particles could be accelerated by these waves to relativistic energies. However,

it was soon realized [26] that pulsars can never be in vacuum: because of the pulsar's rapid rotation an electric field parallel to the magnetic field close to the pulsar surface arises, which is strong enough to lift particles from the star's surface into its magnetosphere, filling it with charge. The number density of the charge carriers was calculated by the Goldreich and Julian [26] to be:

$$n_{GJ} = \frac{\mid \mathbf{\Omega} \cdot \mathbf{B} \mid}{2\pi ec} \tag{6.1}$$

where $\mathbf{\Omega}$ is the angular velocity expressing the star's rotation and $\mathbf{B}$ the magnetic field.

Furthermore, pair cascades on the strong magnetic field close to the pulsar were predicted (e.g.[13], [14],[77]), which would further contribute to the charge density surrounding the pulsar. These cascades develop within the pulsar's *light cylinder*, defined as the distance from the pulsar's equator, at which a corotating particle would reach the speed of light:

$$r_{\rm LC} = \frac{c}{\Omega} \tag{6.2}$$

where Ω is the pulsar's rotational frequency. The cascades are initiated by electrons accelerated along the curved magnetic field lines. These electrons emit high energy photons, which then can pair produce on the neighbouring field lines. This way the pulsar's magnetosphere was predicted to fill with an electron-positron plasma. Thus the need for a magneto-hydrodynamic approach of the pulsar system arose.

Rees and Gunn [75] gave a description of the generic pulsar outflow as a combination of a relativistic magnetized wind and a wave modulated at the pulsar's frequency. This outflow ends at the termination shock, where the ram pressure of the wind equals the pressure in the nebula. By this argument they estimated the location of the shock front in the Crab supernova remnant to be at about 1/10 the radius of the nebula, or about 3×10^{17}cm $\simeq 10^9 r_{\rm LC}$ from the pulsar. In their model, the pulsar's magnetic axis was not aligned with the rotational axis, so it is a rather general description of the outflow.

The first exact solution for a magneto-hydrodynamic wind arising from a rotating neutron star was calculated by Michel [60]. His solution was considering the simple configuration of an aligned rotator with a split monopole magnetic field. The two hemispheres of different polarity in the neutron star wind in this solution are separated by a current sheet at the equator. The existence of plasma in the star's atmosphere plays a crucial role in the field configuration in the wind. The plasma velocity cannot exceed that of light, so beyond the light cylinder the fluid cannot rigidly corotate with the pulsar. The inertia of the plasma, then, exerts a drag on the magnetic field lines beyond the light cylinder, causing them to bend backwards with respect to the rotation, giving rise to an azimuthal field component B_ϕ.

Much later, Bogovalov [10] generalized this result for a misaligned rotator, again for a split monopole configuration. Because of the misalignment of the axes, the equatorial current sheet gets warped, creating an outflow which is the relativistic analogue to the solar wind with its spiral structure. This pulsar wind is commonly referred to as the "striped wind" [17]. The azimuthal magnetic field component has a spiral form, as in the case of the aligned rotator, and in large distances dominates the field in the wind. The reason for this is magnetic flux conservation in the rotating split monopole model. For the radial field component, flux conservation dictates

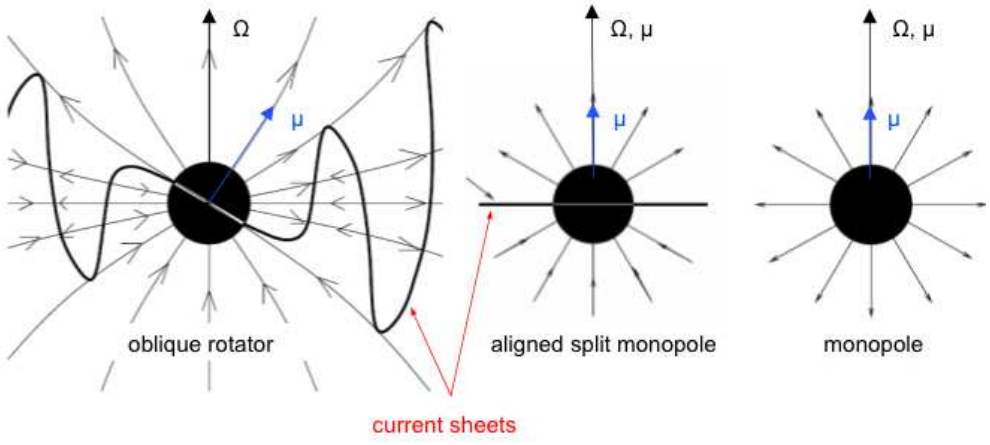

Figure 6.1: **Transition from the monopole solution to the striped wind.**
From right to left: the magnetic monopole, the split monopole solution with a current sheet at the equator, and the misaligned rotator with the warped current sheet, creating the striped wind.

that $B_r \propto \frac{1}{r^2}$, for an azimuthal field however $B_\phi \propto \frac{1}{r}$. The poloidal field in the wind $B_{\rm p}$, which is the combined radial and polar field is much smaller than the toroidal field at regions far from the light cylinder [6]:

$$B_{\rm p} \sim B_\phi \left(\frac{r_{\rm LC}}{r}\right)$$

Far away from the pulsar, then, the poloidal field is negligible in comparison to the azimuthal component. The warped current sheet is generally assumed to be very thin in comparison to the wind's wavelength, something that is supported by MHD simulations [83]. According to an argument put forward by Michel [62], the $\mathbf{J} \times \mathbf{B}$ force on the sheet particles tends to push the sheets to a thinner shape. As a result of this the magnetic field between the sheets tends to a constant value and the wave assumes the shape of a square wave rather than a sinusoidal one.

In the striped wind model, there is a region around the equator which contains magnetic field of alternating polarity, which is carried outwards with the wind as a wave. The opening angle of this region in latitude (measured from the equator) corresponds to the angle of misalignment of the rotational and magnetic axes of the pulsar. The wind, as a result, is not spherically symmetric, but propagates inside a finite solid angle around the equator, which we will denote Ω_w. Inside Ω_w there are stripes of alternating magnetic polarity (see figure 6.1), while outside the field has a constant sign. It is generally supposed that there are enough current carriers in the wind for this outflow to be described magneto-hydrodynamically as an entropy wave. In this case, a radial Lorentz boost with velocity equal to the phase velocity of this wave brings us to a frame of reference where the plasma is at rest. In this frame the electric field is zero, and the structure is one of a time-independent wave with no mean magnetic field value at the equator. This structure has been found to exist in force-free simulations of oblique rotators [83].

However, the point of view of the pulsar wind as an ideal magneto-hydrodynamic outflow has two significant drawbacks. The first of these was noted by Michel [61] and has to do with the current starvation of the outflow. This can be illustrated using Ampere's law in the pulsar

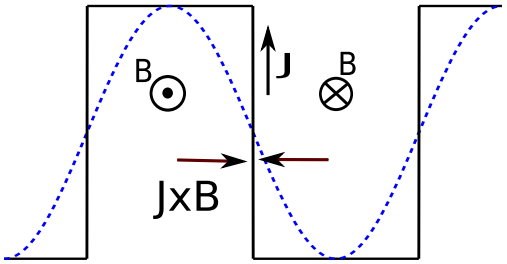

Figure 6.2: **The square wave form of the wave.**
The $\mathbf{J} \times \mathbf{B}$ *force on the particles of the current sheet push the wave into a square wave form. The magnetic field is essentially constant between current sheets.*

wind frame, where the striped pattern is stationary:

$$B' = \Delta' \frac{4\pi}{c} e N' v'_\theta \tag{6.3}$$

where primed quantities are measured in the wind frame, B' is the azimuthal field, N' is the particle number density, Δ' is the thickness of the current sheet and v'_θ is the three-velocity of the current sheet's particles, which is assumed to be purely in the polar direction. In the laboratory frame $N = \Gamma N'$, $B = \Gamma B'$ and $\Delta = \Delta'/\Gamma$ so the above equation translates to:

$$B_\phi = \frac{4\pi}{c} \Delta e N \Gamma v'_\theta \tag{6.4}$$

The current carriers density falls as the inverse square of the distance from the pulsar, while the field falls as $1/r$. Then for the above equation to hold in a wind of constant Γ, $v'_\theta \propto r$ has to apply. However, v'_θ is a three-velocity and is bounded upwards by the speed of light, so the above equation will cease to hold at a certain distance from the pulsar [62]. The two possibilities that arise in that case are that either Γ ceases to be constant, or the wave stops being stationary, and a displacement current term appears in Ampere's law.

The Lorentz factor of the flow can rise through reconnection of the magnetic field in the stripes, as shown in Lyubarsky and Kirk [53]. Another solution to the current starvation problem that involves the appearance of a strong displacement current term was presented in the form of large amplitude superluminal waves [2]. In contrast to the magnetohydrodynamical wind, these waves propagate only if the density of the outflow is *lower* than a certain value, a subject which we will return to in the following chapter. Melatos and Melrose [59] showed that at the distance from the pulsar where ideal magnetohydrodynamics breaks down, the displacement current takes over and the wind can be converted to a large amplitude transverse plasma wave propagating in the background relativistic outflow. This wave is linearly polarized close to the equator and circularly polarized close to the rotational poles. Kirk [43] investigated large amplitude, superluminal, circularly polarized waves and found two modes: a "free escape" mode,where the radial momentum of the particles tends to a constant at large radii and the wave propagates essentially as a vacuum wave in the background plasma, and a "confined" mode, where the particle radial momentum tends to zero at large radii and the wave retains the characteristics of a plasma wave.

The second problem that arises through the magnetohydrodynamical description of the pulsar wind, as noted by Kennel and Coroniti [40], is that in an ultra-relativistic, radial magnetohydrodynamic wind, Poynting flux cannot efficiently be converted to particle kinetic flux ([8],

[9]). However, observations of the nebula show that the conversion must indeed take place at some point between the light cylinder and the termination shock.

In order to address this problem, Coroniti [17] proposed reconnection at the current sheets of the striped wind as a possible mechanism for the dissipation of the magnetic flux in the stripes, and found that dissipation occurs rapidly without the acceleration of the flow, so that the Crab's stripes don't survive as far as its termination shock. However Lyubarsky and Kirk [53] in a more detailed discussion showed that the wind accelerates during reconnection, thus dilating the reconnection timescale and slowing down the process significantly. Kirk and Skjæraasen [46] investigated several dissipation processes and found that dissipation depends on the injection rate of pairs to the wind, so that it is still possible for the Crab's wind to dissipate before it reaches its termination shock, though one would have to assume a fast dissipation timescale and a high injection rate. It is interesting that in the superluminal modes discussed by Melatos and Melrose [59] or Kirk [43] the ratio of Poynting to kinetic energy flux either stays constant or rises, rather than diminishes.

What happens at the interaction of the wind with the termination shock is far from clear. If the dissipation of the field in the stripes wind is incomplete, then the outflow could arrive at the pulsar's termination shock accelerated to a high bulk Lorentz factor and still highly magnetized. In this case the dissipation of the magnetic field, along with particle acceleration has to happen at the shock, as proposed by Lyubarsky [56]. Pétri and Lyubarsky [73] have investigated this process, both analytically and through particle-in-cell simulation, and found a condition under which full dissipation of the stripes happens at the shock. We will return to this issue in a following chapter.

If the stripes are completely dissipated by reconnection in the wind, then the outflow ends in a weakly magnetized shock. There is no alternating field, and no wave component present in the wind anymore. Then the shock can be described as an ideal magneto-hydrodynamic shock [40], an infinitely thin discontinuity in the flow. If not enough particles are injected into the wind, so that the dissipation process cannot continue all the way up to the termination shock, then one returns to the problem of current starvation, and the possible conversion of the flow to a different mode, where the displacement current dominates the conduction current. However, in the following we will argue that the physical picture of the ideal MHD shock in a wind that carries an alternating field is oversimplified. When an electromagnetic wave of any kind interacts with a discontinuity, there should be some reflection of Poynting flux back to the upstream medium. We will show there are indeed large amplitude superluminal wave modes that can propagate in the upstream of a pulsar wind termination shock. These modes are linearly polarized, with a mean field equal to zero at the equator, but rising towards the edges of the alternating field zone. In the following, we will investigate the way these waves arise, their properties and their relevance in addressing the problems described above.

6.2 Plane wave approximation

The pulsar wind can contain either a subluminal magneto-hydrodynamic wave, or a superluminal plasma wave. Whichever is the case, the timescale of the variation τ is imposed by the rotator, $\tau \sim 1/\Omega$, and is associated with the length scale r_{LC}, the light cylinder radius. Far away from

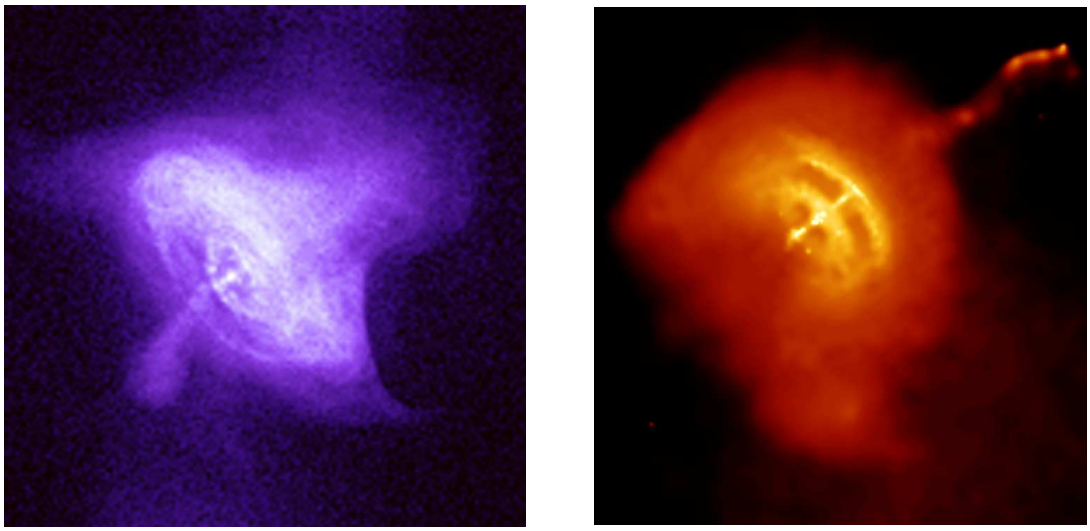

Figure 6.3: **X-ray images from the Crab and Vela pulsar wind nebulae.**
The X-ray images of the Crab and Vela nebulae, as seen by the Chandra X-ray observatory. The toroidal geometry is obvious in both images. A dark region inside the Crab nebula is assumed to contain the pulsar wind.

the light cylinder, where $r \gg r_{\rm LC}$, any length scale one could associate with the wave would be much smaller than the radius. Also, the curvature of the wavefront at large distances from the pulsar is of the order of magnitude of the inverse radius, and it is very low. For these reasons a plane wave approximation of the wave at any given radius is enough to convey the characteristics of the outflow, so long as we are far from the light cylinder.

We introduce a dimensionless radius variable, which is normalized to the light cylinder radius:

$$\varrho = \frac{r}{r_{\rm LC}} \tag{6.5}$$

When $\varrho \gg 1$ we are at the zone where curvature effects can be ignored, and our plane wave approximation is valid.

We will identify the radial direction with the $x-$direction of a cartesian system of coordinates. The wind propagates then in the positive $x-$direction. In the striped wind, the azimuthal magnetic field is represented by B_z and the electric field which is perpendicular to both the propagation direction and the magnetic field is in the $y-$direction and symbolized by E_y. The field in one stripe is in good approximation constant: the change of the field in one stripe is of the order of magnitude $\sim 1/\varrho^2 \ll 1$. For this reason, far from the light cylinder we can consider the wave to be a plane square wave of constant amplitude even for regions which are significantly larger than one wavelength, but still shorter than $\sim \varrho$.

6.3 Constants of the flow

The properties of a steady state, radial wind which can be described as a subluminal or superluminal wave depend on four quantities: the phase-averaged particle flux $\langle J \rangle$, the phase averaged radial energy flux, which we denote by $\langle F \rangle$, the phase averaged radial momentum flux $\langle K \rangle$, and

a fourth parameter $\langle H \rangle$ which we will set to be proportional to the square of the phase-averaged electric field. Taking the phase average of Faraday's law,

$$\nabla \times \mathbf{E} = -\frac{\partial \mathbf{B}}{\partial t}$$

we find that the mean electric field $E_y = E$ for the transverse waves we have already mentioned, is proportional to the inverse square of the radius, i.e. $E \propto 1/r$, and consequently $B_\phi \propto 1/r$, i.e. the conservation of magnetic flux in an outflow with azimuthal field.

The quantity $\langle F \rangle$ is the component T^{01} of the stress-energy tensor of the outflow, which is the sum of the stress-energy tensors of the particles and the electromagnetic field. $\langle K \rangle$ is the component T^{11} of the stress-energy tensor. The general expressions for these quantities for a cold plasma ($p = 0$) take the following form:

$$\langle J \rangle = \langle n u_x \rangle c \tag{6.6}$$

$$\langle F \rangle = \langle n \gamma u_x \rangle m c^3 + c \frac{\langle (\mathbf{E} \times \mathbf{B})_x \rangle}{4\pi} \tag{6.7}$$

$$\langle K \rangle = \langle n u_x^2 \rangle m c^2 + \frac{\langle E^2 + B^2 \rangle}{8\pi} \tag{6.8}$$

$$\langle H \rangle = \frac{\langle E \rangle^2}{8\pi} \tag{6.9}$$

All four of these quantities depend on the distance from the pulsar as $\propto r^{-2}$. It is therefore, more convenient to use dimensionless parameters which are generated by the above fluxes. These are

$$\mu = \frac{\langle F \rangle}{m c^2 \langle J \rangle} \tag{6.10}$$

$$\nu = \frac{\langle K \rangle}{m c \langle J \rangle} \tag{6.11}$$

$$\eta = \frac{\langle H \rangle}{m c^2 \langle J \rangle} \tag{6.12}$$

These are independent of radius and are conserved in a striped pulsar wind [43]. The wave properties depend on these ratios and not on the specific values of $\langle J \rangle$,$\langle F \rangle$,$\langle K \rangle$ and $\langle H \rangle$. This is because the wave properties depend only on the ratio ω/ω_p, with ω the wave frequency and ω_p the plasma frequency in the wind: μ, ν and η depend on this ratio, while $\langle J \rangle$,$\langle F \rangle$,$\langle K \rangle$ and $\langle H \rangle$ depend on the frequency of the wave.

Once we have determined these ratios for the wave, we can fix the wave frequency using the luminosity of the pulsar $\mathcal{L}$ and the distance from it, assuming as we have already mentioned that the largest part of the energy emitted by the pulsar is transferred by the wind and ends up in the nebula:

$$\langle F \rangle = \frac{\mathcal{L}}{\Omega_w r^2} \tag{6.13}$$

Alternatively, if we impose a wave frequency, we can calculate the radius at which the wave can exist. In the pulsar system the rotation is imposed by the star, so the wave oscillates with frequency equal to that of the pulsar. Equation 6.13 states that the luminosity of the pulsar is evenly distributed in an outflow that expands in a solid angle Ω_w.

In the following chapters we will derive the expressions for $\langle J\rangle$,$\langle F\rangle$,$\langle K\rangle$ and $\langle H\rangle$ for the cases of the striped wind and the superluminal large-amplitude wave. Using equation 6.13 we will be able to connect a plane-wave solution of given energy flux $\langle F\rangle$ to a point in the wind, in order to find the range of radii within which waves of a given kind can propagate.

Chapter 7

The striped wind and the termination shock

The striped wind is a subluminal wave: a transformation with velocity $\beta_{\rm MHD} = v_{\rm MHD}/c$ in the radial direction brings us to a frame of reference where the wave is at rest. We will refer to this frame as the "wind frame" and denote it with S'. All primed quantities are in the wind frame and unprimed ones are in the laboratory frame, which is set to coincide with the frame where both the pulsar and the termination shock is at rest. In reality, the termination shock recedes from the pulsar, but it does so at velocities much smaller than the ultra-relativistic velocity of the wind. The coincidence of the two frames, therefore, is a satisfactory approximation.

7.1 The striped wind: an entropy wave

General properties

In the simplest incarnation of the striped wind model, the outflow consists of two species of particles, electrons and positrons. The particles are cold everywhere in the wind, apart from the current sheets separating regions of alternating magnetic field polarity. The magnetic pressure in the cold part of the stripes is balanced by the thermal pressure of the particles in the current sheets, where it is assumed that the field falls to zero. The current sheets are also assumed to be very thin in comparison to the wind's wavelength, so that the shape of the wave is approximated by a square wave, as explained in the previous chapter.

The wind is launched close to the light cylinder with a frequency Ω that is imposed by the pulsar's rotation. Far from the light cylinder the magnetic field amplitude can be approximated by the azimuthal component, and is given by

$$B(\varrho) = \frac{B_L}{\varrho} \tag{7.1}$$

where B_L is an appropriate toroidal magnetic field value at the light cylinder.

The strength parameter of the striped wind can be defined as the strength parameter of a vacuum wave carrying the same energy flux and of the same frequency as the striped wind. The striped wind is a linearly polarized wave, so the corresponding vacuum wave would be

linearly polarized and the strength parameter would be defined using the root mean square of this linearly polarized wave. The wind has a square wave form, so the root mean square field is equal to the amplitude and the strength parameter is:

$$a(\varrho) = \frac{eB(\varrho)}{mc\Omega} = \frac{a_L}{\varrho} \tag{7.2}$$

where a_L is the value of the strength parameter that corresponds to B_L:

$$a_L = \frac{eB_L}{mc\Omega}$$

In the wind frame there is no electric field present, while in the laboratory frame there is an electric field component given by the force-free MHD condition, which dictates that the plasma has an infinite conductivity and all non- electromagnetic forces are negligible:

$$\mathbf{E} = -\overrightarrow{\beta}_{\rm MHD} \times \mathbf{B} \tag{7.3}$$

where $\beta_{\rm MHD} \simeq 1$ for an ultrarelativistic wind. The Lorentz factor corresponding to $\beta_{\rm MHD}$ is the bulk Lorentz factor of the outflow and is denoted by Γ:

$$\Gamma = \frac{1}{\sqrt{1-\beta_{\rm MHD}^2}} \tag{7.4}$$

Since in the plane wave approximation $\mathbf{E} = E\hat{y}$ and $\mathbf{B} = B\hat{z}$, $E = \beta_{\rm MHD}B$ and for an ultrarelativistic wind the electric field in the laboratory frame is only slightly smaller than the magnetic field. The cold plasma is moving radially outwards with a velocity corresponding to $\beta_{\rm MHD}$. In the plane wave approximation, the particle flux, energy flux density and momentum flux density are:

$$\langle J \rangle = 2N\beta_{\rm MHD}\Gamma c \tag{7.5}$$

$$\langle F \rangle = 2Nmc^3\beta_{\rm MHD}\Gamma^2 + c\beta_{\rm MHD}\frac{B^2}{4\pi} \tag{7.6}$$

$$\langle K \rangle = 2Nmc^2\beta_{\rm MHD}^2\Gamma^2 + (1+\beta_{\rm MHD}^2)\frac{B^2}{8\pi} \tag{7.7}$$

In the derivation of the above expressions we have ignored the contribution of the hot current sheets which is negligible if their width is much smaller than the wavelength of the striped wind, which is $\lambda \simeq r_{\rm LC}$. We have, therefore, a cold wind with a proper particle density N for each species. The fourth conserved quantity, $\langle H \rangle$, depends on the latitude in the wind and can be expressed as

$$\langle H \rangle = \frac{\theta^2\beta_{\rm MHD}^2 B^2}{8\pi} \tag{7.8}$$

where θ is a parameter that measures the ratio of the mean magnetic field in the stripes to the field amplitude:

$$\theta = \frac{|\,\langle B \rangle\,|}{\sqrt{\langle B^2 \rangle}} \tag{7.9}$$

At the equator, $\theta = 0$, and the magnitude of θ rises as one moves away from the equator,

becoming $\theta = 1$ at the edge of the wind zone. At this point there is no wave anymore, but rather an outflow with a constant field.

The quantities μ, ν, η are, then

$$\mu = \Gamma(1+\sigma) \tag{7.10}$$

$$\nu = \frac{\Gamma^2(1+\sigma) - (1+\sigma/2)}{\sqrt{\Gamma^2-1}} \tag{7.11}$$

$$\eta = \frac{\Gamma\beta_{\rm MHD}\theta^2\sigma}{2} \tag{7.12}$$

where σ is the *magnetization parameter*

$$\sigma = \frac{B^2}{8\pi N\Gamma^2 mc^2} \tag{7.13}$$

which is the ratio of the Poynting flux to the particle energy flux. The magnetization parameter was introduced by Kennel and Coroniti [39] in the context of the striped wind, and remains constant in the flow, just like the bulk Lorentz factor Γ, if we ignore dissipation effects in the current sheets. Another property of σ is that it is a Lorentz invariant parameter of the striped wind.

Pulsar winds are Poynting-flux dominated and ultrarelativistic, with magnetization parameters and Lorentz factors much larger than unity. As discussed in Chapter 6, it is difficult to convert the Poynting flux to kinetic energy flux, even if dissipation processes in the current sheets are considered. It is therefore likely that σ and Γ remain large all the way out to the termination shock of the wind. This causes a near-degeneration of μ and ν, because $\sqrt{\Gamma^2-1} \approx \Gamma$ and

$$\nu \approx \Gamma(1+\sigma) - \frac{1+\sigma/2}{\Gamma} \approx \mu$$

Validity of the cold outflow approximation

The approximation of the infinitely thin current sheets can be expressed as a requirement that the width of the current sheets is negligible in comparison to the wind's half-wavelength. The minimum width of a current sheet is dictated by the gyration radius r_g of the sheet particles in the field of the square wave.

The particles in the current sheets are hot: if one assumes that the magnetic field is zero in the current sheet and rises to its constant value outside of it, in the cold part of the outflow, then there has to be pressure balance between the hot and cold parts of the outflow. Defining the average Lorentz factor of the thermal motion of the current sheet particles, $\langle\gamma_{\rm th}\rangle$, then pressure balance can be expressed (in the wind frame, where the wave is stationary) as:

$$\langle\gamma_{\rm th}\rangle mc^2 = k_B T = \frac{B'^2}{8\pi 2N'} \tag{7.14}$$

where k_B is the Boltzmann constant, T is the temperature in the current sheets and the particle density is $2N'$, with N' being the density of each of the two species in the outflow. N' is considered for simplicity to be equal in the hot and cold parts of the outflow.

The criterion that has to be satisfied, then, is that r_g has to be much smaller than the wave's

half wavelength. In the wind frame this inequality can be written as:

$$r_g = \frac{\langle \gamma_{\rm th} \rangle mc^2}{eB'} \ll \lambda' \tag{7.15}$$

where γ is the mean Lorentz factor of the thermal motion in the hot current sheets.

Combining 7.15 and 7.14 and taking into account the Lorentz invariance of the magnetization parameter we arrive at the condition

$$\sigma \ll a \tag{7.16}$$

where a is the strength parameter. This condition will almost certainly hold in the inner parts of a pulsar outflow, close to the light cylinder. For the example of the Crab pulsar the strength parameter at the light cylinder is of the order of magnitude $a_L \sim 10^{11}$. Since the strength parameter falls with distance from the pulsar, as the distance $\varrho = a_L/\sigma$ is approached the above condition ceases to hold. Whether this happens before the wind reaches the termination shock or not depends on the individual object we are considering, and from the dissipation processes in the striped wind. For young pulsars with high magnetic fields and low periods or for pulsars in binaries, where the separation between the stars limits the extent of the wind, the above condition is likely to hold. For the Crab pulsar, the termination shock is at a distance of $\varrho \sim 10^9$ from the pulsar, and the strength parameter is of the order of magnitude $a \simeq 10^2$ at this distance. Another example is the pulsar PSR B1259-69 which is a member of a binary system with a blue B2e star. The distance of the two stars varies between $\varrho \sim 10^4$ and $\varrho \sim 10^7$ between periastron and apastron, which means that the pulsar wind collides with the stellar outflow while its strength parameter is still many orders of magnitude greater than unity.

7.2 The termination shock

The pulsar wind is thought to terminate in a shock, where the wind's ram pressure balances the pressure of the surrounding nebula [75]. This shock is usually modeled as an infinitely thin discontinuity. Because the field of the outflow is very nearly toroidal, the shock is perpendicular, which means that the magnetic field is perpendicular to the shock normal. Shocks are classified as weak or strong, according to whether they convert a small or large amount of the energy of the upstream flow to thermal energy in the downstream.

Kennel and Coroniti [39] noted that, although the pulsar's wind is highly magnetized, with $\sigma \gg 1$, observations show that in the nebular flow the magnetization parameter is very low, $\sigma \sim 10^{-3}$. They then investigated whether this jump in the magnetization parameter can be explained using the MHD jump conditions of the shock. These connect the physical quantities that characterize the flow upstream with the ones downstream, and are derived demanding the conservation of particle, energy, momentum and magnetic fluxes in the transition from the upstream to the downstream, without looking into the microphysics of the shock itself. The result was that a large-σ shock is effectively weak. The flow remains relativistic downstream and the magnetic field value remains almost unchanged. This can be quantified by the *compression ratio* of the shock:

$$\rho = \frac{B_2}{B_1} = \frac{v_1}{v_2} = \frac{N_2}{N_1} \tag{7.17}$$

where B_1 and B_2 is the constant magnetic field upstream and downstream, respectively, v_1,v_2 are the respective magnitudes of the three-velocity of the flow and N_1,N_2 the particle number densities. All the quantities refer to the shock frame. For an upstream flow of high magnetization σ, the compression ratio can be expressed as

$$\rho \simeq 1 + \frac{1}{2\sigma} \tag{7.18}$$

What this means is that a highly magnetized flow is going to remain highly magnetized after passing through a perpendicular MHD shock. This is the basis of the $\sigma-$problem, which was introduced in the previous chapter. Assuming, then, that the dissipation in the striped wind is not enough to reduce the magnetization of the outflow, (see [46]), then the pulsar wind termination shock might be expected to be a weak perpendicular shock.

Along the shock front there is a current sheet, which is assumed to be infinitely thin. This sheet supports the jump in the magnetic field between the downstream and the upstream. The application of the jump conditions for a perpendicular MHD shock to the termination shock of a striped pulsar wind has an implicit assumption: that the jump conditions hold between field reversals, and that during a reversal the current direction along the discontinuity changes instantaneously. "Instantaneously" in this context means that the timescale of the current response to a field reversal is much shorter than the timescale of the field reversal itself. If we consider the first to be the gyration period of particles in the magnetic field of the outflow and the second to be the inverse of the wind's frequency, then this condition brings us to the strong wave limit:

$$a \gg 1$$

If the striped wind is a strong wave, and under the assumption that during the "instantaneous" current reversal only a negligible amount of radiation is emitted, then its termination shock can be considered in a steady state between field reversals.

7.3 Wind-shock interaction

The pulsar wind's termination shock is a discontinuity, which carries an alternating current, as we just argued. In the first approximation, the waveform follows the temporal variation of the magnetic field as the stripes sweep the shock. Close to the termination shock, at the equator, the fields are:

$$\mathbf{B} = \hat{z} B_s \mathrm{sq}\left(x/\beta_{\mathrm{MHD}} - t\right) \tag{7.19}$$

$$\mathbf{E} = -\beta_{\mathrm{MHD}} \hat{x} \times \mathbf{B} \tag{7.20}$$

where B_s is the magnetic field amplitude close to the termination shock and $\mathrm{sq}(x)$ is the square wave given by

$$\mathrm{sq}(x) = 2 \sum_{n=-\infty}^{+\infty} \left(\mathrm{H}\left(x - 2\pi n\right) - \mathrm{H}\left(x - 2\pi n - \pi\right) - \frac{1}{2} \right) \tag{7.21}$$

where $\mathrm{H}(x)$ is the Heaviside step function:

$$\mathrm{H}(x) = 1, x > 0 \tag{7.22}$$

$$\mathrm{H}(x) = 0, x < 0 \tag{7.23}$$

Here time is normalized to the inverse of the angular frequency $1/\Omega$ and length to c/Ω, so we have dimensionless time and length parameters. An expression for the square wave which will be useful later is

$$\mathrm{sq}(x) = \frac{4}{\pi}\sum_{n=1}^{\infty}\frac{\sin((2n-1)x)}{(2n-1)} \tag{7.24}$$

Thus the current is implied by 7.19 and 7.20:

$$\mathbf{J}(\mathbf{r},t) = \hat{y}\delta(x-x_s)J_0\mathrm{sq}\left(\frac{x_s}{\beta_{\mathrm{MHD}}} - t\right) = -\hat{y}\delta(x)J_0\mathrm{sq}\,(t) \tag{7.25}$$

where the shock's location is set to $x_s = 0$ and

$$J_0 = \frac{(\rho-1)B_s}{4\pi}$$

with B_s the magnetic field amplitude of the wind at the termination shock.

Wave emission by an alternating current

In vacuum, an alternating current like the one flowing along the shock discontinuity would be the source of an electromagnetic vacuum wave. It is instructive to calculate the vector potential of the radiation emitted by the alternating current. Its components are given by the integral [48]:

$$\mathbf{A}_\omega(\mathbf{r}) = \int_V \mathbf{J}_\omega(\mathbf{r}')\frac{e^{ik|\mathbf{r}-\mathbf{r}'|}}{c\mid \mathbf{r}-\mathbf{r}'\mid}d^3\mathbf{r}' \tag{7.26}$$

where the integration is over all space and $\mathbf{J}_\omega$ is the Fourier transform of the current:

$$\mathbf{J}_\omega = \int_0^{2\pi/\Omega}\mathbf{J}(t)\exp^{-i\omega t}\,dt$$

After calculating $\mathbf{A}_\omega$ from 7.26, the vector potential $\mathbf{A}$ is found using the inverse Fourier transform. In order to arrive at the formula for $\mathbf{A}_\omega$ we need the following integral (from 7.26):

$$I = \int_V \delta(x')\frac{e^{ik|\mathbf{r}-\mathbf{r}'|}}{c\mid \mathbf{r}-\mathbf{r}'\mid}d^3\mathbf{r}' \tag{7.27}$$

and after the x' integration

$$I = \int_{-\infty}^{+\infty}\int_{-\infty}^{+\infty}\frac{e^{ik\sqrt{(z-z')^2+(y-y')^2+x^2}}}{c\sqrt{(z-z')^2+(y-y')^2+x^2}}dz'dy' \tag{7.28}$$

The form of the integral is simplified if we use cylindrical coordinates in the $y-z$ plane:

$$y' - y = \rho\cos\theta \tag{7.29}$$

$$z' - z = \rho\sin\theta \tag{7.30}$$

$$dx'dz' = \rho d\rho d\theta \tag{7.31}$$

so I becomes

$$I = \int_0^\infty \rho d\rho \int_0^{2\pi} d\theta \frac{e^{ik\sqrt{\rho^2+x^2}}}{\sqrt{\rho^2+x^2}}$$

A new substitution $R = \sqrt{\rho^2+x^2}$ from which we get

$$dR = \frac{\rho}{\sqrt{\rho^2+x^2}} d\rho$$

brings the integral to the simplified form

$$I = 2\pi \int_{|x|}^\infty dR e^{ikR}$$

the result of which is"

$$I = \frac{2\pi i}{k} e^{ik|x|} \tag{7.32}$$

The upper limit, which is infinity, was neglected on the physical grounds that physical quantities of the problem cannot depend on effects at infinity [79].

We are interested in the upstream area, where $x < 0$. In that area the waves emitted by the shock front propagate in the negative x-direction. Restoring dimensions, the vector potential is given by:

$$\mathbf{A}(\mathbf{r},t) = \hat{y} J_0 \frac{4}{\pi} \sum_{n=1}^{\infty} \frac{\cos(k_n(x+ct))}{\omega_n/\Omega} \frac{\pi}{ck_n}$$

where $\omega_n/\Omega = 2n-1$ and $\omega_n = k_n c$.

From the above result we can calculate the reflected fields. Because of equation 7.24 the derivative of the above series with respect to t or z gives a square wave form again. Returning to the dimensionless time and space variables the reflected fields are given by:

$$\mathbf{B}_\mathrm{r}(z,t) = \hat{x} B_0 \mathrm{sq}(z+t) \tag{7.33}$$

$$\mathbf{E}_\mathrm{r}(z,t) = \hat{z} \times \mathbf{B}_\mathrm{r} \tag{7.34}$$

where

$$B_0 = \frac{(\rho-1)B_s}{4}$$

The fields referring to the reflected component as it is calculated for propagation is vacuum are explicitly marked with the subscript r. It is straightforward to show by Fourier decomposition that for any incoming wave the corresponding reflected one is going to have the same shape and frequency but an amplitude diminished by $(\rho-1)/4$.

If full dissipation of the alternating field in the stripes happens at the shock, as proposed by Lyubarsky, [56], then there's no large scale magnetic field in the downstream. The amplitude of the waves in this case would then be:

$$B_0 = -\frac{B_s}{4} \tag{7.35}$$

The strength parameter of the reflected wave would be, in the absence of dissipation:

$$a_r = \frac{\rho - 1}{4} a \tag{7.36}$$

7.3.1 Linear and non-linear waves in a plasma

The alternating current along the termination shock would be the source of a wave in vacuum, that has the same shape and frequency as the striped wind incident on the shock. The wave, however, is not emitted in vacuum, but into a plasma which carries a magnetic field. Moreover this wave can be a strong wave if the compression ratio is not too close to unity: for $\rho \gtrsim 1 + 4/a$ the strength parameter of the reflected wave will be greater than unity. However, if we replace for ρ in this inequality from the relation 7.18 we see that the reflected wave is going to be strong if

$$\sigma \lesssim a \tag{7.37}$$

which is guaranteed to hold in a striped wind because of the condition 7.16.

Moving now to the wind frame S', a criterion is needed for the propagation of a strong wave in a magnetized plasma. In S' each stripe is longer by Γ^2 than the laboratory wavelength, and holds a constant magnetic field that corresponds to the field of the stripe in the laboratory frame. It can be then considered as a uniform medium with a background field where the propagation of a non-linear wave is investigated. This wave is going to propagate transversely to the background field and is a transverse wave by the mechanism of its emission.

In the linear (low amplitude) limit, the cutoffs for the propagation of electromagnetic waves in plasma have been extensively studied and can be found in standard textbooks (see, for example, [22]). An electromagnetic wave can propagate in a cold unmagnetized plasma only if its frequency is higher than the plasma frequency: $\omega > \omega_p$. ω_p depends on the particle density n, in our case the density of electrons and positrons:

$$\omega_p = \sqrt{\frac{4\pi n e^2}{m}}$$

It has been shown that this cutoff is lower for strong waves (an explanation can be found in [58]). In that case the condition for propagation becomes

$$\omega > \frac{\omega_p}{\sqrt{a}}$$

with $a > 1$ the strength parameter of the wave.

If the wave propagates in a background magnetic field, then the cutoff depends on whether it propagates along or perpendicularly to the field lines. In the first case the mode is called the ordinary mode or O-mode, while in the second case it is referred to as the extraordinary mode or X-mode. The cutoffs for these waves in the case of electron-ion plasmas are well known [22].

For the case of electron-positron plasmas, the cutoff for the linear X-mode is [38]:

$$\omega > \sqrt{\Omega_c^2 + \omega_p^2} \tag{7.38}$$

where

$$\Omega_c = \frac{eB}{mc}$$

is the cyclotron frequency in the background field with B the magnetic field amplitude. In en electron-ion plasma, the X-mode is a hybrid wave, which means that it is neither purely longitudinal nor purely transverse. This is however not true for the same mode in an electron-positron plasma: in this case it is a purely transverse wave [38], like the non-linear mode we are investigating. This is why we will identify the reflected wave with the non-linear X-mode and investigate its propagation upstream.

Cutoff of the non-linear X-mode

Kennel and Pellat [41] have calculated the dispersion relation for the non-linear extraordinary mode in the limit of massless particles. This limit applies to the case where the wave is strong enough to make the particles ultrarelativistic, so their energy is much larger than their rest mass energy. Their results can be applied to an electron-positron plasma. The cutoff frequency for the non-linear X-mode can be calculated from the dispersion equation in the limit where the phase velocity tends to infinity, $\beta_\phi \to \infty$, and it is given in the wind frame S' as [41]:

$$\omega' = \frac{\Omega_c'}{2a_r} + \frac{1}{2}\sqrt{\left(\frac{\Omega_c'}{a_r}\right)^2 + \frac{\omega_p'^2}{a_r}} \tag{7.39}$$

where $\Omega_c' = eB'/mc$ and B' is the constant field of the stripe in the outflow frame, taken as the background field. If

$$\Omega_r' > \omega' \tag{7.40}$$

where the frequency Ω_r' refers to the reflected component in S', the wave propagates in the upstream. However, the condition 7.16 is equivalent to:

$$\Omega_c' \ll \sqrt{a_r}\omega_p'$$

which means that in 7.39 the cyclotron frequency can be ignored. So the condition for the propagation of a large amplitude wave in the upstream is reduced to the one for propagation in an unmagnetized plasma already mentioned in the previous paragraph [58]:

$$\Omega_r' > \frac{\omega_p'}{\sqrt{a_r}} \tag{7.41}$$

Taking into account that $B = \Gamma B'$, $n = \Gamma n'$ and $\Omega = \Omega'/\Gamma$, where n is the laboratory frame density, the above condition transforms into

$$\Gamma^4 > \frac{a_\mathrm{r}}{\sigma} \tag{7.42}$$

7.4 Dissipation at the shock front

Full dissipation

The calculations of the reflected wave have been performed assuming that the field downstream is just the compressed upstream field. Lyubarsky [56] however, has proposed that the magnetic field might dissipate at the shock front via reconnection caused by the compression of the upstream flow as it enters the shock. Pétri and Lyubarsky [73] subsequently showed that the alternating magnetic field dissipates completely at the strong shock front if the condition

$$\Gamma \geq \frac{a}{\sigma} \tag{7.43}$$

holds. For full dissipation of the stripes the downstream large-scale field vanishes. The amplitude of the reflected wave, then, is one fourth the amplitude of the field in the wind just before the shock:

$$a_r = \frac{a}{4}$$

The condition 7.42 for propagation in the upstream becomes then:

$$\Gamma^4 > \frac{a}{4\sigma} \tag{7.44}$$

Comparing 7.43 and 7.44, we see that 7.44 always holds when 7.43 holds.

The first conclusion we can reach, therefore, is that when full dissipation occurs at the shock, a strong wave is emitted and propagates upstream. This wave carries a Poynting flux with is a fraction of $\sim 1/16$ of that carried in the striped wind. If $a \gg 1$ then $a_r \gg 1$ too, so the reflected wave is also strong. A strong wave with a large Poynting flux is likely to have a significant effect on the upstream flow, possibly imparting energy to the cold wind particles and leading to the formation of a precursor. In that case the jump conditions for the ideal MHD shock are not valid anymore, and an inconsistency arises: the description of the shock as a sharp discontinuity obeying MHD jump conditions has as a result the prediction of a reflected wave, which will create a precursor, thus rendering the approximation of the MHD shock insufficient.

Partial dissipation

Pétri and Lyubarsky have also found a condition under which partial dissipation of the upstream field occurs at the shock. This is

$$\frac{a}{4\sigma^{3/2}} \leq \Gamma \leq \frac{a}{\sigma} \tag{7.45}$$

At the left limit of this interval, at which dissipation disappears, the compression ratio of the shock is given by the MHD jump conditions as calculated by Kennel and Coroniti, equation 7.18. The strength parameter of the reflected wave is in this case

$$a_r = \frac{a}{8\sigma}$$

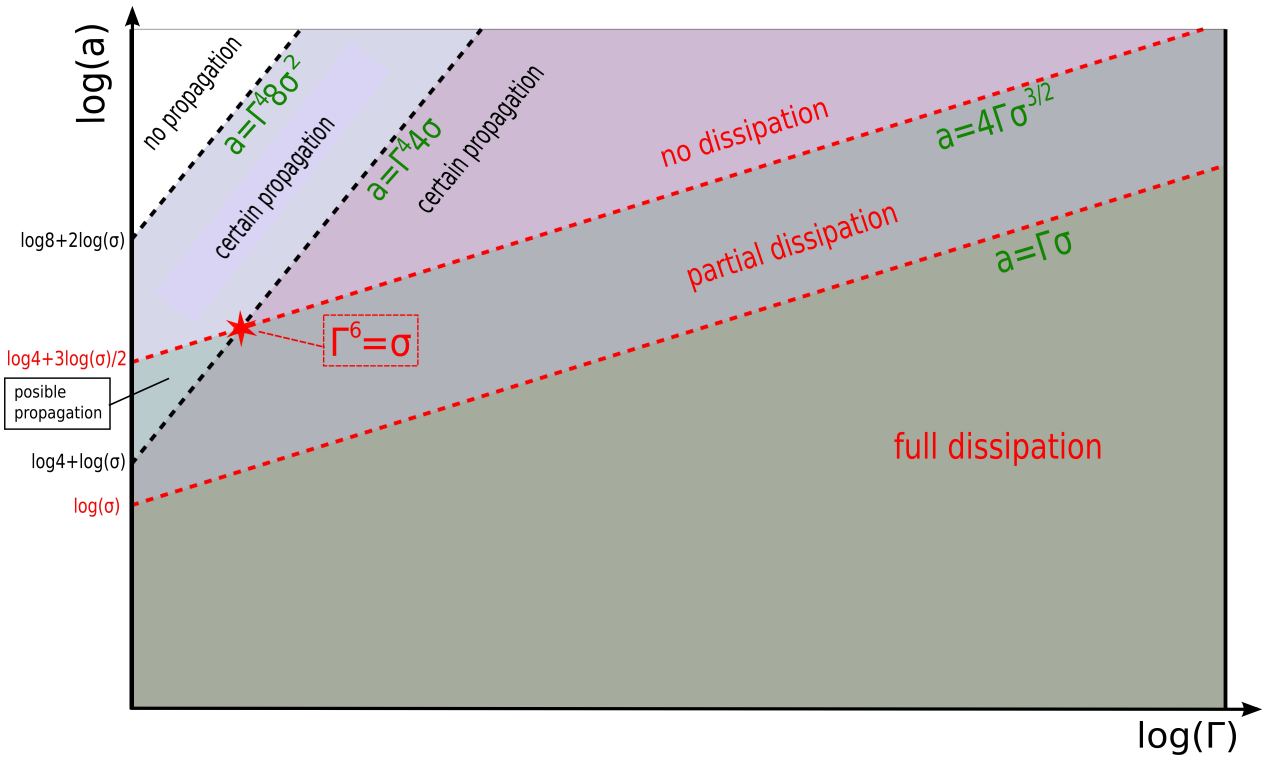

Figure 7.1: **Regions of full, partial and no dissipation and conditions for reflected wave propagation in a** $\log a$**-**$\log\Gamma$ **plot.**
The plot is made for arbitrary magnetization σ*. The three regions of full, partial and no dissipation are separated by the dashed red lines, while the black dotted lines separate regions where waves can propagate from the ones where it cannot (or we cannot know). The lower of these lines,* $a = \Gamma^4 4\sigma$*, refers to the regions of full and partial dissipation, while the upper one,* $a = \Gamma^4 8\sigma^2$*, refers to the no dissipation region. This means that the region between the upper red line and the two black ones is a region of propagation, while the degree of dissipation would decide the propagation in the small triangle formed between the upper red line and the lower black one. In the white region up left there is no wave propagation. The values of* a *at the points of intersection of the lines with the* a*-axis where* $\Gamma = 1$ *are shown on the left of the axis.*

The condition that has to hold for the reflected wave to propagate is then:

$$\Gamma^4 > \frac{a}{8\sigma^2} \tag{7.46}$$

At the right limit of the interval, where dissipation becomes full, the condition becomes stricter, and is given by 7.44 as explained in the above paragraph. Throughout this region of partial dissipation, the generalized condition for the wave to propagate is

$$\Gamma^4 > \delta\frac{a}{4\sigma} \tag{7.47}$$

$$\frac{1}{2\sigma} \leq \delta \leq 1 \tag{7.48}$$

The parameter δ is smaller than unity and depends on the degree of dissipation of the stripes at the shock front, which is unknown. The only definitive conclusion we can get from the above equation is that if $\Gamma^3 > \sqrt{\sigma}$, then the wave propagates in the case of partial dissipation.

No dissipation

The case where there is no magnetic field reconnection at the shock according to Pétri and Lyubarsky is

$$\Gamma \leq a/4\sigma^{3/2} \tag{7.49}$$

The condition of propagation, then, is given by 7.46.

The above results are summarized in the following table:

$\Gamma < a/(4\sigma^{3/2})$	$a/(4\sigma^{3/2}) \leq \Gamma \leq a/\sigma$	$\Gamma > a/\sigma$
$a_r = a/(8\sigma)$	$a_r = \delta a/4$, $1/(2\sigma) < \delta < 1$	$a_r = a/4$
No dissipation	Partial dissipation	Full dissipation
a_r propagates if $\Gamma > a/(8\sigma^2)$ (otherwise not)	a_r propagates if $\Gamma^4 > \alpha/(4\sigma)$ (otherwise uncertain)	a_r always propagates

The regions of full, partial and no dissipation can also be seen in figure 7.4, along with the regions of propagation of the reflected wave.

7.5 A possible precursor

We have argued that the interaction of the striped wind with the termination shock is going to produce a strong reflected component which, in most cases, is going to propagate in the upstream. A self-consistent solution of the full magnetohydrodynamical problem of the interaction of two strong, counter-propagating waves is a formidable problem analytically, which we will not try to tackle here. Instead, we will give some simple arguments about the possibility of the creation of an extended precursor to the shock. These are based on the motion of a single particle of the wind in the field of the two counter-propagating waves, which is much similar to the motions we have investigating in Part I of this thesis. Now the counter-propagating waves have different strength parameters, and one of them (the striped wind) has a phase velocity $\beta_{\rm MHD}$ which is different than unity. However, $\beta_{\rm MHD}$ is so close to unity, that it resembles a light wave for particles that are not *exactly* in phase with it. The wind particles are indeed exactly in phase with the striped wind, however even a small perturbation in their motion will change that. Such a perturbation can be provided by the reflected wave.

Let us introduce the center of momentum frame, which will be defined as the frame moving with respect to the laboratory frame with a lorentz factor

$$\gamma_{\rm com} = \frac{1}{\sqrt{1 - \langle \beta_x \rangle^2}}$$

where $\langle \beta_x \rangle$ is the mean velocity in the direction of propagation of the wave.

Let us now think of the interaction of an electron with the reflected wave and the striped wind as if the two interactions were independent of each other and were not happening simultaneously.

The purpose of this is to get an estimate of the energy imparted to a test particle in the field of the two waves.

If a wind electron were to be treated as a free particle with a Lorentz factor Γ, then its interaction with a counter-propagating wave of strength parameter a_r would have as a result the change of its center-of-momentum Lorentz factor to the value $\gamma_{\rm com} \sim \Gamma/a_r$, provided that $\Gamma > a_r$ (see [52] and [50]) or to $\gamma_{\rm com} \sim a_r/\Gamma$ in the case that $\Gamma < a_r$. In the second case the particle would actually be initially accelerated *backwards*, against the flow. Let us assume that this is indeed the initial recoil of a wind particle for the two cases mentioned when it first interacts with the reflected wave. Now let us bring into the game the strong wave of the pulsar wind.

The particle now is out of phase with the wind and interacts with it as if it was a vacuum wave, as explained above. The wind induces an oscillation of amplitude $\sim a$ (in four-velocity, see Chapter 3 or [50]), in the direction of the electric field and also accelerates the particle in its direction. For the two cases discussed above, a simple estimate gives, using as an initial condition for the motion in the wind the mean velocities and Lorentz factors arising from the interaction of a particle with the reflected wave:

- $\Gamma > a_r$
  The mean energy of the particle rises to
  $$\langle \gamma' \rangle \sim \left(1 + \frac{a^2}{a_r^2}\right) \Gamma$$
  and the center-of- momentum Lorentz factor becomes
  $$\gamma_{\rm com} \sim \frac{a\Gamma}{a_r}$$

- $\Gamma < a_r$
  Now the mean energy is
  $$\langle \gamma' \rangle \sim \frac{a_r^2}{\Gamma}$$
  and the center-of-momentum Lorentz factor is estimated to be
  $$\gamma_{\rm com} \sim \frac{a_r}{a\Gamma} + \frac{a\Gamma}{a_r}$$

Depending on the relationship between a_r, Γ and $a_{\rm eff}$ we can tentatively conclude that there is the possibility that the particle gains a significant amount of energy from the interaction with the two waves, and a large gain in momentum in the direction of the electric field can occur. It is logical to assume that the center-of-momentum motion is always going to be in the direction of the strongest wave, which in this case is always the striped wind, so these particles will always propagate towards the shock.

If the reflected wave is neglected, i.e. if it is considered only as a perturbation that throws a test particle out of phase with the wind, so that it is accelerated in the fields of the wind as in a vacuum wave of strength parameter $a \gg 1$, then the mean energy of the test electron becomes [50]:

$$\langle \gamma \rangle \sim \Gamma a^2$$

and its center-of-momentum motion has a Lorentz factor of

$$\gamma_{\rm com} \sim \Gamma a$$

These results can be extracted from the above equations (in the first case $\Gamma > a_r$) assuming $a_r \to 1$ and $a \gg 1$. The case $a_r < 1$ is not relevant - as we have seen, a weak wave does not change the longitudinal momentum of the particle.

The above estimates are based on considerations about the mean velocities and mean energies of the motion of a single particle in the fields of two counter-propagating electromagnetic waves: the striped wind and a wave reflected from the shock, both of which have been approximated as light waves in vacuum. At best this treatment gives an estimate of the initial response of single particles of the outflow to the reflection of Poynting flux from the shock. If indeed individual particles can be accelerated in the process, then a precursor to the shock should be expected, which changes the dynamics close to the discontinuity. It remains to be seen if future simulations of the interaction of striped winds with a termination shock will reveal behaviour like this described above, and if the precursors resulting from the wave interaction in the upstream will strongly modify the MHD outflow.

Chapter 8

Superluminal waves in magnetized plasma

In contrast to the previous chapter, where we studied the subluminal wave that is the pulsar's striped wind, in this chapter we will investigate superluminal non-linear waves of linear polarization. These waves share some common features with the striped wind: they occupy the same region around the equatorial plane, they are linearly polarized and the mean field rises from zero at the equator until it reaches the value of the wave amplitude at a maximum latitude which depends on the misalignment of the magnetic and rotational axes of the pulsar.

Kennel and Pellat [41] showed that superluminal waves can have arbitrarily large amplitudes. Their analytical treatment, however is far from trivial. The main advantage of waves with superluminal phase speed comes from the fact that one can move to a reference frame where all space dependence vanishes, thus removing many of the nonlinearities that appear in the equations, like for example the convective terms in the equation of motion as explained in Clemmow 1974,1977 [15], [16]. We will name this frame "homogeneous frame" and quantities referring to it will be unprimed. The primed quantities now will refer to the laboratory frame.

In analogy with the wave reflected from the shock front in the case of the striped wind, we will mainly be concerned with waves propagating inwards from the shock. These waves are not *additional* to the wind, rather, we will investigate the possibility that the wind converts to such a superluminal mode *before* reaching the shock. The direction of the phase velocity in itself poses no contradiction, as long as the particle, energy and momentum fluxes and the magnetic flux are conserved during the transition.

8.1 The homogeneous frame

In the investigation of waves of superluminal phase velocity $\beta_\phi c$, it is useful to conduct all calculations in the homogeneous frame where all space dependence vanishes. This is analogous to the wind frame of the striped wind: in that case a Lorentz transformation with velocity $\beta_{\rm MHD}c$ in the direction of the wave brought us to a frame where the wave was static. In the case of the superluminal wave one has to transform to a frame moving with velocity c/β_ϕ in the direction of the wave, to arrive in the homogeneous frame.

In the derivations in this section, we will follow the method used in Kennel and Pellat [41].

However, we will work in the homogeneous frame, and all unprimed quantities refer to this frame. In the following sections, where we need quantities in the shock frame we will simply conduct a Lorentz transformation with velocity c/β_ϕ.

The equations we have to solve are the fluid equations for a cold, two-species collisionless plasma. These consist of Maxwell's equations, the equations of motion and the continuity equation for each species of particles:

$$\nabla \cdot \mathbf{E} = 4\pi\rho \tag{8.1}$$

$$\nabla \cdot \mathbf{B} = 0 \tag{8.2}$$

$$\nabla \times \mathbf{E} = -\frac{1}{c}\frac{\partial \mathbf{B}}{\partial t} \tag{8.3}$$

$$\nabla \times \mathbf{B} = 4\pi\mathbf{j} + \frac{1}{c}\frac{\partial \mathbf{E}}{\partial t} \tag{8.4}$$

$$\frac{\gamma_i}{c}\frac{\partial \mathbf{u}_i}{\partial t} + \mathbf{u}_i \cdot \nabla \mathbf{u}_i = \frac{q_i}{m_i c^2}\left(\gamma_i \mathbf{E} + \mathbf{u}_i \times \mathbf{B}\right) \tag{8.5}$$

$$\frac{\gamma_i}{c}\frac{\partial \gamma_i}{\partial t} + \mathbf{u}_i \cdot \nabla \gamma_i = \frac{q_i}{m_i c^2}\mathbf{u}_i \cdot \mathbf{E} \tag{8.6}$$

$$\frac{1}{c}\frac{\partial}{\partial t}\left(n_i \gamma_i\right) + \nabla \cdot \left(n_i \mathbf{u}_i\right) = 0 \tag{8.7}$$

In the above we have used ρ as the charge density, not to be confused with the shock compression ratio, $\mathbf{j}$ is the current density, $(\gamma_i, \mathbf{u}_i)$ is the four-velocity of each species of particle, γ_i refers to the Lorentz factor and n_i is the proper number density. For the charge and mass we have used the symbols q_i and m_i. However, since electrons and positrons have the same mass and charges of equal magnitude and opposite sign, we will just write m for mass, e for the positron's charge and $-e$ for the electron charge, following the conventions we have been using so far.

The charge and current densities are given by the expressions:

$$\rho = \sum_i n_i q_i \gamma_i = e(n_+\gamma_+ - n_-\gamma_-) \tag{8.8}$$

$$\mathbf{j} = c\sum_i n_i q_i \mathbf{u}_i = ce\left(n_+\mathbf{u}_+ - n_-\mathbf{u}_-\right) \tag{8.9}$$

where we have used the indices "+" and "−" to denote positrons and electrons respectively.

In the homogeneous frame there is no space dependence, therefore all space derivatives disappear from the above equations. One gets then, taking into account 8.8 and 8.9:

$$4\pi e(n_+\gamma_+ - n_-\gamma_-) = 0 \tag{8.10}$$

$$-\frac{1}{c}\frac{d\mathbf{B}}{dt} = 0 \tag{8.11}$$

$$4\pi ce\left(n_+\mathbf{u}_+ - n_-\mathbf{u}_-\right) + \frac{1}{c}\frac{d\mathbf{E}}{dt} = 0 \tag{8.12}$$

$$\frac{\gamma_i}{c}\frac{d\mathbf{u}_i}{dt} = \frac{q_i}{m_i c^2}\left(\gamma_i \mathbf{E} + \mathbf{u}_i \times \mathbf{B}\right) = 0 \tag{8.13}$$

$$\frac{1}{c}\frac{d}{dt}\left(n_i \gamma_i\right) = 0 \tag{8.14}$$

An immediate result is that the magnetic field **B** is constant in the homogeneous frame. From Coulomb's law and the continuity equation, equations 8.10 and 8.14 we have:

$$n_+\gamma_+ = n_0\gamma_0 = n_-\gamma_- \tag{8.15}$$

where the zero subscript indicates the initial condition which we take to be the same for the two species.

We are looking for transverse modes with non-zero E'_y and B'_z components in the laboratory frame for a wave propagating in the positive or negative $x-$direction. This corresponds to non-zero E_y and B_z in the homogeneous frame, and from now on we will drop the subscripts and write just E and B, where the $y-$ and $z-$components are to be understood, respectively. We do not treat longitudinal waves. As explained in the previous chapter, the linear extraordinary mode in an electron-positron plasma is a purely transverse mode, and we will assume the same for its non-linear counterpart. The $z-$component of the equation of motion becomes then

$$\frac{Pu_z}{dt} = 0$$

and if we take the initial condition for $u_{z+,-}$ to be $u_{z+,0} = u_{z-,0} = 0$ then the $z-$component of the four-velocity remains zero for all times. From Ampere's law we have

$$\frac{dE_x}{dt} = 0 \Rightarrow n_+u_{x+} = n_-u_{x-} \tag{8.16}$$

From 8.15 and 8.16 we have

$$\frac{u_{x+}}{\gamma_+} = \frac{u_{x-}}{\gamma_-} \tag{8.17}$$

From the equations of motion for electrons and positrons we get then

$$\frac{du_{y+}}{dt} + \frac{du_{y-}}{dt} = \frac{e}{mc}\left(\frac{u_{x+}}{\gamma_+} - \frac{u_{x-}}{\gamma_-}\right)B \tag{8.18}$$

and because of 8.17 we see that $u_{y+} = -u_{y-} + u_c$ where u_c is a constant. A solution then with $u_c = 0$ can be found for which

$$n_+ = n_- = n \tag{8.19}$$

$$u_{x+} = u_{x-} \tag{8.20}$$

$$u_{y+} = -u_{y-} \tag{8.21}$$

$$u_{z+} = u_{z-} = 0 \tag{8.22}$$

$$\tag{8.23}$$

In the following we will write n_0 for n_+, γ for γ_+, u_x for u_{x+} and u_y for u_{y+} and we will solve the equations for the positron fluid.

We introduce dimensionless electric and magnetic fields as

$$\nu = \frac{eE}{mc\omega} \tag{8.24}$$

$$\Omega = \frac{eB}{mc\omega} \tag{8.25}$$

where ω is the wave frequency. The correspondence with the strength parameter of the vacuum waves is obvious, however here there are two such parameters, one of which (Ω) is constant in the homogeneous frame, while ν is not constant. We will again normalize time t to the inverse of the wave frequency using $\tau = \omega t$. From Ampere's law then, 8.12, we get:

$$\frac{d\nu}{d\tau} = -\frac{u_y}{\alpha\gamma} \tag{8.26}$$

where

$$\alpha = \frac{\omega^2}{2\gamma_0\omega_{p0}^2} \tag{8.27}$$

$$\omega_{p0}^2 = \frac{4\pi n_0 e^2}{m} \tag{8.28}$$

with ω_{p0}^2 is the rest frame plasma frequency of each species. The equations of motion become:

$$\frac{d\gamma}{d\tau} = \frac{u_y}{\gamma}\nu \tag{8.29}$$

$$\frac{du_x}{d\tau} = \frac{u_y}{\gamma}\Omega \tag{8.30}$$

$$\frac{du_y}{d\tau} = \nu - \frac{u_x}{\gamma}\Omega \tag{8.31}$$

From those equations we can work to find an equation governing the behaviour of ν and all other quantities as a function of ν, i.e. as a function of the electric field. Replacing from 8.26 we have for the first two equations:

$$\frac{d\gamma}{d\nu} = -\alpha\nu \tag{8.32}$$

$$\frac{du_x}{d\nu} = \alpha\Omega \tag{8.33}$$

We select the initial conditions $u_x|_0 = p_0$, $\gamma|_0 = \gamma_0$ and $u_y|_0 = 0$ at the point where the electric field reaches its largest modulus ν_0. We also normalize the field to this modulus so that the new field variable becomes $y = \nu/\nu_0$. The modulus of y, then, is always less than or equal to unity, and the initial condition for y is $y_0 = 1$. The solutions for u_x and γ are:

$$u_x = p_0 + \alpha\Omega\nu_0(1 - y) \tag{8.34}$$

$$\gamma = \gamma_0 + \frac{\alpha\nu_0^2}{2}(1 - y^2) \tag{8.35}$$

Now we need an expression for ν as a function of τ, in order to know the dependence of all other quantities on τ, since u_y is given by equation 8.31 as a function of u_x, γ and ν, which

depend only on ν. The same is true for the number densities $n_\pm$ which depend on ν through γ. Squaring equation 8.26 we have

$$\alpha^2\nu_0^2\left(\frac{dy}{d\tau}\right)^2 = \frac{u_y^2}{\gamma^2}$$

Using the identity $u_y^2 = \gamma^2 - u_x^2 - 1$ and the initial condition $\gamma_0^2 - p_0^2 - 1 = 0$ we get an equation for the dimensionless electric field y that is basically the same that Kennel and Pellat derive, but now expressed in the homogeneous frame:

$$\alpha^2\nu_0^2\left(\frac{dy}{d\tau}\right)^2 = \frac{(1-y)^2[(y+1)^2 - 4\lambda^2 - q] + (1-y)qQ}{[q/2 + (1-y^2)]^2} \tag{8.36}$$

$$q = \frac{4\gamma_0}{\alpha\nu_0^2} \tag{8.37}$$

$$Q = 2\left(1 - \frac{p_0}{\gamma_0}\lambda\right) \tag{8.38}$$

$$\lambda = \frac{\Omega}{\nu_0} \tag{8.39}$$

where λ is equal to the ratio of the (constant) magnetic field to the amplitude of the electric field and q is a "weakness" parameter as defined by Kennel and Pellat. The limit $q \to 0$ corresponds to the strong wave limit in the case of the waves propagating in plasma. The main difference between this parameter and the strength parameter of the vacuum waves, is that the initial conditions for the particle proper density and Lorentz factor play a crucial role in whether the wave is strong or weak. Another way to express it, which makes this dependence obvious, is:

$$q = \frac{2(2\gamma_0)^2 4\pi n_0 mc^2}{E_0^2} \tag{8.40}$$

We can see that it is likely that for a highly relativistic fluid, or for large densities, q is going to be large, thus rendering the wave weak.

The dispersion equation for these waves can be found by demanding that the phase of the wave (which is τ in the homogeneous frame) changes by π on the transition from the lowest to the highest value of y, since $dy/d\tau$ does not depend explicitly on τ but only through y. As we have already explained, the largest value of y is unity, and since $\mid y \mid \leq 1$ its lowest value, which corresponds to the smaller amplitude of the wave, has to be in the interval $(-1, 1)$. For a mean magnetic field equal to zero the constants $B = 0$ and $\lambda = 0$ in the homogeneous frame, and the mean values of electric and magnetic fields vanish in the laboratory or any other frame. The oscillation of y then is symmetric around $y = 0$ and the integration is between the values -1 and 1.

Let us denote the lowest allowed value of y by y_1. The demand that the change in phase is π in half a cycle of the wave can be expressed as:

$$\pi = \int_{y_1}^{1} \frac{dy}{dy/d\tau} \tag{8.41}$$

where y_1 is another turning point of y, like the point $y_0 = 1$ which is a root of the denominator $dy/d\tau$ ($u_y = 0$ at $y = 1$ from the initial conditions). The value y_1 corresponds to another point

where the denominator of 8.41 or equivalently u_y becomes zero. In order, then, to find y_1, one must find a root of the denominator y_1 that lies in the interval $(-1, 1)$ and make sure that the quartic polynomial in the numerator of 8.36 remains positive between y_1 and 1. The numerator of 8.36 is

$$(1-y)\{(1-y)[(y+1)^2 - 4\lambda^2 - q] + qQ\}$$

so one needs to find a root of the cubic equation

$$(1-y)[(y+1)^2 - 4\lambda^2 - q] + qQ = 0$$

in the interval $(-1, 1)$. This can be achieved through the trigonometric solution to a cubic, in the case that the cubic has three real roots, or by the reduction to a monic trinomial and then to a binomial, if the cubic has only one root. To be complete, this standard material is briefly presented in Appendix B.

Once the appropriate root has been found, the integration can be performed numerically, taking care of the integrable singularities at y_1 and $y_0 = 1$. In a similar way one can calculate the mean quantities in the wave. For some quantity A than depends on y, like u_x or γ, the mean can be calculated as

$$\langle A \rangle = \frac{1}{\pi} \int_{y_1}^{1} \frac{A(y)}{dy/d\tau} dy \tag{8.42}$$

8.2 Conserved quantities

The mathematical treatment of the non-linear extraordinary mode presented above was conducted following the calculation of Kennel and Pellat [41]. Non-linear superluminal waves have been investigated in their own right (see, for example [58], [15],[16]), or in relation to pulsar outflows ([2],[3]), not, however, in the c context of the conversion of a striped wind to a different wave mode. This is what we will attempt in the remainder of this chapter.

In the previous chapter, we introduced the three parameters μ, ν and η, which are connected with the particle, energy, momentum and magnetic fluxes in the outflow. These are conserved in the striped wind and have to be conserved also across the surface at which it converts to a superluminal wave. This dictates the "jump conditions" of the conversion, in analogy to the conditions at a shock front. The quantities μ, ν and η, then, have to be expressed in terms of the wave parameters.

We have worked in the homogeneous frame up to now, but the fluxes are expressed in the laboratory frame. We introduce, therefore, the group velocity of the wave β_*, which is the velocity of a Lorentz transformation that brings us from the homogeneous to the laboratory frame. The magnitude of the group velocity is the inverse of that of the phase velocity: $\beta_* = 1/\beta_\phi$. We take the wave propagation to be inwards, i.e. from the shock and towards the pulsar. The reason for this is that we are looking for non-linear waves which, as explained in the previous chapter, arise through the interaction of the flow with the shock front and appear as a precursor to the shock.

The quantities $\langle F \rangle$ and $\langle K \rangle$, introduced in Chapter 6 and expressed in terms of striped wind parameters in Chapter 7, are the phase-averaged components T^{01} and T^{11} of the sum of the

stress-momentum tensors of the particles and the fields in the wave. The transformations of these quantities from the homogeneous frame to a frame moving in the positive $x-$direction with respect to it, i.e. the laboratory frame, are:

$$T'^{01} = \langle F' \rangle = -\beta_* \gamma_*^2 \left(T^{00} + T^{11} \right) + \gamma_*^2 \left(1 + \beta_*^2 \right) T^{01} \tag{8.43}$$

$$T'^{11} = \langle K' \rangle = \gamma_*^2 \left(\beta_*^2 T^{00} + T^{11} \right) - 2\beta_* \gamma_*^2 T^{01} \tag{8.44}$$

where γ_* is the Lorentz factor of the transformation from the homogeneous to the laboratory frame

$$\gamma_* = \left(1 - \beta_*^2 \right)^{-1/2}$$

The quantity $\langle H \rangle$, which depends on the phase average of the electric field transforms as

$$\langle H' \rangle = \frac{\gamma_*^2 (\langle E \rangle - \beta_* B)^2}{8\pi} \tag{8.45}$$

and the particle flux is the $x-$component of the four-vector $(n\gamma, n\mathbf{u})$ and is transformed in the primed frame as

$$\langle J' \rangle = 2\gamma_* (\langle n u_x \rangle - \beta_* \langle n\gamma \rangle) c \tag{8.46}$$

with n the proper density of each species. Taking advantage of the fact that the quantity $n\gamma$ is constant and equal to $n_0\gamma_0$ we can write the last equation as:

$$\langle J' \rangle = 2 n_0 \gamma_0 \gamma_* \left(\langle \frac{u_x}{\gamma} \rangle - \beta_* \right) \tag{8.47}$$

The relevant components of the phased-averaged stress-momentum tensors of the particles in the homogeneous frame is [63]:

$$T^{00}_{\text{part}} = 2mc^2 \langle n\gamma^2 \rangle = 2 n_0 \gamma_0 mc^2 \langle \gamma \rangle \tag{8.48}$$

$$T^{01}_{\text{part}} = 2mc^2 \langle n\gamma u_x \rangle = 2 n_0 \gamma_0 mc^2 \langle u_x \rangle \tag{8.49}$$

$$T^{11}_{\text{part}} = 2mc^3 \langle n u_x^2 \rangle = 2 n_0 \gamma_0 mc^3 \langle \frac{u_x^2}{\gamma} \rangle \tag{8.50}$$

and for the electromagnetic field

$$T^{00}_{\text{EM}} = \frac{\langle E^2 \rangle + B^2}{8\pi} = \frac{\langle y^2 \rangle + \lambda^2}{8\pi} \tag{8.51}$$

$$T^{01}_{\text{EM}} = \frac{c\langle E \rangle B}{4\pi} = \frac{c\langle y \rangle B}{4\pi} \tag{8.52}$$

$$T^{11}_{\text{EM}} = T^{00}_{\text{EM}} \tag{8.53}$$

where B does not need averaging since it is constant in the homogeneous frame, and

$$\lambda = \frac{\Omega}{\nu_0} = \frac{B}{E_0}$$

$$y = \frac{\nu}{\nu_0} = \frac{E}{E_0}$$

Taking these equations into account we can calculate μ, ν and η by dividing 8.43,8.44 and 8.45 by the particle flux **??**:

$$\mu = \frac{1}{2n_0\gamma_0\left(\langle\frac{u_x}{\gamma}\rangle - \beta_*\right)}\left[-\beta_*^2\gamma_*\left(T^{00}+T^{11}\right)+\gamma_*\left(1+\beta_*^2\right)T^{01}\right] \tag{8.54}$$

$$\nu = \frac{1}{2n_0\gamma_0\left(\langle\frac{u_x}{\gamma}\rangle - \beta_*\right)}\left[\gamma_*\left(\beta_*^2T^{00}+T^{11}\right)-2\beta_*\gamma_*T^{01}\right] \tag{8.55}$$

$$\eta = \frac{2\gamma_0\gamma_*\left(\langle y\rangle - \beta_*\lambda\right)^2}{q\left(\langle\frac{u_x}{\gamma}\rangle - \beta_*\right)} \tag{8.56}$$

The constants μ, ν and η are specified for a given pulsar through equations7.12. In the transition from the striped wind to the superluminal wave these quantities have to be conserved. For given values of the conserved quantities and a group speed β_*, equations 8.54,8.55,8.56 constitute a non-linear system with three unknowns, which are the variables λ, q and p_0. Here we restrict ourselves to $0 \leq \beta_* < 1$, i.e. for inwards propagating modes.

The system 8.54,8.55,8.56 can be solved numerically using the multi-dimensional Newton Raphson method. However, in order that the method converges to a solution, one needs as input a guess that is close enough to the real solution. In the next section we will describe a way to get such a solution, for the case β_*.

8.3 The $\beta_* = 0$ case

Waves propagating upstream from the termination shock have a minimum group velocity $\beta_* = 0$, which corresponds to infinite phase speed. In this case the homogeneous frame coincides with the laboratory (shock) frame, which means that the wave is stationary in that frame, and one can calculate μ, ν and η as:

$$\mu = \frac{T^{01}}{mc\langle J\rangle} \tag{8.57}$$

$$\nu = \frac{T^{11}}{mc^2\langle J\rangle} \tag{8.58}$$

$$\eta = \frac{\langle y\rangle^2 E_0^2}{8\pi mc\langle J\rangle} \tag{8.59}$$

where all quantities are calculated in the homogeneous frame and can be derived from the formulae given in the last section for $\beta_* = 0$ and $\gamma_* = 1$. The particle flux is

$$\langle J\rangle = 2n_0\gamma_0 c\langle\frac{u_x}{\gamma}\rangle \tag{8.60}$$

and $\langle F\rangle$,$\langle K\rangle$ and $\langle H\rangle$ are:

$$\langle F\rangle = 2n_0\gamma_0 mc^2\langle u_x\rangle + c\frac{\langle y\rangle\lambda}{4\pi}E_0^2 \tag{8.61}$$

$$\langle K\rangle = 2n_0\gamma_0 mc^3\langle\frac{u_x^2}{\gamma}\rangle + \frac{\langle y^2\rangle + \lambda^2}{8\pi}E_0^2 \tag{8.62}$$

$$\langle H\rangle = \frac{\langle y\rangle^2 E_0^2}{8\pi} \tag{8.63}$$

From 8.34, 8.35 and 8.37 we have

$$\langle u_x\rangle = p_0 + \frac{4\lambda\gamma_0}{q}\left(1 - \langle y\rangle\right) \tag{8.64}$$

$$\langle\gamma\rangle = \gamma_0 + \frac{2\gamma_0}{q}\left(1 - \langle y^2\rangle\right) \tag{8.65}$$

Inserting these into the equations for $\langle F\rangle$,$\langle K\rangle$ and $\langle H\rangle$ and dividing by $mc\langle J\rangle$ or $mc^2\langle J\rangle$ as appropriate we arrive to the expressions for μ,ν and η:

$$\mu = \langle\frac{u_x}{\gamma}\rangle^{-1}\left(p_0 + 4\frac{\gamma_0\lambda}{q}\right) \tag{8.66}$$

$$\nu = \langle\frac{u_x}{\gamma}\rangle^{-1}\left[\langle\frac{u_x^2}{\gamma}\rangle + \frac{2\gamma_0}{q}\left(\langle y^2\rangle + \lambda^2\right)\right] \tag{8.67}$$

$$\eta = \langle\frac{u_x}{\gamma}\rangle^{-1}\frac{2\gamma_0\langle y\rangle^2}{q} \tag{8.68}$$

These equations involve integrals of the type 8.42, which are cumbersome to calculate analytically, and even if one were to calculate them the solution of the above system of equations for (λ, q, p_0) would not be feasible analytically. In the next paragraph we will simplify these equations in order to get simple approximate solutions for (λ, q, p_0). These solutions will be used subsequently to calculate accurate solutions by numerical root finding of the system 8.54, 8.55 and 8.56.

8.3.1 The large amplitude limit

In order to simplify the system of equations 8.66,8.67,8.68 we introduce the small parameter ϵ, which is defined by $q = 4\gamma_0\epsilon$. For a large amplitude wave, $q \ll 1$ and $\epsilon \ll 1$. We will assume that the superluminal waves corresponding to the solutions of the above system of equations for a pulsar wind fulfill the large amplitude wave criterion. This requires

$$\frac{\lambda}{\epsilon} \gg p_0$$

and also

$$\gamma_0 \ll \frac{1}{\epsilon}$$

in which case 8.64 and 8.65 can be approximated as

$$\langle u_x\rangle \simeq \frac{\lambda}{\epsilon}\left(1 - \langle y\rangle\right) \tag{8.69}$$

$$\langle\gamma\rangle \simeq \frac{1}{2\epsilon}\left(1 - \langle y^2\rangle\right) \tag{8.70}$$

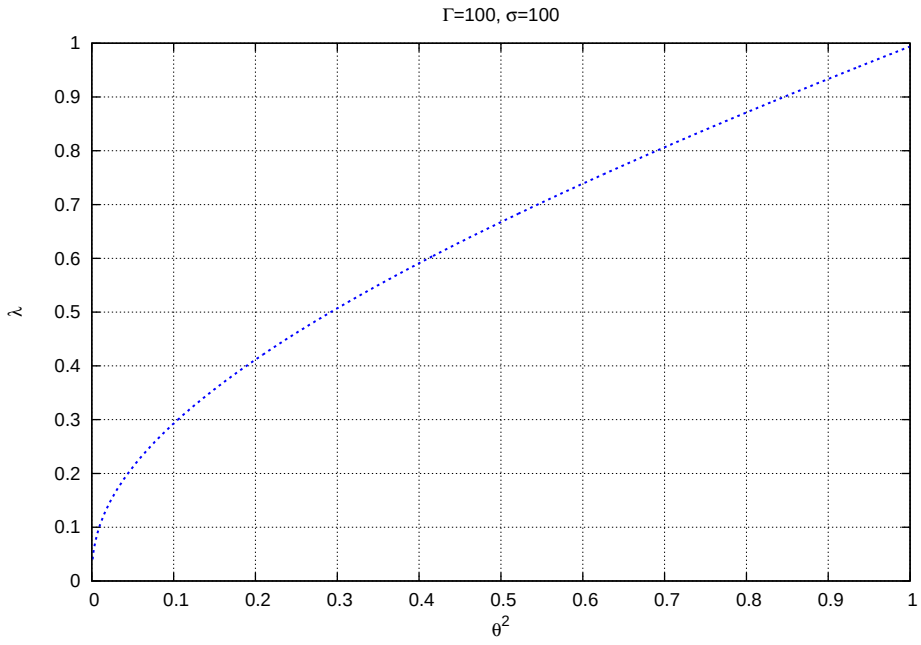

Figure 8.1: λ **as a function of** θ^2 **in the** $q \to 0$ **approximation.**
Numerical solution of equation 8.78 for $\Gamma = 100$, $\sigma = 100$ *as a function of* θ^2 *in the case where the homogeneous frame and the laboratory (shock) frame coincide. When* $\theta = 0$ *we are at the wind's equator, and the mean magnetic field in the superluminal wave is zero,* $\lambda = 0$. *When* $\theta^2 \to 1$ *we move towards the highest latitude in the wind, where the magnetic field becomes constant. Then for the superluminal wave solution* $\lambda \sim 1$*: the magnitude of the magnetic field is close to the electric field amplitude, and* $y_1 \to 1$, *which means that the wave disappears and gives its place to a constant field solution. For* $\Gamma = 100$, $\sigma = 100$ *the solution for* $\theta^2 = 1$ *gives* $\lambda_{\theta^2=1} = 0.994$.

These approximations hold so long as $\langle y \rangle$ and $\langle y^2 \rangle$ are not very close to unity. This condition means essentially that the valid region to look for large amplitude wave solutions is away from the latitudes where we would have $\theta \simeq 1$ in the striped wind, where the oscillation of the electric field is small and the field has an almost constant value. Practically, one can calculate solutions of 8.54,8.55 and 8.56 for values of θ very close to unity, depending on the chosen values for μ and ν, without encountering computational problems.

Using the approximation $q \to 0$ one can simplify the differential equation for the field to:

$$\alpha^2 \nu_0^2 \left(\frac{dy}{d\tau} \right)^2 = \frac{(y+1)^2 - 4\lambda^2}{(1+y)^2} \tag{8.71}$$

and the dispersion relation becomes

$$\alpha \nu_0 = \pi \left(\int_{y_1}^{2} \frac{(1+y)dy}{\sqrt{(1+y)^2 - 4\lambda^2}} \right)^{-1} \tag{8.72}$$

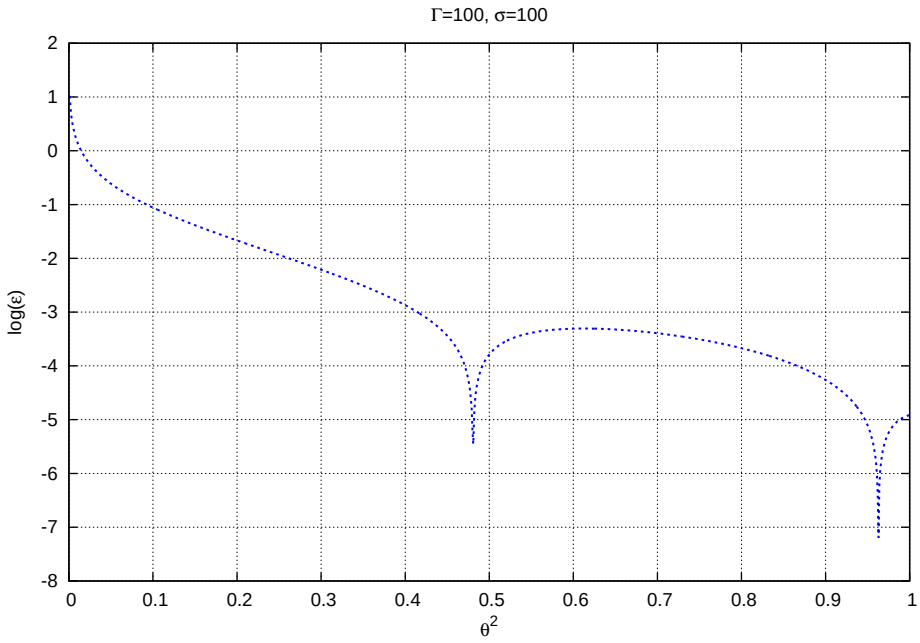

Figure 8.2: **The parameter $\epsilon = q/4\gamma_0$ as a function of θ^2 in the $q \to 0$ limit.** *The logarithm of the parameter ϵ is plotted against θ^2. It is seen that $\epsilon \ll 1$ for all but the smallest θ^2 values, i.e. for the whole wind apart from a small region around the equator.*

where now $y_1 = -1 + 2\lambda$. The integration yields

$$\alpha\nu_0 = \frac{\pi}{2\sqrt{1-\lambda^2}} \tag{8.73}$$

Equations 8.66 and 8.68 become:

$$\mu = \langle\frac{u_x}{\gamma}\rangle^{-1}\frac{\lambda}{\epsilon} \tag{8.74}$$

$$\eta = \langle\frac{u_x}{\gamma}\rangle^{-1}\frac{\langle y\rangle^2}{2\epsilon} \tag{8.75}$$

from which we can extract an equation for λ:

$$\frac{\mu}{\eta} = \frac{2\lambda}{\langle y\rangle^2} \tag{8.76}$$

The integration of y gives

$$\langle y\rangle = \frac{\lambda^2}{\sqrt{1-\lambda^2}}\ln\Lambda$$

where

$$\Lambda = \frac{1+\sqrt{1-\lambda^2}}{\lambda} \tag{8.77}$$

In this way we arrive at an algebraic equation for λ:

$$\ln\Lambda - \sqrt{\frac{2\eta}{\mu}}\sqrt{\frac{1-\lambda^2}{\lambda^3}} = 0 \tag{8.78}$$

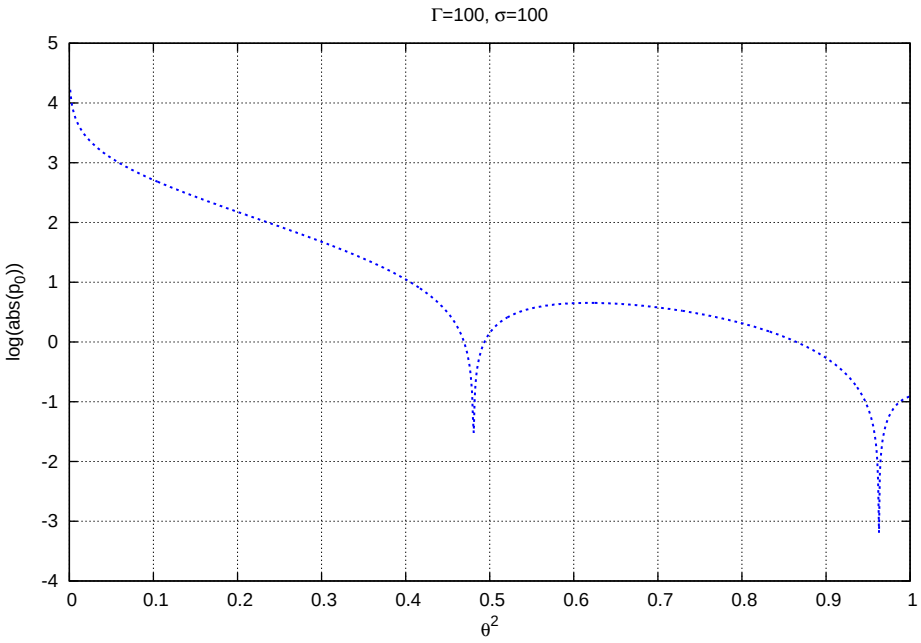

Figure 8.3: **The magnitude of the initial value of the normalized four-momentum p_0 as a function of θ^2. The logarithm $|p_0|$ is plotted.**
The initial four-velocity as a function of θ^2. The downwards spike corresponds to the point where the value of p_0 turns from negative (for smaller θ^2 values) to positive (for larger θ^2 values), and then back to negative for θ^2 approaching unity.

which can be solved numerically. The ratio $2\eta/\mu$ that appears in 8.78 depends on the parameter θ which rises from the equator to the edge of the wind region:

$$\frac{2\eta}{\mu} = \frac{\beta_{\rm MHD}\sigma\theta^2}{1+\sigma}$$

For a highly magnetized ultrarelativistic outflow, $\sigma \gg 1$ and $\beta_{\rm MHD} \simeq 1$ so that

$$\frac{2\eta}{\mu} \simeq \theta^2$$

and 8.78 becomes

$$\ln\Lambda - \sqrt{\theta^2}\sqrt{\frac{1-\lambda^2}{\lambda^3}} = 0 \tag{8.79}$$

The parameter λ, therefore, that expresses the ratio of the magnetic field to the electric field amplitude in a large amplitude superluminal wave in an ultrarelativistic, highly magnetized wind, depends only on the ratio θ of the mean magnetic field to the amplitude of the magnetic field in the striped wind which converts to a superluminal mode.

Equation 8.78 or 8.79 can be solved numerically for different values of θ^2, in a wind with fixed Γ and σ. We have solved 8.78 for $\sigma = 100$ and $\Gamma = 100$ using Mathematica for $0 < \theta^2 < 1$ and the result is plotted in figure 8.1. These values of Γ and σ will be used from now in our calculations. We will use θ^2 rather than θ as a free parameter, since θ can be positive or negative, depending on which hemisphere of the wind it refers to, however results depend only on its magnitude, or

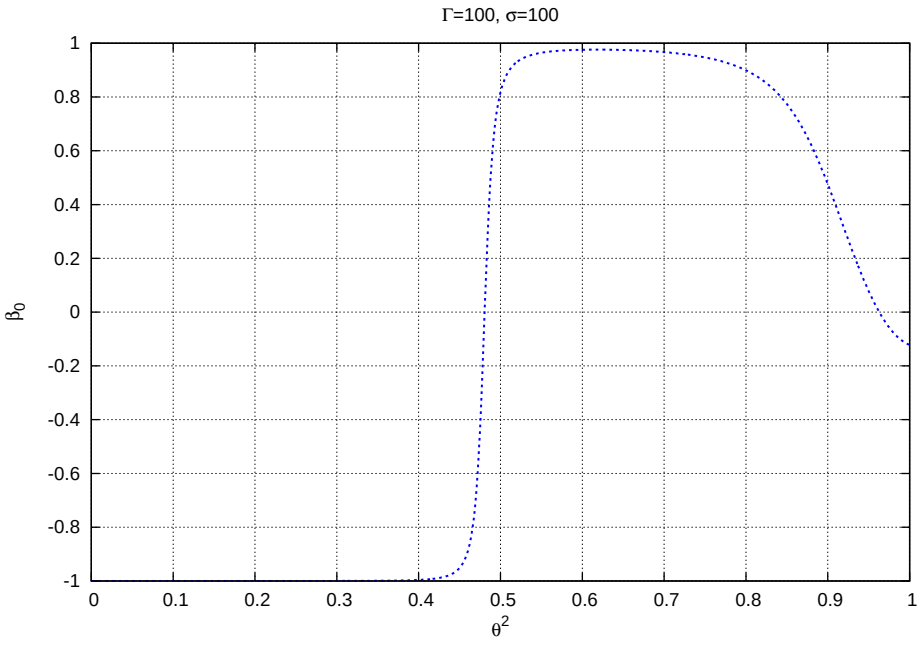

Figure 8.4: **The initial three-velocity given by** $\beta_0 = p_0/\gamma_0 = p_0/\sqrt{1+p_0^2}$**.** *The initial velocity in the radial direction. For the lower* θ^2 *values* β_0 *is negative and it turns positive for larger* θ^2*. The particle flux is defined by the phase average of the quantity* u_x/γ *and is always positive.*

equivalently, θ^2.

From the approximate expressions for μ or η, 8.74 or 8.75 we can now calculate the small parameter ϵ as a function of θ. To do this we need the expression:

$$\langle \frac{u_x}{\gamma} \rangle = \frac{\langle y \rangle}{\lambda} = \frac{\lambda}{\sqrt{1-\lambda^2}} \ln \Lambda$$

which has been calculated using the approximations 8.65 and 8.64. We have then

$$\epsilon = \frac{\lambda^{3/2}}{\sqrt{2\mu\eta}} \tag{8.80}$$

or, for $\Gamma \gg 1$ and $\sigma \gg 1$

$$\epsilon \simeq \frac{\lambda^{3/2}}{\Gamma\sigma|\theta|}$$

The value of ϵ as a function of θ^2 calculated from 8.80 is shown in figure 8.2.

The third parameter we need to calculate is the initial four-velocity p_0. We have not used the equation for ν up to now. Due to the near-degeneracy of μ and ν for a striped wind with $\Gamma \gg 1$ and $\sigma \gg 1$ we can use equation 8.67 in order to calculate p_0, by using the same approximations we have used up to now in this section but keeping one first-order term in p_0 in the numerator of the ratio u_x^2/γ, in order to make the last variable p_0 appear in perturbing the zeroth-order

approximation for u_x^2/γ. This ratio is then approximated by

$$\frac{u_x^2}{\gamma} = \frac{4p_0\lambda(1-y) + 2\lambda^2/\epsilon(1-y^2)}{1-y^2} \tag{8.81}$$

For the calculation of ν we also need the phase average of y^2:

$$\langle y^2 \rangle = \frac{1+8\lambda^2}{3} - 2\frac{\lambda^2}{\sqrt{1-\lambda^2}}\ln\Lambda$$

Then p_0 can be calculated as a function of ν, λ and ϵ:

$$p_0 = \frac{\nu}{2} - \frac{\lambda}{2\epsilon} - \frac{(1-\lambda^2)^{3/2}}{12\epsilon\lambda\ln\Lambda} \tag{8.82}$$

In figure 8.3 we have plotted the logarithm of the magnitude of p_0. Because p_0 changes sign in the interval $0 < \theta < 1$ we have also plotted the $x-$component of the three-velocity $\beta_0 = p_0/\gamma_0$ in figure 8.4.

In the way described in this section we have achieved to calculate a set of parameters $(\lambda, q = 4\gamma_0\epsilon, p_0)$ that approximately solve the set of equations 8.66,8.67,8.68 for each value of θ^2 in a wind of definite μ and ν. These values are approximate: they will be used as an initial guess to the numerical calculation of the root of the equations 8.54, 8.55 and 8.56 for $\beta_* = 0$ and consequently for the general case $\beta_* \neq 0$ in which the superluminal wave propagates in the upstream.

8.4 Propagation in the upstream: exact solutions

The approximate solutions we calculated in the previous paragraph are to be taken with caution. In keeping first-order terms in p_0 in the expression of u_x^2/γ we have ignored terms coming from γ_0 in the full expression of γ in the denominator. For this reason we will not draw any conclusions about the properties of the waves under investigation from them. Their sole purpose is to be used as starting points for the iterative numerical solution of the exact equations 8.54-8.56.

Because these approximate solutions were reached under the condition $\beta_* = 0$, the first step in the numerical solution of the exact equations is to solve them for $\beta_* = 0$ using the set of parameters (λ, q, p_0) calculated approximately, as a guess for the multi-dimensional Newton-Raphson subroutine [74]. If a solution is reached, then we make a small step in β_* and use the values of (λ, q, p_0) found for $\beta_* = 0$ as a guess for the roots of the system 8.54-8.56 for the new β_* value. The iteration is continued in this way for small steps in β_* using each time the previous solution as a guess for the next value of β_* It turns out that at some point no solution can be found numerically once a maximum value of β_* has been reached. This maximum value corresponds to a minimum phase speed. After reaching this extremum we iterate back towards smaller β_*. In this way we trace out a smooth curve in the four dimensional space $(\lambda, q, p_0, \beta_*)$.

In order to connect results in the laboratory frame with a radius in the pulsar wind, we have to connect the luminosity of the wind to the energy flux at some radius. To achieve that we make use of the condition of conservation of particle flux during the conversion of the striped

wind to a superluminal wave:

$$\langle J' \rangle = 2n_0\gamma_0 c\gamma_* \left(\langle \frac{u_x}{\gamma} \rangle - \beta_* \right) = 2N\Gamma\beta_{\rm MHD} c \tag{8.83}$$

From equation 8.47 then, we have

$$\mathcal{F} = \mu mc^2 \langle J' \rangle = \mu 2n_0\gamma_0 mc^3\gamma_* \left(\langle \frac{u_x}{\gamma} \rangle - \beta_* \right) = \frac{\mathcal{L}}{\Omega_w r^2} \tag{8.84}$$

or, using the normalized radius ϱ

$$\frac{\mathcal{L}\omega^2}{\Omega_w \varrho^2 c^2} = \mu 2n_0\gamma_0 mc^3\gamma_* \left(\langle \frac{u_x}{\gamma} \rangle - \beta_* \right) \tag{8.85}$$

The rest frame number density n_0 is an unknown, however it is possible to calculate it from the dispersion equation 8.41 using 8.36. From those we can calculate the quantity $\alpha\nu_0$ as a function of the solution (λ, q, p_0) of our non-linear system of equations. Then we use:

$$\alpha\nu_0 = \frac{\omega^2}{2\gamma_0\omega_{p0}^2}\nu_0 \tag{8.86}$$

to which we can substitute ν_0 from the definition of q:

$$\nu_0 = \frac{4\gamma_0}{\alpha\nu_0 q} \tag{8.87}$$

which gives us

$$n_0 = \frac{2\omega^2}{q(\alpha\nu_0)^2}\frac{m}{4\pi e^2} \tag{8.88}$$

Substituting this to the expression 8.85 we get

$$\varrho = a_L \alpha\nu_0 \sqrt{\frac{q}{4\gamma_0\mu}} \left[\gamma_* \left(\langle \frac{u_x}{\gamma} \rangle - \beta_* \right) \right]^{-1/2} \tag{8.89}$$

where the parameter a_L is defined as

$$a_L = \sqrt{\frac{4\pi e^2 \mathcal{L}}{\Omega_w m^2 c^5}}$$

This corresponds to a strength parameter at the light cylinder $a_L = eE_{\rm eff}/(mc\omega)$ of a wave, the electric field of which is given by $E_{\rm eff}^2 = 4\pi\langle F \rangle/c$ (see [43]).

Let us now introduce a new radius variable:

$$R = \frac{\varrho\sqrt{\mu}}{a_L} \tag{8.90}$$

Now R depends only on q, p_0, λ and the phase velocity:

$$R = \alpha\nu_0 \sqrt{\frac{q}{4\gamma_0}} \left[\gamma_* \left(\langle \frac{u_x}{\gamma} \rangle - \beta_* \right) \right]^{-1/2} \tag{8.91}$$

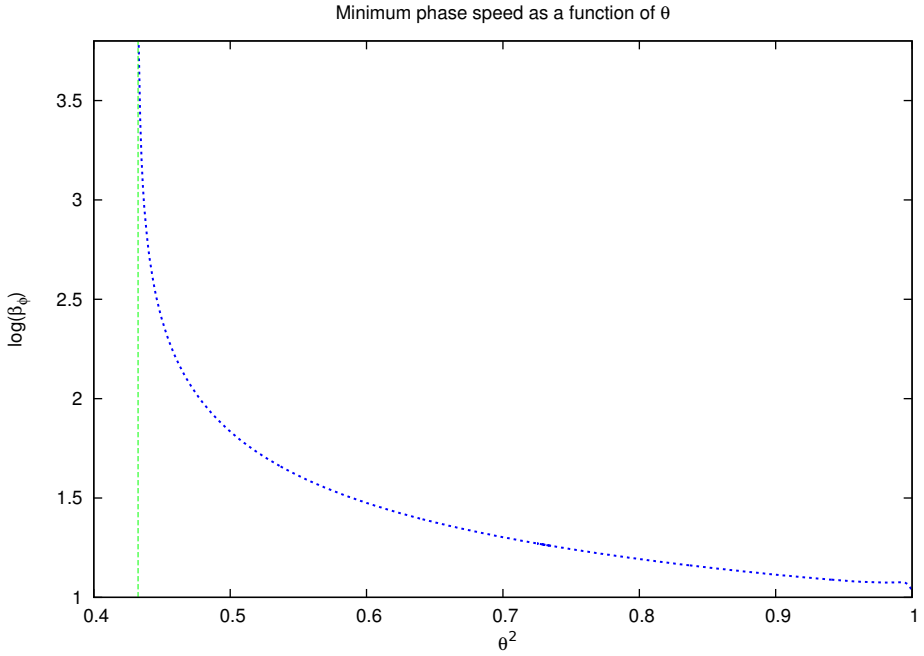

Figure 8.5: **The minimum β_ϕ as a function of θ^2.**
The vertical green line is the limit $\theta^2 = 0.432$. The logarithm of the minimum phase speed is plotted. For $\theta^2 < 0.433$ we have not found inward propagating solutions for the case $\Gamma = 100$, $\sigma = 100$.

This variable is independent of the pulsar's luminosity, and we will use it for our following plots.

8.4.1 Minimum phase velocity

As we have already mentioned, we have numerically solved the equations 8.54, 8.55 and 8.56 for the values $\Gamma = 100$ and $\sigma = 100$, which correspond to $\mu = \Gamma(1+\sigma) = 10100$ and $\nu = (\Gamma^2-1)^{-1/2}\left[\Gamma^2(1+\sigma) - (1+\sigma/2)\right] = 10099.995$ and for a set of different θ^2 values in the interval $0 \leq \theta^2 \leq 1$. Specifically, we have started from the value $\theta^2 = 0.001$ and have solved the above equations for 1000 θ^2 values, using the step $\delta\theta^2 = 0.001$. Using the method described above, for each θ^2 we started our iteration from the value $\beta_* = 0$ which corresponds to $\beta_\phi \to \infty$ and calculated the solution (λ, q, p_0) for small steps in β_*. From the calculation it turns out that for each value of θ^2, to which a set of equations corresponds, there is a maximum value of β_* for which there are solutions. This $\beta_{*,\max}$ corresponds to a minimum phase velocity $\beta_{\phi,\min}$.

For $\theta^2 = 1$, $\beta_{\phi,\min}$ is very close to unity. However as one moves to lower θ^2, $\beta_{\phi,\min}$ rises, until for some value of θ^2 $\beta_{\phi,\min} \to \infty$ and there is no solution of the equations 8.54,8.55,8.56 below this value. For the example we have calculated, a finite $\beta_{\phi,\min}$ exists for $\theta^2 \geq 0.433$. This is shown in figure 8.5 where we have plotted the logarithm of $\beta_{\phi,\min}$ as a function of θ^2. The large rise towards lower θ^2 is evident. Below the green line, $\theta^2 \simeq 0.432$ there is no inward propagating solution, and also no standing wave solutions in the laboratory frame (solutions with $\beta_* = 0$) which means that the striped wind cannot convert to an inward propagating wave in the lower latitudes.

Connecting solutions with the dimensionless radius R from the equations 8.89 and 8.90 we can plot the Lorentz factor γ_* corresponding to the phase velocity of the wave through

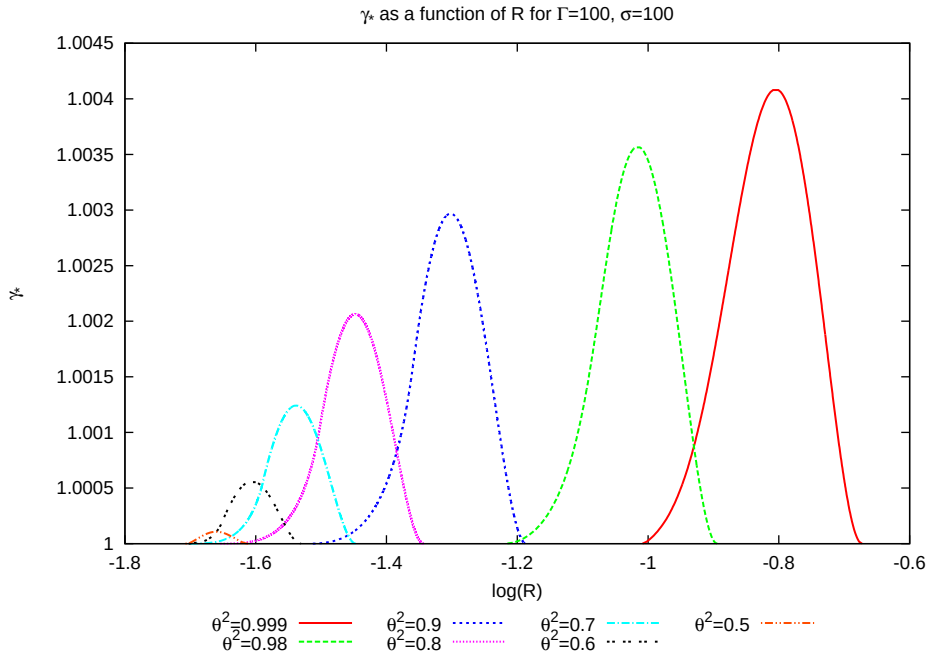

Figure 8.6: **The Lorentz factor γ_* as a function of the dimensionless radius R for various values of θ^2, in the case $\Gamma = 100$, $\sigma = 100$.**
The peak of each curve corresponds to a maximum value of γ_* which is connected to a minimum value in phase velocity β_ϕ, as seen in figure 8.5. Conversion from the striped wind to the superluminal inwards propagating mode happens at each latitude inside of a finite range of radii, which is smaller than an order of magnitude in R.

$\gamma_* = \beta_\phi/\sqrt{\beta_\phi^2 - 1}$. In figure 8.6 we show γ_* as a function of R for different values of θ^2. Here we can see that the conversion of the wind into a wave, either standing or inward propagating, is only possible for certain radius intervals. These intervals depend on θ^2, however the variation is not large: from the largest radius (for $\theta^2 = 1$) to the lowest where conversion can occur, the difference in R is one order of magnitude, which means that the whole wind converts to a superluminal wave within a restricted radius interval.

8.4.2 A new "magnetization" parameter

In order to estimate how much energy is transferred from the fields to the particles in the transition from the striped wind to the superluminal wave, we introduce a new "magnetization parameter" which is defined as the phase-averaged Poynting flux in the laboratory frame divided by the phase-averaged kinetic energy flux in the same frame. In other words, it is the ratio of the T^{01} components of the stress-energy tensor of the fields and particles in the laboratory frame. This parameter corresponds to the magnetization parameter in the striped wind σ which is defined in the same way. We choose the symbol σ_w for this new parameter:

$$\sigma_w = \frac{T^{01}_{\mathrm{EM,lab}}}{T^{01}_{\mathrm{part,lab}}} = \frac{4\gamma_0}{q}\frac{-\beta_*(\langle y^2\rangle + \lambda^2) + (1+\beta_*^2)\langle y\rangle\lambda}{-\beta_*(\langle\gamma\rangle + \langle\frac{u_x^2}{\gamma}\rangle) + (1+\beta_*^2)\langle u_x\rangle} \tag{8.92}$$

If $\sigma_w/\sigma < 1$ then during the transition from the striped wind to the superluminal wave

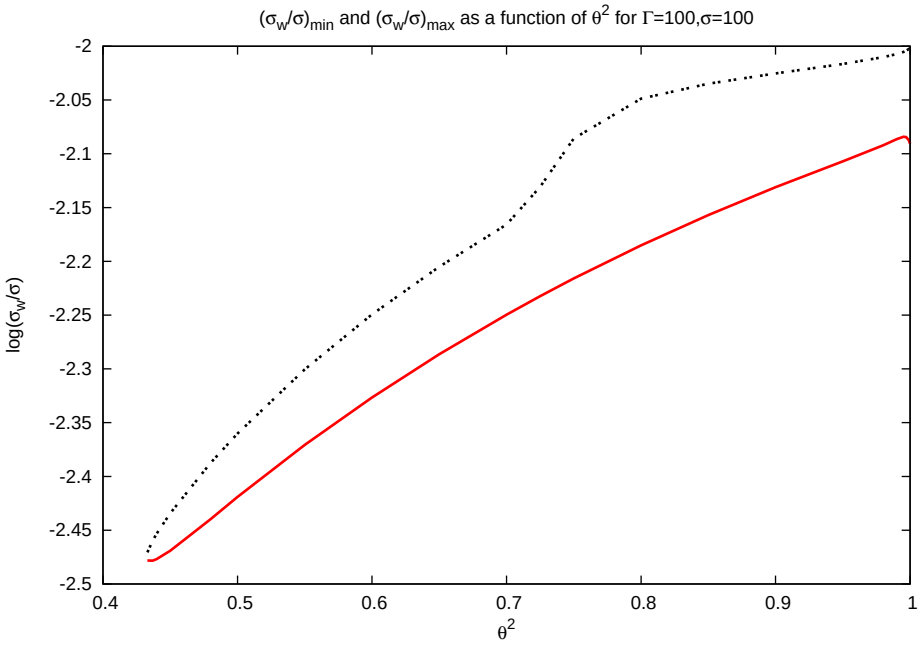

Figure 8.7: **The maximum and minimum values of the ratio σ_w/σ as a function of θ^2, for the case $\Gamma = 100$ and $\sigma = 100$.**

energy is transferred from the fields to the particles. In figure 8.7 we plot the logarithm of the ratio σ_w/σ as a function of θ^2. Plotted are the largest and lowest ratios for each θ^2, which depend on the phase velocity of the wave. It is readily seen that for all values of θ^2 for which there is a solution, σ_w is at least two orders of magnitude lower than σ. The "magnetization" in the wave is $\sigma_w < 1$, which means that the outflow is converted from Poynting-dominated to kinetically dominated.

Another example: $\Gamma = 1000$**,** $\sigma = 100$

In order to investigate if results vary strongly when we vary parameters in the striped wind, we repeated the above calculation for different values of μ and ν, corresponding to $\Gamma = 1000$ and $\sigma = 100$. Some curves of γ_* as a function of R for the same values of θ as in figure 8.6 are shown in figure 8.8. The first result is that there is the same cutoff at values $\theta^2 < 0.433$, i.e. waves do not propagate upstream for these values of θ^2. The form of the curves $\gamma_* - R$ is very similar in the two cases, but in the larger Lorentz factor case the dimensionless radius R is by half an order of magnitude smaller.

Also, as we can see from figure 8.9, the drop in the magnetization is similar in the two cases: the curves have a similar shape and the ratio σ_w/σ is of the same order of magnitude. The magnetization drops also in this case by more than two orders of magnitude.

8.5 Discussion and implications for pulsar outflows

We have seen that the wind can convert to a superluminal mode in a certain allowed range of latitudes as expressed by θ, and this conversion occurs at certain restricted range of radii. What

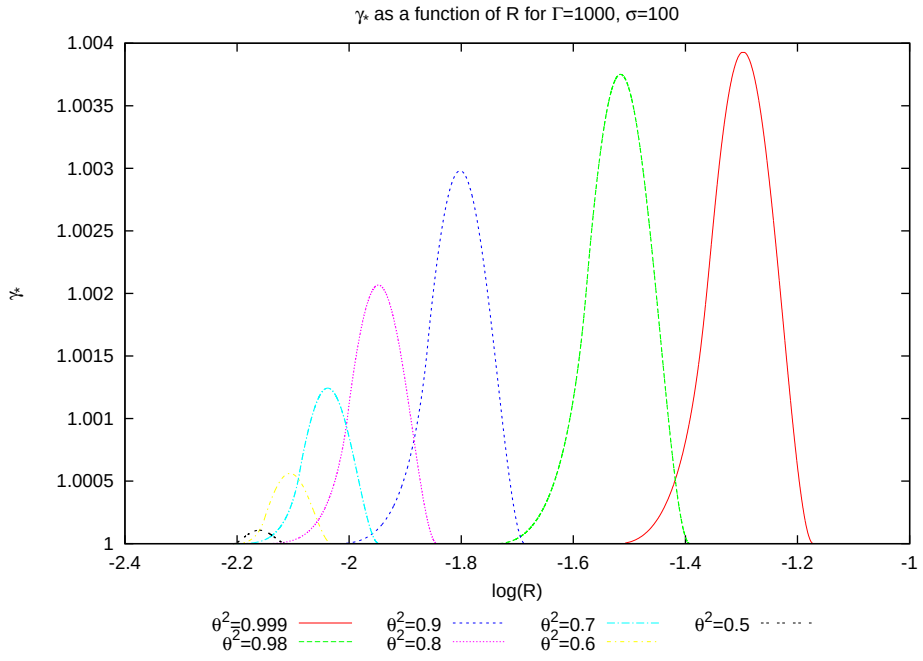

Figure 8.8: **The Lorentz factor γ_* as a function of the dimensionless radius R for various values of θ^2, in the case $\Gamma = 1000$, $\sigma = 100$.**
The same as 8.6, for larger Γ.

we have examined are essentially "jump conditions", similar to those holding for a shock, which dictate that certain conservation laws have to hold during the transition of the wind from a certain state (MHD striped wind) to another (superluminal wave). We have observed that this transition can take place only in a limited range in radius. After the conversion, in order to follow the evolution of the wave over several orders of magnitude in radii towards the termination shock, one would have to solve the system of equations in spherical geometry, something that is beyond the scope of the present work.

For the first case we have examined, $\Gamma = 100$, $\sigma = 100$, the dimensionless radius is confined in the range $R \sim 10^{-1.7} - 10^{-0.7}$, while in the second case, $\Gamma = 1000$, $\sigma = 100$ it lies in the range $R \sim 10^{-2.2} - 10^{-1.2}$. Most pulsars have spin-down luminosities in the range $\mathcal{L} \simeq 10^{33} - 10^{38}$erg/sec. Assuming $\Omega_w \sim 1$ we can see that the above intervals in radius translate to $\varrho \sim 10^{2.8} - 10^{3.8}$ in light cylinder radii for the lower luminosity end to $\varrho \sim 10^{5.4} - 10^{6.4}$ in the higher luminosity end. In both the cases the result is roughly the same, because the half order of magnitude in R is compensated by the value of $\sqrt{\mu}$ with which R is divided to get ϱ. One can tentatively take this as an indication that there is a characteristic radius of conversion, that depends only on the pulsar's luminosity and the solid angle Ω_w, i.e. the inclination of the magnetic axis of the pulsar with respect to its rotational axis. However, we have not examined if this radius changes for a different value of the magnetization σ.

For a pulsar with luminosity comparable to the Crab pulsar's, then, the conversion would happen at a distance $\sim 10^6$ light cylinder radii from the star. In Crab's case, the termination shock is estimated to be at a distance of $\varrho \sim 10^9$ at the equator. However, the solutions we have found correspond to larger latitudes, where the shock is predicted to be closer to the pulsar,

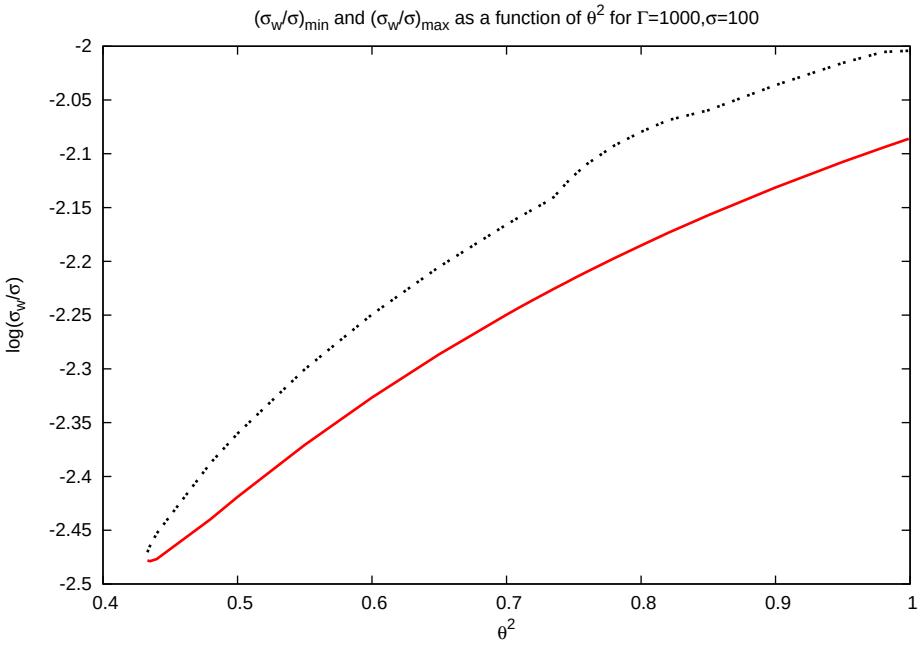

Figure 8.9: **The maximum and minimum values of the ratio σ_w/σ as a function of θ^2, for the case $\Gamma = 1000$ and $\sigma = 100$.**

due to the diminished energy carried in higher latitudes in combination with the condition of pressure balance between the nebula and the wind's ram pressure at the shock (see for example Lyubarsky 2002 [55] for a more detailed explanation). This non-spherical shape of the shock is shown schematically in figure 8.6. This effect is strengthened by the fall of luminosity with latitude. We have assumed in the previous chapter that the energy imparted by the pulsar to the wind is evenly distributed in the solid angle Ω_w. If, however, this is not true, then for larger latitudes in the wind there will be an additional fall in the allowed range of R due to the diminishing of the energy flux in the outflow.

In this way the possibility arises that the termination shock falls into the range of radii which we have calculated above for the corresponding θ. Should this be the case, the conversion of the striped wind to such a wave is possible, since as we have argued the wave is generated by the interaction of the wind with its termination shock.

There is then, in principle, a mechanism that can convert a high σ flow to a low σ one just before the outflow reaches the termination shock. The conversion of the striped wind to a superluminal wave is, therefore, a highly efficient mechanism for particle acceleration, where energy is extracted from the fields and is imparted to the cold particles of the outflow. This could lead to an extended precursor to the shock, which thermalizes particles and converts the high-σ wind to a flow with $\sigma_w \sim 0.1 - 1$ (in the cases that we have investigated, which had initial magnetization $\sigma = 100$, see figures 8.7 and 8.9). As we have already mentioned, a low σ flow can produce a strong shock, one that has the capability of further thermalizing the outflow [40]. This would be in agreement with observations of the Crab nebula, to name an example, where the magnetization downstream is estimated to be of the order $\sigma \sim 10^{-3}$ [40].

The special quality of the modes we have examined is that they are propagating inwards (or

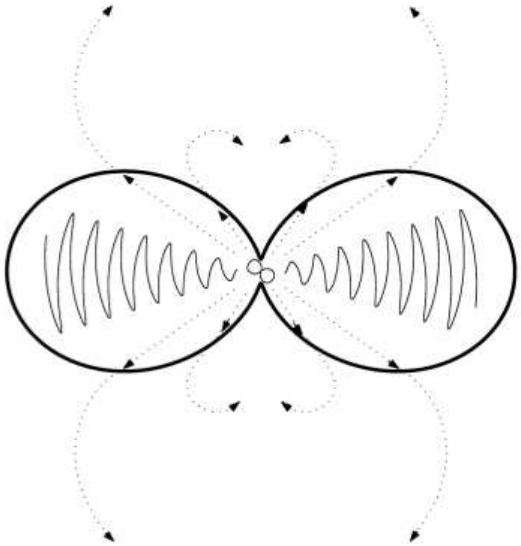

Figure 8.10: **The non-sphericality of the termination shock.**
The termination shock, seen as the thick black line, is much closer to the pulsar at high latitudes, because the energy flux carried by the wind decreases towards higher latitudes (not to scale). The figure is taken from Lyubarsky 2002 [55].

the shock frame coincides with the frame where the wave is homogeneous). The motivation to look for such waves came from the observation, made in Chapter 7, that reflection of Poynting flux at the termination shock can have as a result the propagation of a wave upstream and that the interaction of a wave carried outwards from the pulsar, with a wave propagating inwards from the termination shock will have as a result a precursor in which particles would be accelerated because of the energy transfer from the fields to the particles of the outflow. The direction of the phase velocity of the modes found is not important, as far as the wave is able to carry the wind's energy, momentum and particles outwards towards the shock during the conversion, as indeed we have shown is the case.

8.6 Other modes and future work

Apart from the modes we have been examining, one can assume that there will exist also linearly polarized forward- propagating waves. These are the linearly polarized counterparts to the circularly polarized modes investigated by Kirk 2010 [43]. They are expected to have a mean magnetic field which is zero at the equator and would rise to a value close to unity at the highest latitude where $\theta^2 = 1$, if indeed they exist for all latitudes (something which, as we have seen, is not the case in the stationary and backwards propagating modes).

In the present work we have not investigated forward-propagating modes, but it is logical to assume that they exist and might have characteristics similar to their circularly polarized counterparts as examined in [43], at least in the case where the mean field is zero. A particularly interesting question would be whether the ratio of Poynting to kinetic energy flux in this case would rise or fall during a conversion, since a rise was predicted for the circularly polarized modes.

In the present work we have refrained from investigating these modes, because we were explicitly looking for waves propagating upstream, as a result of the interaction of the wind with the termination shock. However, they could be the object of a future investigation, since outgoing waves could exist where the ingoing ones cannot propagate, i.e. for the lower latitudes.

In the calculations presented in this chapter, we have attempted to give some meaningful

results for two sets of realistic parameters in pulsar winds. The numerical calculation of these results is difficult when the Lorentz factor of the outflow or the magnetization parameter become large, due to the near-degeneracy of μ and ν. However, one might attempt to compute solutions for realistic values of Γ and σ as inferred from observations and simulations of pulsar winds in order to apply them to individual objects. In the case of isolated pulsars (for example the well-known and well-studied Crab and Vela pulsars) the magnetization problem might be addressed, while in the case of pulsars in binary systems (for example systems with a Be star like the TeV binary PSR B1259-63) one could investigate the effects of the conversion to a superluminal mode when two stellar winds collide.

A significant issue that arises here is that of radiation. Since the cold wind particles are accelerated during the conversion process, they are expected to radiate in the electromagnetic field of the wave. The particles are highly relativistic and the radiation will be beamed in the direction of propagation of the wind, so it would be important to find out whether this radiation is observable or not. Furthermore, since the wave has the frequency of the rotator, another interesting question would be whether the radiation reaching an observer would be continuous or pulsed.

Asseo et al. [1] have predicted that a superluminal linearly polarized plane wave in a rapid rotator like the Crab pulsar will be damped within ~ 10 wavelengths due to radiation reaction. However their discussion was taking into account only outward propagating waves with a mean magnetic field equal to zero. Since the outward and inward propagating modes are expected to have different characteristics, it would be interesting to investigate whether radiation damping would be significant for the modes examined in this chapter. The same investigation might be applied to outward propagating waves with non-zero average fields, since the $\langle B \rangle = 0$ case is very special and applies only at a pulsar wind's equator.

Chapter 9

Summary and Conclusions

In this last chapter we briefly summarize the methods and results of our research in the subjects of pair production using counter-propagating laser beams of ultra-high intensity and the conversion of a striped pulsar wind to a superluminal wave propagating upstream from the wind's termination shock.

9.1 The prospect of pair production in ultra-high intensity lasers

In the first part of this thesis we investigated the possibility of prolific electron-positron pair production using next generation laser facilities like the Vulcan 10PW ultra-high intensity laser, or the lasers under construction in ELI facilities. We showed that the ultra-short, ultra-high intensity laser beams expected to be produced in these and other facilities would have strength parameters of the order of hundreds and reviewed the processes of particle acceleration, radiation and pair production in the fields of strong waves. We presented two experiments that have already lead to pair production in the laboratory, using a high-intensity laser beam as an accelerator of electrons in one case, and as a target for high energy electrons from a linear accelerator in the second case. We argued that a counter-propagating beam configuration would combine the advantages of using lasers both as accelerators and targets. Taking as a starting point the calculations of Bell and Kirk [7], which were restricted to particle trajectories on the magnetic field nodes of two very long, counter-propagating, circularly polarized beams, we showed that circular polarization is actually not ideal for pair production, and that other polarizations might be more effective in this regard.

We then numerically calculated the acceleration of electrons and the probability of pair production by one electron in the field of linearly polarized beams of a finite duration. The length of these pulses was set to be a few wavelengths and the polarization vectors of the two pulses were either parallel or perpendicular. We also included one case where the second pulse was simulating one reflected from a solid surface. The results of these calculations were that, for intensities approaching $10^{24}\mathrm{Wcm}^{-2}$ the probability of one particle producing one $e^+ - e^-$ pair in the field of the counter-propagating pulses is approaching unity. The results were not substantially different for the three cases we studied, i.e. for different polarization alignments and pulse shapes. Conducting the same calculation for circularly polarized pulses, either of the same or of opposite handedness, the results showed that the number of pairs produced in this

case is reduced by several orders of magnitude.

From the results described above we can conclude that not only pair production in the focus of linearly polarized, counter- propagating laser beams by pre-existing electrons can be a significant effect, but also that the secondary particles can be accelerated themselves and produce new pairs, thus initiating an electromagnetic cascade. We have estimated the threshold for this process to be at an intensity value of $I \sim 10^{23.86}\mathrm{Wcm}^{-2}$. These cascades could develop rapidly in the focus of the beams, leading possibly to the depletion of their energy.

Encouraging as these results might be, one has to consider that our calculations did not take into account the discontinuous nature of the particle trajectory due to quantum effects in the strong field of the interacting beams. Throughout the calculation we have treated the motion of the electron classically, the only quantum mechanical effect being the reduction in the total emitted radiation in strong fields given by the quantum synchrotron formula. However, it has been predicted [81] that the quantum effects in the particle trajectories lead to a significant spread in the electron energy which will have a positive effect on pair production [19].

9.2 Pulsar winds as large amplitude superluminal waves

In the second part of this thesis we investigated the possibility of the conversion of a striped pulsar wind to a superluminal large amplitude wave. The motivation for the search for such modes were the following two observations: firstly, the pulsar wind's magnetization (the ratio of the Poynting flux to the kinetic energy flux) is predicted to be much higher than unity upstream of the termination shock but lower than unity in the nebula, downstream of the shock. Secondly, unless the wind is accelerated to a very high bulk Lorentz factor, the problem of current starvation might arise, where the currents in the wind are not able to support the fields any more, due to the rapid decrease of particle density with radius, and displacement currents might appear.

After reviewing the model of the pulsar's striped wind, and noting that it is a strong wave with strength parameter decreasing with distance from the pulsar, we introduced a set of parameters that are conserved in the striped wind and also have to be conserved during the conversion of the wind to a superluminal wave. This way we arrived at a set of "jump conditions" for the process discussed, to be used subsequently in fixing the characteristics of the superluminal wave for any given pulsar wind with certain bulk Lorentz factor of the outflow Γ and magnetization σ. Using the pulsar's luminosity we showed how one can connect the wave solution to a certain radius in the wind.

Consequently we derived the conditions necessary for the current sheets to be very thin in comparison to the stripe's wavelength, so that the wind's field can be approximated at the equator as a square wave, and we presented some well- known characteristics of perpendicular shocks. We argued that, even in the absence of current starvation, where the striped wind arrives at the shock front undisturbed, there is bound to be some reflection of Poynting flux due to alternating currents at the shock. This wave, propagating upstream, might perturb the trajectories of test particles in the cold wind in such a way as to cause their acceleration in the field of the wind.

However, an analytical description of the interaction of the two waves in a magneto- hydrodynamic outflow is not feasible. This is why we assumed that the interaction of the wind with the reflected component can have as a result a new wave, propagating upstream with superluminal phase speed, and investigated the possibility of the conversion of a pulsar striped wind to this wave. We found that this conversion is not possible for all latitudes in the wind, and there is a region around the equator where these waves cannot propagate. However, in the region where propagation is possible, significant transfer of Poynting flux to kinetic energy flux is predicted. This means that particles are accelerated during the conversion, and a precursor to the termination shock is expected to form. The radii in a pulsar wind for which these solutions exist, depend on the pulsar's luminosity as stated above. For the Crab pulsar, these radii are several orders of magnitude smaller than the radius of the termination shock at the equator, and could be smaller if one takes into account the uneven distribution of luminosity with latitude. However, the shock is expected to be closer to the pulsar's rotational axis in higher latitudes, for which we have found solutions. It is, therefore, possible, that a wave propagates upstream from the shock at those latitudes, accelerating the flow, thermalizing particles and creating a precursor where the magnetization parameter falls from a value much higher than unity to a value slightly smaller than unity.

Even though these results are quite promising, one should take into consideration the fact that inward-propagating solutions have not been found around the pulsar wind's equator. It is likely that outward propagating modes exist there, however if they behave similarly to their circularly-polarized counterparts investigated by Kirk [43], they might not result in the transfer of energy from the fields to the particles, but rather the opposite. Also the issues of particle radiation and radiation damping in the superluminal waves have not been discussed in this thesis. We leave these as a subject of a future work.

Appendix A

Functions used in the calculation of pair production

A.1 The functions M_i,J_i

The expressions for the functions M_i, J_i depend on combinations of the invariant parameters χ and η. These are

$$\xi = \frac{2\chi}{\eta}$$

$$\zeta = \frac{2\chi}{3\eta(\eta - 2\chi)}$$

The functions, then, are given by the following expressions (as reviewed by Erber 1966, [20]):

$$M_1(\xi) = 1 + \frac{1}{(1-\xi)^2} \tag{A.1}$$

$$M_2(\xi) = \frac{2}{1-\xi} \tag{A.2}$$

$$M_3(\xi) = \left(\frac{\xi}{1-\xi}\right)^2 \tag{A.3}$$

and

$$J_1(\zeta) = \frac{1}{3\zeta^2}\int_\zeta^\infty \frac{sds}{\sqrt{\left(\frac{s}{\zeta}\right)^{2/3} - 1}} K^2_{2/3}(s) \tag{A.4}$$

$$J_2(\zeta) = \frac{1}{3\zeta}\int_\zeta^\infty \left(\frac{s}{\zeta}\right)^{(1/3)} \sqrt{\left(\frac{s}{\zeta}\right)^{2/3} - 1} K^2_{1/3}(s) \tag{A.5}$$

$$J_3(\zeta) = \frac{1}{3\zeta}\int_\zeta^\infty \left(\frac{s}{\zeta}\right) \sqrt{\left(\frac{s}{\zeta}\right)^{2} - 1} K^2_{1/3}(s) \tag{A.6}$$

A.2 The function $\hat{\Omega}(\eta)$

The function $\hat{\Omega}(\eta)$ which appears in the calculation of the trident pair production is given by

$$\hat{\Omega}(\eta) = \frac{\pi}{16} G^{6,0}_{2,6}\left(\left.\frac{16}{9\eta^2}\right| \begin{matrix} 1, & 3/2 \\ 0\,, & 0\,, \quad 1/6\,, \quad 1/2\,, \quad 5/6\,, \quad 2 \end{matrix}\right)$$

where G is the Meijer function, given by

$$G^{m,n}_{p,q}\left(x\left| \begin{matrix} a_1 & , & \dots & , & a_p \\ b_1 & , & \dots & , & b_q \end{matrix}\right.\right) \equiv \frac{1}{2\pi i}\int_{\gamma_L} \frac{\prod_{j=1}^{m}\Gamma(b_j - s)\prod_{j=1}^{n}\Gamma(1-a_j+s)}{\prod_{j=n+1}^{p}\Gamma(a_j - s)\prod_{j=m+1}^{q}\Gamma(1-b_j+s)} x^s ds$$

where $\Gamma(x)$ is the gamma function and the contour γ_L lies between the poles of $\Gamma(1-a_j+s)$ and the poles of $\Gamma(b_j - s)$. The Meijer function has a very general formulation, which reduces to simpler functions in many special cases.

Appendix B

Solution of a cubic equation with three real roots

This is a standard way to solve a cubic equation with three real roots, which we include for the sake of completeness (see for example [27]).

In order to solve the cubic, the first step is to eliminate the second-order term by a change of variable. If the original equation is

$$x^3 + ax^2 + bx + c = 0$$

then the change of variable

$$x = u - \frac{1}{3}a$$

brings the equation to the form

$$u^3 + \left(b - \frac{a^2}{3}\right)u + \left(\frac{2a^3}{27} - \frac{ab}{3} + c\right) = 0$$

Renaming the coefficients of the first- and zero-order terms p and q respectively, the equation to solve becomes now

$$u^3 + pu + q = 0 \tag{B.1}$$

Next we notice that for a complex number z with magnitude r and phase α, or real part x and imaginary part y, the following expressions are true:

$$z = re^{i\alpha} = x + iy \tag{B.2}$$

$$z^3 = r^3\left(\cos 3\alpha + i \sin 3\alpha\right) \tag{B.3}$$

$$z^3 = x^3 - 3xy^2 - i(y^3 - 3x^2y) \tag{B.4}$$

Taking into account that $r^2 = x^2 + y^2$ B.4 becomes

$$z^3 = x^3 - 3x(r^2 - x^2) - i(y^3 - 3x^2y)$$

and from B.3 and B.4 we get

$$4x^3 - 3r^2x = r^3 \cos 3\alpha$$

Dividing by the coefficient of the first term, we finally get

$$x^3 - \frac{3r^2}{4}x - \frac{r^3}{4}\cos\alpha = 0 \tag{B.5}$$

Equations B.5 and B.1 are of the same form, and we can equate the coefficients of the same terms:

$$-\frac{3r^2}{4} = p \tag{B.6}$$

$$-\frac{r^3}{4}\cos\alpha = q \tag{B.7}$$

Solving these for r and α we have

$$r = \sqrt{-\frac{4\pi}{3}} \tag{B.8}$$

$$\alpha = \frac{1}{3}\arccos\left(-\frac{4q}{r^3}\right) \tag{B.9}$$

so that, for the cubic B.1 to have three real roots, the conditions $p < 0$ and

$$|\frac{4q}{r^3}| < 1$$

must hold.

The three roots are given, then, by:

$$u_1 = r\cos\alpha \tag{B.10}$$

$$u_2 = r\cos\left(\alpha + \frac{2\pi}{3}\right) \tag{B.11}$$

$$u_3 = r\cos\left(\alpha - \frac{2\pi}{3}\right) \tag{B.12}$$

Bibliography

[1] E. Asseo, C. F. Kennel, and R. Pellat. Synchro-Compton radiation damping of relativistically strong linearly polarized plasma waves. A&A, 65:401–408, May 1978.

[2] E. Asseo, F. C. Kennel, and R. Pellat. Flux limit on cosmic ray acceleration by strong spherical pulsar waves. A&A, 44:31–40, November 1975.

[3] E. Asseo, R. Pellat, and X. Llobet. Spherical propagation of large amplitude pulsar waves. A&A, 139:417–425, October 1984.

[4] T. Baeva, S. Gordienko, and A. Pukhov. Theory of high-order harmonic generation in relativistic laser interaction with overdense plasma. Phys. Rev. E, 74(4):046404–+, October 2006.

[5] S.-W. Bahk, P. Rousseau, T. A. Planchon, V. Chvykov, G. Kalintchenko, A. Maksimchuk, G. A. Mourou, and V. Yanovsky. Generation and characterization of the highest laser intensities (10ˆ22 W/cm2). *Optics Letters*, 29:2837–2839, December 2004.

[6] W. Becker, editor. *Neutron Stars and Pulsars*, volume 357 of *Astrophysics and Space Science Library*, 2009.

[7] A. R. Bell and J. G. Kirk. Possibility of Prolific Pair Production with High-Power Lasers. *Physical Review Letters*, 101(20):200403–+, November 2008.

[8] V. S. Beskin, I. V. Kuznetsova, and R. R. Rafikov. On the MHD effects on the force-free monopole outflow. MNRAS, 299:341–348, September 1998.

[9] S. Bogovalov and K. Tsinganos. On the magnetic acceleration and collimation of astrophysical outflows. MNRAS, 305:211–224, May 1999.

[10] S. V. Bogovalov. On the physics of cold MHD winds from oblique rotators. A&A, 349:1017–1026, September 1999.

[11] D. L. Burke, R. C. Field, G. Horton-Smith, J. E. Spencer, D. Walz, S. C. Berridge, W. M. Bugg, K. Shmakov, A. W. Weidemann, C. Bula, K. T. McDonald, E. J. Prebys, C. Bamber, S. J. Boege, T. Koffas, T. Kotseroglou, A. C. Melissinos, D. D. Meyerhofer, D. A. Reis, and W. Ragg. Positron Production in Multiphoton Light-by-Light Scattering. *Physical Review Letters*, 79:1626–1629, September 1997.

[12] H. Chen, S. C. Wilks, J. D. Bonlie, E. P. Liang, J. Myatt, D. F. Price, D. D. Meyerhofer, and P. Beiersdorfer. Relativistic Positron Creation Using Ultraintense Short Pulse Lasers. *Physical Review Letters*, 102(10):105001–+, March 2009.

[13] A. Cheng, M. Ruderman, and P. Sutherland. Current flow in pulsar magnetospheres. ApJ, 203:209–212, January 1976.

[14] A. F. Cheng and M. A. Ruderman. Pair-production discharges above pulsar polar caps. ApJ, 214:598–606, June 1977.

[15] P. C. Clemmow. Nonlinear waves in a cold plasma by Lorentz transformation. *Journal of Plasma Physics*, 12:297–317, October 1974.

[16] P. C. Clemmow. Nonlinear, superluminous, periodic waves in a plasma with magnetic field. *Journal of Plasma Physics*, 17:301–316, April 1977.

[17] F. V. Coroniti. Magnetically striped relativistic magnetohydrodynamic winds - The Crab Nebula revisited. ApJ, 349:538–545, February 1990.

[18] A. Dubietis, G. Jonušauskas, and A. Piskarskas. Powerful femtosecond pulse generation by chirped and stretched pulse parametric amplification in BBO crystal. *Optics Communications*, 88:437–440, April 1992.

[19] R. Duclous, J. G. Kirk, and A. R. Bell. Monte Carlo calculations of pair production in high-intensity laser-plasma interactions. *Plasma Physics and Controlled Fusion*, 53(1):015009–+, January 2011.

[20] T. Erber. High-Energy Electromagnetic Conversion Processes in Intense Magnetic Fields. *Reviews of Modern Physics*, 38:626–659, October 1966.

[21] A. M. Fedotov, N. B. Narozhny, G. Mourou, and G. Korn. Limitations on the Attainable Intensity of High Power Lasers. *Physical Review Letters*, 105(8):080402–+, August 2010.

[22] R. Fitzpatrick. *The Physics of Plasmas*. 2008.

[23] Y. A. Gallant, M. Hoshino, A. B. Langdon, J. Arons, and C. E. Max. Relativistic, perpendicular shocks in electron-positron plasmas. ApJ, 391:73–101, May 1992.

[24] S. Glenzer. Layered capsule implosions on the National Ignition Facility. *APS Meeting Abstracts*, pages 6011–+, November 2010.

[25] T. Gold. Rotating Neutron Stars as the Origin of the Pulsating Radio Sources. Nature, 218:731–732, May 1968.

[26] P. Goldreich and W. H. Julian. Pulsar Electrodynamics. ApJ, 157:869–+, August 1969.

[27] A. W. Goodman, . *Algebra from A to Z, World Scientific Publishing*. 2002.

[28] J. P. Gordon, H. J. Zeiger, and C. H. Townes. Molecular Microwave Oscillator and New Hyperfine Structure in the Microwave Spectrum o f NH3. *Physical Review*, 95:282–284, July 1954.

[29] J. E. Gunn and J. P. Ostriker. Acceleration of High-Energy Cosmic Rays by Pulsars. *Physical Review Letters*, 22:728–731, April 1969.

[30] J. E. Gunn and J. P. Ostriker. Magnetic Dipole Radiation from Pulsars. Nature, 221:454–456, February 1969.

[31] J. E. Gunn and J. P. Ostriker. On the Nature of Pulsars. III. Analysis of Observations. ApJ, 160:979–+, June 1970.

[32] J. E. Gunn and J. P. Ostriker. On the Motion and Radiation of Charged Particles in Strong Electromagnetic Waves. I. Motion in Plane and Spherical Waves. ApJ, 165:523–+, May 1971.

[33] T. Heinzl and A. Ilderton. A Lorentz and gauge invariant measure of laser intensity. *Optics Communications*, 282:1879–1883, May 2009.

[34] R. W. Hellwarth. Theory of the Pulsation of Fluorescent Light From Ruby. *Physical Review Letters*, 6:9–12, January 1961.

[35] C. Hernandez-Gomez, S. P. Blake, O. Chekhlov, R. J. Clarke, A. M. Dunne, M. Galimberti, S. Hancock, R. Heathcote, P. Holligan, A. Lyachev, P. Matousek, I. O. Musgrave, D. Neely, P. A. Norreys, I. Ross, Y. Tang, T. B. Winstone, B. E. Wyborn, and J. Collier. The Vulcan 10 PW project. *Journal of Physics Conference Series*, 244(3):032006–+, August 2010.

[36] C. Hernandez-Gomez, J. L. Collier, D. Canny, O. Chekhlov, R. J. Clarke, M. Dunne, M. Galimberti, S. Hancock, R. Heathcote, P. Holligan, A. Lyachev, P. Matousek, I. Musgrave, Neely, D, D. Pepler, I. N. Ross, Y. Tang, T. Winstone, and B. E. Wyborn. The Vulcan 10PW OPCPA project. *Central Laser Facility Annual Report 2006/2007*, pages 211–212, 2007.

[37] A. Hewish, S. J. Bell, J. D. H. Pilkington, P. F. Scott, and R. A. Collins. Observation of a Rapidly Pulsating Radio Source. Nature, 217:709–713, February 1968.

[38] N. Iwamoto. Collective modes in nonrelativistic electron-positron plasmas. Phys. Rev. E, 47:604–611, January 1993.

[39] C. F. Kennel and F. V. Coroniti. Confinement of the Crab pulsar's wind by its supernova remnant. ApJ, 283:694–709, August 1984.

[40] C. F. Kennel and F. V. Coroniti. Magnetohydrodynamic model of Crab nebula radiation. ApJ, 283:710–730, August 1984.

[41] C. F. Kennel and R. Pellat. Relativistic nonlinear plasma waves in a magnetic field. *Journal of Plasma Physics*, 15:335–355, June 1976.

[42] J. G. Kirk. Particle Acceleration in Relativistic Current Sheets. *Physical Review Letters*, 92(18):181101–+, May 2004.

[43] J. G. Kirk. Waves in pulsar winds. *ArXiv e-prints*, August 2010.

[44] J. G. Kirk, A. R. Bell, and I. Arka. Pair production in counter-propagating laser beams. *Plasma Physics and Controlled Fusion*, 51(8):085008–+, August 2009.

[45] J. G. Kirk, Y. Lyubarsky, and J. Petri. The theory of pulsar winds and nebulae. *ArXiv Astrophysics e-prints*, March 2007.

[46] J. G. Kirk and O. Skjæraasen. Dissipation in Poynting-Flux-dominated Flows: The σ-Problem of the Crab Pulsar Wind. ApJ, 591:366–379, July 2003.

[47] L. D. Landau and E. M. Lifshit's. *Quantum mechanics : non-relativistic theory*. 1991.

[48] L. D. Landau and E. M. Lifshitz. *The classical theory of fields*. Elsevier, 1975.

[49] M. I. Large, A. E. Vaughan, and B. Y. Mills. A Pulsar Supernova Association? Nature, 220:340–341, October 1968.

[50] Y. Y. Lau, F. He, D. P. Umstadter, and R. Kowalczyk. Nonlinear Thomson scattering: A tutorial. *Physics of Plasmas*, 10:2155–2162, May 2003.

[51] K. W. D. Ledingham and W. Galster. Laser-driven particle and photon beams and some applications. *New Journal of Physics*, 12(4):045005–+, April 2010.

[52] Y. Lyubarsky. Electron-Ion Coupling Upstream of Relativistic Collisionless Shocks. ApJ, 652:1297–1305, December 2006.

[53] Y. Lyubarsky and J. G. Kirk. Reconnection in a Striped Pulsar Wind. ApJ, 547:437–448, January 2001.

[54] Y. Lyubarsky and M. Liverts. Particle Acceleration in the Driven Relativistic Reconnection. ApJ, 682:1436–1442, August 2008.

[55] Y. E. Lyubarsky. On the structure of the inner Crab Nebula. MNRAS, 329:L34–L36, January 2002.

[56] Y. E. Lyubarsky. The termination shock in a striped pulsar wind. MNRAS, 345:153–160, October 2003.

[57] T. H. Maiman. Stimulated Optical Radiation in Ruby. Nature, 187:493–494, August 1960.

[58] C. E. Max. Steady-state solutions for relativistically strong electromagnetic waves in plasmas. *Physics of Fluids*, 16:1277–1288, 1973.

[59] A. Melatos and D. B. Melrose. Energy transport in a rotation-modulated pulsar wind. MNRAS, 279:1168–1190, April 1996.

[60] F. C. Michel. Rotating Magnetospheres: an Exact 3-D Solution. ApJ, 180:L133+, March 1973.

[61] F. C. Michel. Theory of pulsar magnetospheres. *Reviews of Modern Physics*, 54:1–66, January 1982.

[62] F. C. Michel. Magnetic structure of pulsar winds. ApJ, 431:397–401, August 1994.

[63] C. W. Misner, K. S. Thorne, and J. A. Wheeler. *Gravitation*. 1973.

[64] H. W. Mocker and R. J. Collins. Mode Competition and Self-Locking Effects in a Q-Switched Ruby Laser. *Applied Physics Letters*, 7:270–273, November 1965.

[65] P. F. Moulton. Spectroscopic and laser characteristics of Ti:Al2O3. *Journal of the Optical Society of America B Optical Physics*, 3:125–133, January 1986.

[66] G. Mourou and T. Tajima. More Intense, Shorter Pulses. *Science*, 331:41–, January 2011.

[67] G. A. Mourou, C. P. J. Barty, and M. D. Perry. Ultrahigh-intensity lasers: Physics of the extreme on a tabletop. *Physics Today*, 51:22–28, January 1998.

[68] G. A. Mourou, T. Tajima, and S. V. Bulanov. Optics in the relativistic regime. *Reviews of Modern Physics*, 78:309–371, April 2006.

[69] J. Ostriker. Possible Model for a Rapidly Pulsating Radio Source. Nature, 217:1227–1228, March 1968.

[70] J. P. Ostriker and J. E. Gunn. Do Pulsars Turn Off? Nature, 223:813–814, August 1969.

[71] J. P. Ostriker and J. E. Gunn. Magnetic Decay and the Maximum Period of Pulsars. In *Bulletin of the American Astronomical Society*, volume 1 of *Bulletin of the American Astronomical Society*, pages 357–358, September 1969.

[72] J. P. Ostriker and J. E. Gunn. On the Nature of Pulsars. I. Theory. ApJ, 157:1395–+, September 1969.

[73] J. Pétri and Y. Lyubarsky. Magnetic reconnection at the termination shock in a striped pulsar wind. A&A, 473:683–700, October 2007.

[74] W. H. Press, S. A. Teukolsky, W. T. Vetterling, and B. P. Flannery. *Numerical recipes in FORTRAN. The art of scientific computing*. 1992.

[75] M. J. Rees and J. E. Gunn. The origin of the magnetic field and relativistic particles in the Crab Nebula. MNRAS, 167:1–12, April 1974.

[76] V. I. Ritus. Quantum effects in the interaction of elementary particles with an intense electromagnetic field. *Moscow Izdatel Nauka AN SSR Fizicheskii Institut Trudy*, 111:5–151, 1979.

[77] M. A. Ruderman and P. G. Sutherland. Theory of pulsars - Polar caps, sparks, and coherent microwave radiation. ApJ, 196:51–72, February 1975.

[78] J. Schwinger. On Gauge Invariance and Vacuum Polarization. *Physical Review*, 82:664–679, June 1951.

[79] J. Schwinger, L. L. Deraad, Jr., K. A. Milton, W.-Y. Tsai, and J. Mehra. *Classical Electrodynamics*. 1998.

[80] J. W. Shearer, J. Garrison, J. Wong, and J. E. Swain. Pair Production by Relativistic Electrons from an Intense Laser Focus. Phys. Rev. A, 8:1582–1588, September 1973.

[81] C. S. Shen and D. White. Energy Straggling and Radiation Reaction for Magnetic Bremsstrahlung. *Physical Review Letters*, 28:455–459, February 1972.

[82] L. Sironi and A. Spitkovsky. Particle Acceleration in Relativistic Magnetized Collisionless Pair Shocks: Dependence of Shock Acceleration on Magnetic Obliquity. ApJ, 698:1523–1549, June 2009.

[83] A. Spitkovsky. Time-dependent Force-free Pulsar Magnetospheres: Axisymmetric and Oblique Rotators. ApJ, 648:L51–L54, September 2006.

[84] D. H. Staelin and E. C. Reifenstein, III. Pulsating Radio Sources near the Crab Nebula. *Science*, 162:1481–1483, December 1968.

[85] D. Strickland and G. Mourou. Compression of amplified chirped optical pulses. *Optics Communications*, 56:219–221, December 1985.

[86] Official ELI website. http://www.extreme-light-infrastructure.eu/.

[87] Official HiPER website. http://www.hiper-laser.org/.

[88] Official NIF website. https://lasers.llnl.gov/.

[89] L. Woltjer. The Nature of Pulsating Radio Sources. ApJ, 152:L179+, June 1968.

Some words of thanks

First and foremost I'd like to thank my supervisor **John Kirk**, for his patience, for his commitment to his students and his projects, for being a role model and sharing with me his insights and his deep knowledge of physics. I feel grateful to have been able to learn from him.

I would like to thank the members of the examination committee **Norbert Christlieb**, **Cornelis Dullemond**, and **Carsten Müller** (who agreed to undertake the assessment of the thesis, in spite of his full schedule).

Words are not enough to convey my gratitude towards **Apostolos Mastichiadis**, for help anytime I needed it, words of encouragement, always giving good advice, sharing thai food, long conversations, and for being a friend at the same time as being a teacher.

Many thanks to **Frank Rieger** for lots and lots and lots of good advice in the face of crisis and editing the german abstract and to **Richard Tuffs** for stimulating discussions and for correcting spelling and grammar mistakes. Thanks also to **Jerome Pétri** for useful discussions.

Thanks to **Massimo**, **Kelly**, **Iwona**, **Brian**, **Olaf** and **Eva** for their friendship and support.

Dave, thanks for making me love Australia though I've never been there, for all the chocolate-coated macadamias, the chili dinners, the coffee breaks and for being a fine chap, indeed.

Life in Heidelberg wouldn't have been the same without my officemate **Ellen Andrae**, whose support and loyalty never failed me. Thanks for everything from translating contracts and explaining bureaucratic procedures to support in difficult times. Also to **Rene Andrae**, a wonderful guy and a wonderful friend, thanks for always stepping in to help!

Steevie, thanks for the support and all the laughs. Love you, miss you.

Christina, thanks for being a friend and believing in me!

My family deserve more thanks than I could express here. **My mother**, however, I'd like to especially mention: for continuing to selflessly offer her help under any circumstances, for being a role model and keeping calm in difficult times, for rarely losing her patience, for doing everything to please us, thanks and cheers to mum!

Bei der super-Oma **Elisabeth Hafner**, meiner Schwiegermutter, möchte ich mich auch bedanken. Ohne ihre Ständige Unterstützung wäre unser Leben schwieriger, und weniger genussvoll!

As for my husband, well, he knows ◡̈
Finally, a big thanks to my beautiful baby daughter ♡Athina♡, who made me get rid of my stress and improve my quality of life.